Alma Mater Studiorum – Università di Bologna

School of Science
Department of Physics and Astronomy
Master Degree Program in Astrophysics and Cosmology

A Multi-Method Approach to membership selection in Ultra-Faint Dwarf Galaxies: The role of RR Lyrae Stars

Graduation Thesis

Presented by:
Maria Letizia Valentini

Supervisor:
Chiar.ma Prof.ssa Barbara Lanzoni

Co-Supervisors:
Dott.ssa Gisella Clementini
Dott.ssa Alessia Garofalo
Dott.ssa Tatiana Muraveva
Dott. Lorenzo Monti

Accademic Year 2024/2025

Contents

Abstract

The formation history of the Milky Way (MW) and, in particular, the assembly of its stellar halo, remains one of the key open questions in modern astrophysics. In recent decades, the advent of increasingly deep and precise large-scale surveys has led to the discovery of dozens of ultra-faint dwarf galaxies (UFDs) surrounding the MW, stellar systems that are significantly smaller and fainter than the MW's classical dwarf spheroidal satellites: Draco, Ursa Minor, Sextans, Fornax, Sculptor, Leo I, Leo II and the disrupting Sagittarius.

UFDs are mainly characterised by old and metal-poor stellar populations, with ages and metallicities comparable to those of the oldest and most metal-poor stars in the Galactic halo, raising the question of a possible evolutionary connection between these systems and the formation process of the Milky Way halo.

RR Lyrae stars are among the most powerful tracers of old and metal-poor stellar populations such as those observed in ultra-faint dwarf galaxies (UFDs). These pulsating variable stars have characteristic pulsation properties that make them crucial tools for probing the structure, stellar content, and dynamical properties of such faint systems. In this context, the European Space Agency (ESA) mission *Gaia* has marked a major breakthrough. By providing homogeneous, high-precision astrometric measurements (including positions, parallaxes, and proper motions) along with multi-band timeseries photometry for more than one billion stars, *Gaia* has opened a striking window onto the structure, formation, and evolution of the Milky Way. Its combined astrometric and photometric all-sky capabilities have also significantly advanced the detection and characterisation of variable sources, including RR Lyrae stars, even within the sparse and challenging environments of UFD galaxies.

The thesis investigates a sample comprising six UFD galaxies using data from the *Gaia* Data Release 3 (DR3), with the goal of identifying RR Lyrae stars that are likely members of these systems. Two complementary methodologies are employed: a classical approach based on proper motion analysis, color-magnitude diagrams, and Period-Wesenheit-Metallicity relations; and a statistical approach using machine learning techniques to associate RR Lyrae stars across the sky with their host galaxies based on astrometric and photometric properties. This dual approach aims to enhance the reliability of membership determination, while also highlighting the potential of machine learning to develop robust clustering techniques for stellar association in the context of the big data era.

The thesis is structured as follows. Chapter 1 offers an overview of the scientific context and background on RR Lyrae stars, UFDs, and the *Gaia* satellite mission. Chapter 2 presents a detailed description of data analysis methods, covering proper motion selection, color-magnitude diagrams, Period-Wesenheit-Metallicity relations, and the application of machine learning clustering algorithms. Chapter 3 presents results of the data analysis for several UFD: Boötes I, Boötes III, Carina II, Coma Berenices, Sagittarius II, and Ursa Major I. Finally, Chapter 4 outlines a summary of the conclusions and prospects for future research.

1 Introduction: Scientific Background

This chapter provides a brief introduction to the key elements that form the scientific context of the present work: RR Lyrae stars, ultra-faint dwarf galaxies, and the *Gaia* mission, which constitutes the primary dataset used throughout this thesis.

1.1 Variable Stars

Variable stars are celestial objects whose luminosity, as observed from Earth, changes over time. These stars are classified into two broad categories depending on the origin of their variability: extrinsic and intrinsic variables. Extrinsic variables exhibit apparent brightness variations caused by external factors, such as eclipses in binary systems or rotational modulation due to star spots or surface features. In contrast, intrinsic variables undergo physical changes within the star itself - including pulsations, eruptions, or structural instabilities - which lead to variations in their energy output. Depending on the physical mechanisms responsible for these changes, intrinsic variables are further subdivided into distinct classes, such as pulsating variables, eruptive variables, and cataclysmic variables.

The intrinsic pulsators play a crucial role in astrophysics, as their periods of variability are often directly related to their intrinsic luminosity, providing valuable tools for measuring cosmic distances and understanding stellar evolution. Among these, Cepheid variables and RR Lyrae stars stand out as primary standard candles.

1.1.1 RR Lyrae Variables

RR Lyrae stars are a class of pulsating variable stars named after their prototype, RR Lyrae[1]. Being typically old ($\geqslant$ 10 Gyr), low-mass ($0.6{-}0.8\,M_{\odot}$) and metal-poor stars, RR Lyrae are predominantly found in the stellar halo, the Galactic bulge, and the thick disk of the Milky Way (MW), serving as reliable tracers of the ancient stellar population therein. They are also widely present in the Galaxy's satellite systems - including globular clusters, classical dwarf spheroidal galaxies, and ultra-faint dwarf galaxies - where their presence reflects the old and metal-poor nature of these environments. As such, RR Lyrae are fundamental probes for reconstructing the formation history and assembly of both the MW and its satellite systems.

RR Lyrae cross the Instability Strip (IS), a roughly vertical band in the color-magnitude diagram where stars become instable for radial pulsation, during their core He-burning phase and are pulsating Horizontal Branch (HB) stars, having periods in the range of $0.2 - 1$ days, and light curve amplitudes between 0.2 and 1.6 mag in the B photometric band.
RR Lyrae stars are primarily classified into three main subtypes based on their light curve morphology and pulsation modes:

- RRab: Fundamental-mode pulsators characterised by asymmetric light curves with a rapid rise to maximum brightness followed by a slower decline; they constitute the majority of observed RR Lyrae stars and their periods generally range from 0.4 to 1.0 days.
- RRc: First-overtone pulsators exhibiting nearly sinusoidal and more symmetric light curves; they have shorter periods, typically between 0.2 and 0.4 days, and generally smaller amplitudes compared to RRab stars.
- RRd: "Double-mode" or "Mixed-mode" pulsators, which simultaneously pulsate in both the fundamental and first-overtone modes; their light curves are more complex, resulting from the superposition of two distinct periods; they are relatively rare, covering only a few percent of the total RR Lyrae population, but they are crucial as the ratio of their pulsation periods can provide direct information about stellar parameters such as, most noteworthy, the mass (Petersen 1973; Nemec et al. 2024, and references therein).

[1] See Salaris et al. (2005) for a comprehensive overview.

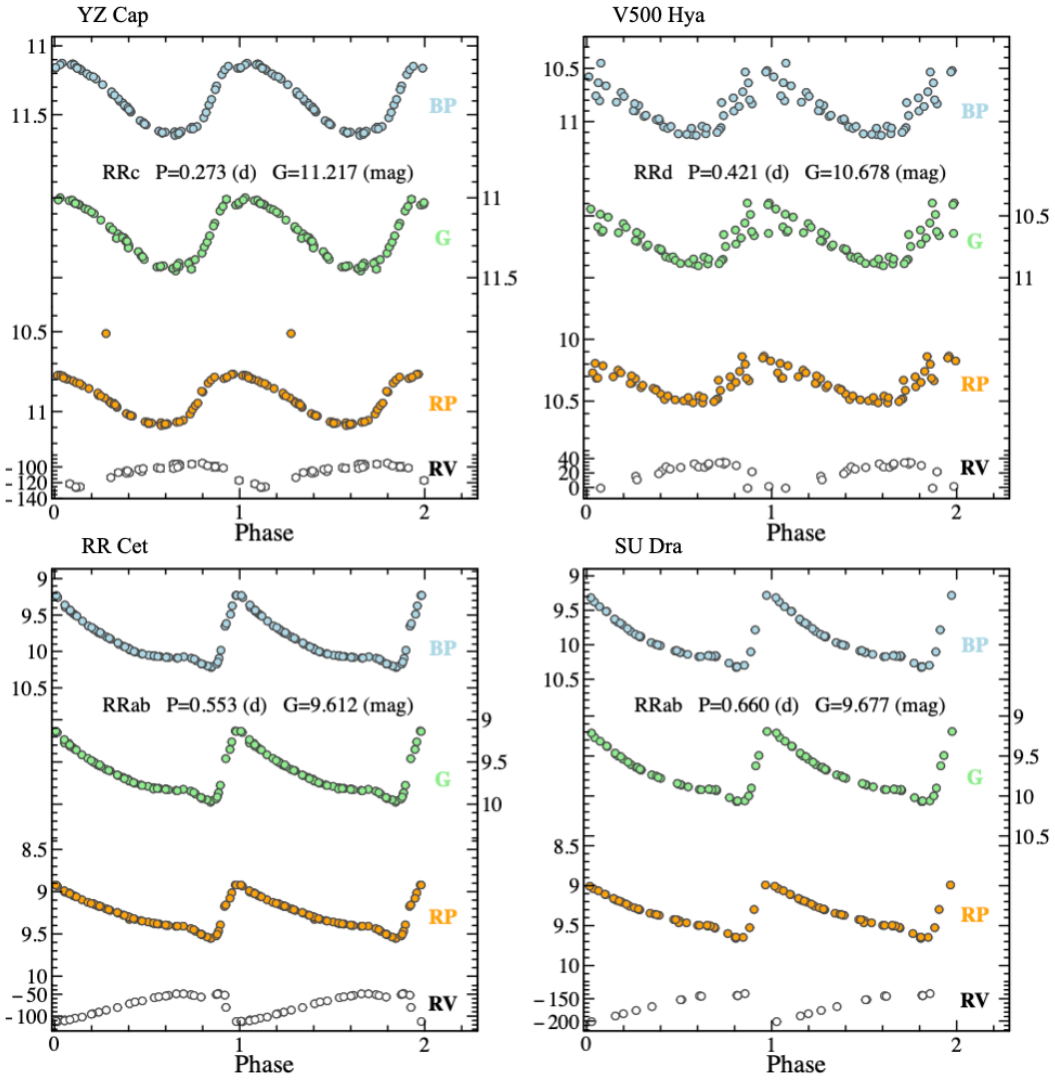

Figure 1: Examples of *Gaia* light and radial velocity (RV) curves of RR Lyrae stars (RRab, RRc and RRd types) published in *Gaia* Data Release 3 (DR3). Each panel shows, from top to bottom, the G_{BP}, G, G_{RP} light curves and the RV curve. Error bars are comparable to or smaller than the symbol size. Figure from Clementini et al. (2023).

RR Lyrae stars are standard candles used to measure the distance to systems composed by old stellar populations, because they conform to a luminosity-metallicity (M-[Fe/H]) relation in the optical bands (e.g. Clementini et al. 2003) and in the *Gaia* bands (e.g. Muraveva et al. 2018; Garofalo et al. 2022) which allows distance estimates based on their metallicity. In the near-infrared (NIR), they obey tight period-luminosity (PL) relations (e.g. Longmore et al. 1986; Braga et al. 2015; Neeley et al. 2017; Muraveva et al. 2018; Neeley et al. 2019), offering even more precise distance estimations thanks to lower extinction and reduced intrinsic scatter of the NIR PL relations.
Moreover, RR Lyrae follow Period-Wesenheit-Metallicity (PWZ) relations that are reddening-free by construction (Madore 1982). These relations become progressively tighter when moving from optical to NIR bands (e.g. Marconi et al. 2015; Muraveva et al. 2018; Braga et al. 2020), further improving the accuracy of distance estimates.
Figure 2 displays the M_G-[Fe/H] relation (left panel) and the $PW_{G,G_{BP},G_{RP}}Z$ relation (right panel) derived from field RR Lyrae stars calibrated using *Gaia* DR3 astrometry and Data Release 2 (DR2) photometry from Garofalo et al. (2022).

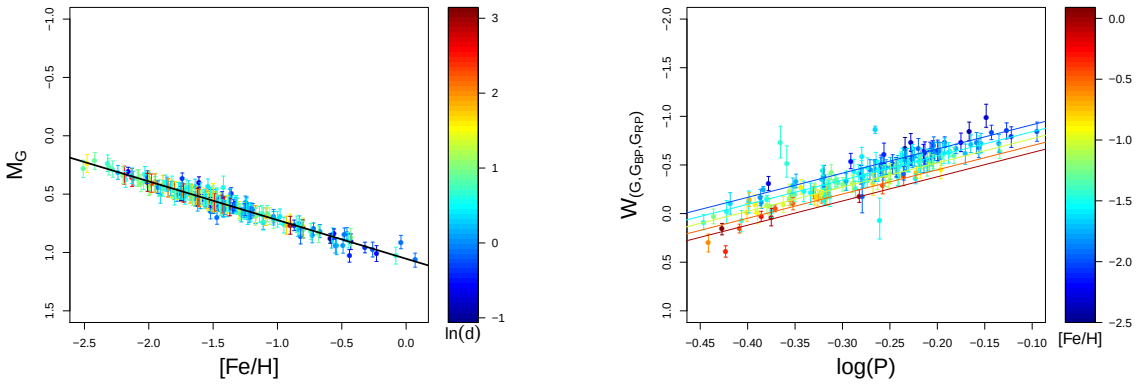

Figure 2: Left: M_G – [Fe/H] relation, and **Right:** $\mathrm{PW}_{G,G_{\mathrm{BP}},G_{\mathrm{RP}}}\mathrm{Z}$ relation from Garofalo et al. (2022), both derived from a sample of field RR Lyrae stars. The calibrations are based on *Gaia* DR2 photometry and *Gaia* DR3 astrometry. In the left panel, the colour scale indicates the logarithm of the barycentric distance in kpc; in the right panel, it shows the metallicity on the Zinn et al. (1984) scale.

1.1.2 Cepheid Variables

Classical Cepheids (CCs, also named δ Cepheids or DCEPs) are a class of pulsating variable stars mainly used as primary standard candles for measuring distances on Galactic and extragalactic scales. Unlike RR Lyrae stars, which are tracers of old, metal-poor populations, CCs are relatively young - ages from tens to a few hundred million years -, massive (3-11 $M_\odot$), and metal-rich stars, associated with Population I systems. They are predominantly found in the thin disk and along the spiral arms of the MW, and in star-forming regions of nearby galaxies.

CCs cross the IS during the core He-burning phase or, in some cases, during shell hydrogen burning, undergoing radial pulsations. Their pulsation periods typically range from about 1 to more than 100 days, with light curve amplitudes typically between 0.1 and 2 magnitudes in the optical bands.
CCs obey a well-defined and tight PL relation, first discovered by Henrietta Leavitt studying the luminosity variation of Cepheids she had identified on plates of the Small Magellanic Cloud (SMC) (Leavitt et al. 1912). The PL relation of CCs is a cornerstone of the cosmic distance ladder, enabling accurate distance measurements out to tens of megaparsecs. It is remarkably linear over a broad period range, particularly in the near-infrared bands, where it is less affected by interstellar extinction and metallicity effects.

Thanks to their high luminosity (up to several thousand $L_\odot$), CCs are detectable at cosmological distances and play a crucial role in the determination of the Hubble constant and the expansion rate of the Universe (Riess et al. 2022, and references therein).
The presence of CCs in a galaxy indicates ongoing or recent star formation and thus a young stellar component, in contrast to RR Lyrae stars, which trace ancient stellar populations. While both classes are crucial distance indicators (Groenewegen 2024, and references therein), they are complementary in probing different epochs of galaxy formation and evolution.

A distinct class of pulsating variables are the Type II Cepheids (T2Cs), which, despite the similarity in name and light curve morphology, are fundamentally different from CCs. T2Cs are low-mass ($\sim 0.5 - 0.6\,M_\odot$), Population II stars, hence old ($\gtrsim$ 10 Gyr) and metal-poor. They are typically found in the Galactic halo, thick disk, globular clusters, and dwarf spheroidal galaxies. They cross the IS during advanced evolutionary phases: post-horizontal branch or during the asymptotic giant branch (AGB) evolution.
T2Cs are subdivided into three subclasses based on their pulsation periods: BL Herculis stars, with periods between 1 and 4 days; W Virginis stars, with periods ranging from 4 to 20 days; and RV Tauri stars, with periods longer than 20 days. The latter are characterised by alternating deep and shallow minima in their light curves (Soszyński et al. 2008, and references therein).
T2Cs are fainter than CCs of the same period and follow their own PL and PW relations (Sicignano et al. 2024; Narloch et al. 2025, and references therein). Given their association with old populations, T2Cs are valuable tracers for studying the structure and evolution of the Galactic halo and nearby dwarf galaxies,

providing independent distance estimates complementary to those derived from RR Lyrae stars.

Anomalous Cepheids (ACEPs) have properties that do not neatly fit into the established categories of CCs, T2Cs, or RR Lyrae stars. They are typically brighter than RR Lyrae stars of comparable period, yet fainter and often with shorter periods than CCs. In details, they are characterised by periods ranging from approximately 0.4 to 2 days, hence typically shorter than those of CCs but longer than those of RR Lyrae stars. They are more luminous than RR Lyrae stars but less massive than CCs, with masses generally between 1.2 and 2.2 $M_{\odot}$ (Bono et al. 1997). ACEPs are commonly found in metal-poor environments, with typical metallicities of [Fe/H] $\lesssim -1.5$ (Caputo et al. 2004; Ripepi et al. 2024, and references therein).

Two main formation scenarios have been proposed for ACEPs: they can originate either as single intermediate-age stars ($2-6$ Gyr) that evolved from relatively low-metallicity populations, or as products of binary evolution, where mass transfer or mergers between low-mass stars produce a more massive star capable of entering the IS. ACEPs are commonly observed in systems dominated by old, metal-poor stellar populations like dwarf spheroidal galaxies, ultra-faint dwarf galaxies, and globular clusters, where recent star formation is unlikely, hence supporting the binary evolution channel.

Like CCs and RR Lyrae stars, ACEPs are subdivided into fundamental-mode (F) and first-overtone (1O) pulsators and follow well-defined Period-Luminosity (PL) and PW relations.These relations have been empirically calibrated in various photometric bands, from optical (e.g., Ripepi et al. 2014; Soszyński et al. 2015), including *Gaia* bands (e.g., Ripepi et al. 2019; Ripepi et al. 2023), to near-infrared bands (Sicignano et al. 2025, and references therein). Further empirical tests based on spectroscopic data are needed to verify the dependence of the AC PL and PW relations on metallicity. Figure 3 shows examples of G-band light curves for fundamental mode and first-overtone ACEPs in the Large Magellanic Cloud (LMC) observed by *Gaia* during 28 days of continuous observation of the South Ecliptic Pole in the initial commissioning phase of the mission.

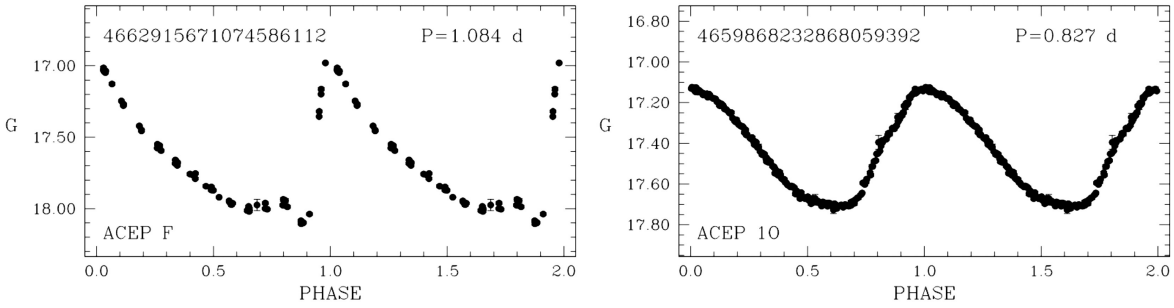

Figure 3: G-band light curves of fundamental mode (F; left panel) and first-overtone (1O; right panel) ACEPs released in *Gaia* Data Release 1 (DR1). Error bars are smaller than or comparable to the symbols. Figure from Clementini et al. (2016).

1.2 Ultra-Faint Dwarf Galaxies

The existence of Ultra-Faint Dwarf (UFD) galaxies became widely recognized soon after the first discoveries in 2005-2007 in the Sloan Digital Sky Survey (SDSS) data (Willman et al. 2005; Belokurov et al. 2007). This breakthrough marked a significant expansion of the knowledge about the lowest-luminosity end of the galaxy luminosity function. Subsequent observational campaigns, employing deeper imaging and spectroscopic follow-up, have progressively unveiled more and more of these elusive systems and allowed for detailed characterisation of their properties.

UFD galaxies represent the least luminous, most dark matter-dominated, and most metal-poor galaxies currently known (Simon 2019, and references therein). With absolute magnitudes fainter than $M_V \sim -7.7$ mag and stellar masses typically below $10^5\,M_{\odot}$, they represent the extremely low-luminosity end of the galaxy population. UFDs are characterised by very low metallicities, typically [Fe/H] $\lesssim -2.5$, and mainly contain old stellar populations, with the majority of their stars formed more than $10-12$ billion years ago.

From a cosmological perspective, UFDs are key objects for understanding the formation of the first galaxies and the role of cosmic reionization in quenching star formation in low-mass halos (e.g. Bullock

et al. 2000; Ricotti et al. 2005; Bovill et al. 2009; Brown et al. 2014). Their stellar populations preserve the chemical signatures of the earliest supernovae, providing a unique window into the processes of early chemical enrichment (Frebel et al. 2015). Dynamically, UFDs are dominated by dark matter, with mass-to-light ratios often exceeding several hundred, making them the most dark matter-dominated systems known in the Universe (Simon et al. 2007; Wolf et al. 2010).
Due to these properties, UFD galaxies are considered fossil relics of the early Universe. Studying them provides fundamental insights into near-field cosmology, the nature of dark matter, and the hierarchical assembly of galaxies in the context of ΛCDM cosmology.

Approximately 50 UFDs are currently known around the MW. Figure 4 presents the sky distribution of the MW UFDs, showing the spatial coverage and discovery locations of these systems.
Similar systems have also been identified in the vicinity of the Andromeda galaxy (M31) and more broadly within the Local Group (Bell et al. 2022, and references therein). The discovery of M31 UFDs has been primarily enabled by deep imaging surveys such as PAndAS (Pan-Andromeda Archaeological Survey; Martin et al. 2009; Arias et al. 2025, and reference therein). These systems provide crucial insights into the small-scale structure formation in different environments within the Local Group, offering a complementary perspective to that obtained from the MW satellites.
Recent work by Jensen et al. (2024) has shown that UFDs often exhibit more extended spatial distributions than previously estimated. This suggests that their stellar components are not as compact as once thought, and that past studies may have underestimated their total luminosities and masses. Accurately characterising the extent and structural parameters of UFDs is essential not only for understanding their formation and evolutionary histories, but also for reconstructing the assembly of the MW, as the properties of these satellites provide key insights into the processes of hierarchical galaxy formation and the growth of stellar halos through accretion of small systems.
Taking into account the findings by Jensen et al. (2024), RR Lyrae stars emerge as a particularly powerful tool to trace the stellar populations in these systems. Their well-established role as standard candles enables precise distance measurements, which are crucial for mapping the three-dimensional structure of such diffuse galaxies, as already made in other systems such as Galactic dwarf spheroidal galaxies (Martínez-Vázquez et al. 2016; Muraveva et al. 2020) and globular clusters (Kundu et al. 2019).
In this context, the *Gaia* mission represents the primary reference catalogue for RR Lyrae stars, providing the most complete, homogeneous, and precise dataset of RR Lyrae variables published to date. Thanks to its all-sky coverage, high-precision astrometry, photometry, and variability characterisation, *Gaia* enables an unprecedented mapping of old stellar populations across the MW and its satellite systems (Clementini et al. 2023; Rimoldini et al. 2023).

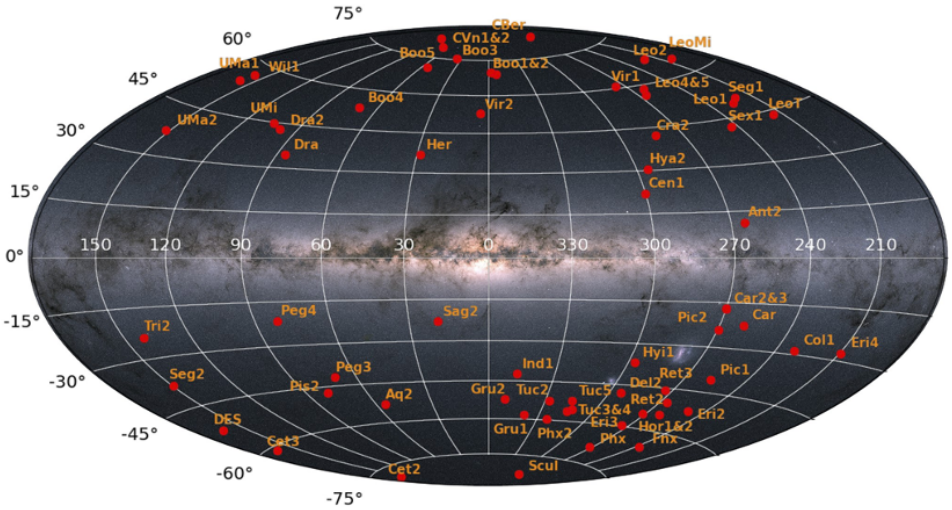

Figure 4: Sky distribution of the known UFD galaxies associated with the Milky Way. The figure shows the location of all currently identified UFDs in Galactic coordinates. Figure from Jensen et al. (2024).

1.3 The *Gaia* Mission

Gaia[2], the ambitious mission of the European Space Agency (ESA) primarily aimed at charting the most precise and comprehensive three-dimensional map of our Galaxy, represents a cornerstone in modern Astronomy. Launched on 19 December 2013, the *Gaia* spacecraft (left panel of Fig. 5) operated from a Lissajous orbit around the Sun-Earth L2 Lagrangian point, approximately 1.5 million km from Earth (right panel of Fig. 5). This strategic position offered a clear view of the cosmos, enabling unique astrometric observations. After more than a decade of groundbreaking operations, *Gaia* officially ended its scientific observations on January 15, 2025, and was subsequently decommissioned on 27 March 2025, transitioning into a post-operations phase focused on final data processing and release.

Gaia's primary objective has been to survey nearly two billion objects, representing approximately one percent of the MW's stellar population, to determine their precise positions, distances (via parallax), and proper motions. Beyond this, *Gaia* also measures stellar brightness, temperatures, and radial velocities, providing a multidimensional census of the Galaxy. This unprecedented dataset is fundamental for understanding the composition, formation, and evolutionary history of our Galaxy.

The spacecraft is equipped with two identical telescopes feeding a common focal plane as schematically represented in Fig. 6. *Gaia*'s payload consisting of a single integrated instrument (left panel of Fig. 7 that comprises three major scientific functions:

- a Sky Mapper and Astrometric Field devoted to star angular position measurements, providing the five astrometric parameters: star position (2 angles); proper motion (2 time derivatives of position) and parallax (distance);
- Blue and Red Photometer Prisms (BP and RP) providing low resolution spectra in the 330-680 nm and 640-1000 nm spectral regions, respectively, for brightness and temperature estimation;
- a Radial Velocity Spectrometer (RVS) for measuring stellar motions along the line of sight and providing spectral data with resolution R=11,500 in the narrow band 847-874 nm of the Ca triplet.

The focal-plane assembly is the largest ever developed for a space application, consisting of 106 CCDs, a total of almost 1,000 million pixels, and a physical dimension of 1.0 m $\times$ 0.4 m (right panel of Fig. 7; Gaia Collaboration et al. 2016).

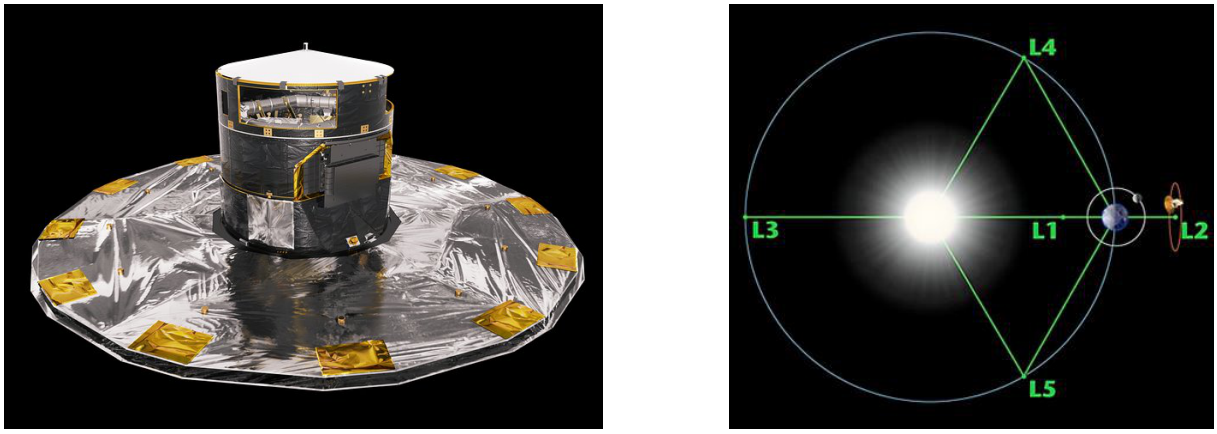

Figure 5: Left: Image of the *Gaia* spacecraft with its sun-shield unfold. **Right:** Schematic view of the *Gaia* spacecraft orbiting the Sun-Earth L2 Lagrangian point in a Lissajous-type orbit.

[2]https://www.esa.int/Science_Exploration/Space_Science/Gaia

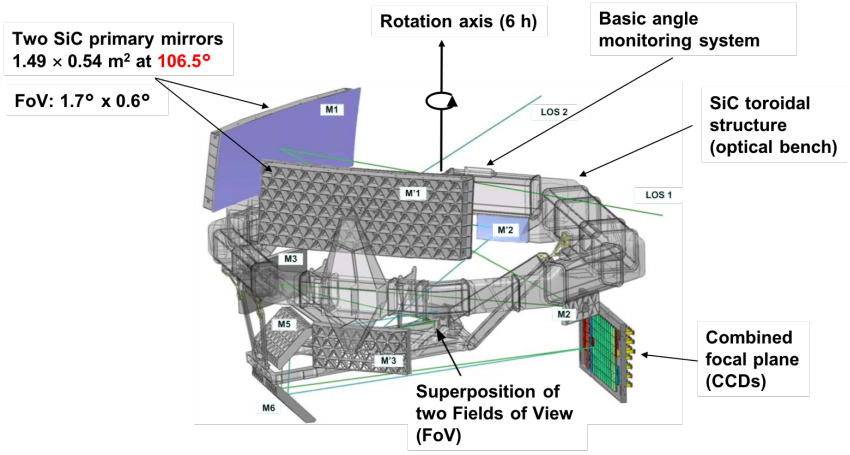

Figure 6: *Gaia*'s payload module with its main components outlined.

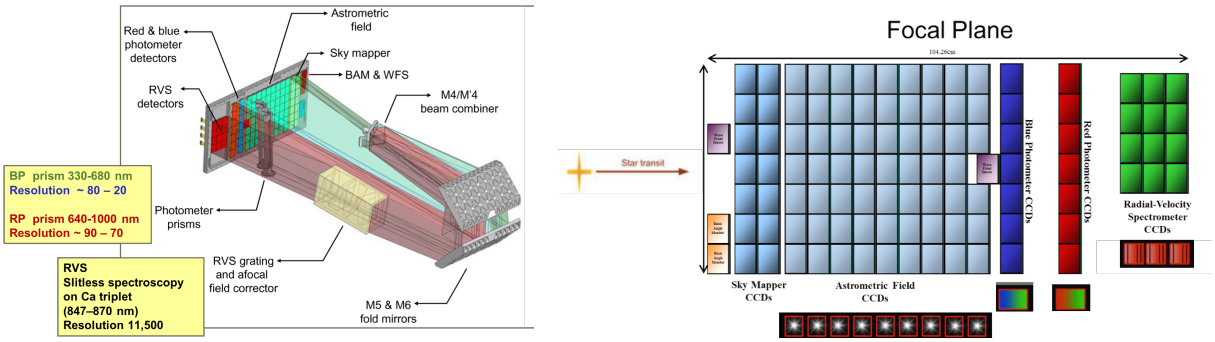

Figure 7: Left: *Gaia*'s single integrated instrument comprising three major scientific functions: astrometry, spectrophotometry with the BP and RP photometer detectors, and slitless spectroscopy on the Calcium triplet with the Radial Velocity Spectrometer (RVS); **Right:** Complete set of 106 CCDs that make up *Gaia*'s focal plane. The 14 CCDs of the Sky Mapper, 62 CCDs of the Astrometric Field, 7 CCDs of the Blue Photometer, 7 CCDs of the Red Photometer, and the 12 CCDs of the RVS are labelled.

In more than 10 years of science operations, *Gaia* has carried an all-sky survey of the entire celestial sphere repeatedly observing, measuring positions, motions, fluxes, etc., and recording data for all sources fainter than $G \sim 3$ mag crossing its field-of-view (FoV), down to a faint limit of $G \sim 21$ mag.
Three main releases of *Gaia* data have taken place so far, each presenting an increased number of sources with progressive improvement in quantity and quality of the released data: (i) Data Release 1 (DR1) on 14 September 2016, based on data collected by *Gaia* in the first 14 months of science operations[3], providing positions (α and δ) and G magnitudes for about 1.143 billion sources, and including also time series G-band photometry and characterisation for 3,194 RR Lyrae stars and Cepheids in the Large Magellanic Cloud (Clementini et al. 2016); (ii) *Gaia* Data Release 2 (DR2) on 25 April 2018, based on data collected in the first 22 months of *Gaia* operations, with position on the sky (α and δ), parallax, and proper motion for more than 1.3 billion sources down to $G \sim 21$ mag, G magnitudes for more than 1.69 billion sources, $G_{\rm BP}$ and $G_{\rm RP}$ magnitudes for more than 1.38 billion sources, median radial velocities for 7.2 million stars, and more than 550,000 variable sources among which 9575 Cepheids and 140,784 RR Lyrae stars[4] (Clementini et al. 2019) ; and (iii) *Gaia* Data Release 3, based on data collected in the first 34 months of science operations, which was split into an Early Data Release 3 (EDR3) published on 3 December 2020, containing position on the sky (α and δ), parallax, and proper motion for around 1.468 billion sources, G magnitudes for around 1.806 billion source, and $G_{\rm BP}$ and $G_{\rm RP}$ magnitudes for around 1.542 billion and 1.555 billion sources, respectively[5], and the full Data Release 3 (DR3) on 13 June 2023 which added

[3]See `https://www.cosmos.esa.int/web/gaia/dr1` for details.
[4]See `https://www.cosmos.esa.int/web/gaia/dr2` for details.
[5]See `https://www.cosmos.esa.int/web/gaia/earlydr3` for details.

object classifications for 1.59 billion sources and astrophysical parameters (T_{eff}, logg, [M/H], absortpion in the G-band, distance, etc.) from BP/RP spectra for 470 million objects, astrophysical parameters (T_{eff}, logg, [M/H], [X/M] for 12 elements, etc.) from RVS spectra for 5.5 million objects, all-sky total galactic extinction maps, mean BP/RP spectra for 219 million sources, mean RVS spectra for 1 million sources, mean radial velocities for 33 million stars, and variability analysis, together with the underlying epoch photometry, for 10.5 million sources, among which more than 15,000 Cepheids (Ripepi et al. 2023) and more than 270,000 RR Lyrae stars[6] (Clementini et al. 2023).

Typical uncertainties of *Gaia* DR3 astrometry and photometry as a fraction of the magnitude of source G are summarised in the upper and lower panels of Table 1, respectively. Figure 8 shows the sky distribution in Galactic coordinates of the sample of 270,905 confirmed RR Lyrae stars published in *Gaia* DR3.

So far, *Gaia* has provided high-precision measurements for billions of stars, revealing previously unseen details of the galaxy structure and dynamics. It discovered hundreds of thousands of new celestial objects, such as extra-solar planets and brown dwarfs, and observed hundreds of thousands of asteroids within our own Solar System. *Gaia* also studied more than one million distant quasars and provided stringent new tests of Albert Einstein's General Theory of Relativity.

The next release of *Gaia* data, Data Release 4 (DR4), is expected not early than end of 2026 and will contain data for all processed sources, which amount to some 2.7 billion sources in total, based on observations collected over 66 months of *Gaia*'s science operations[7].

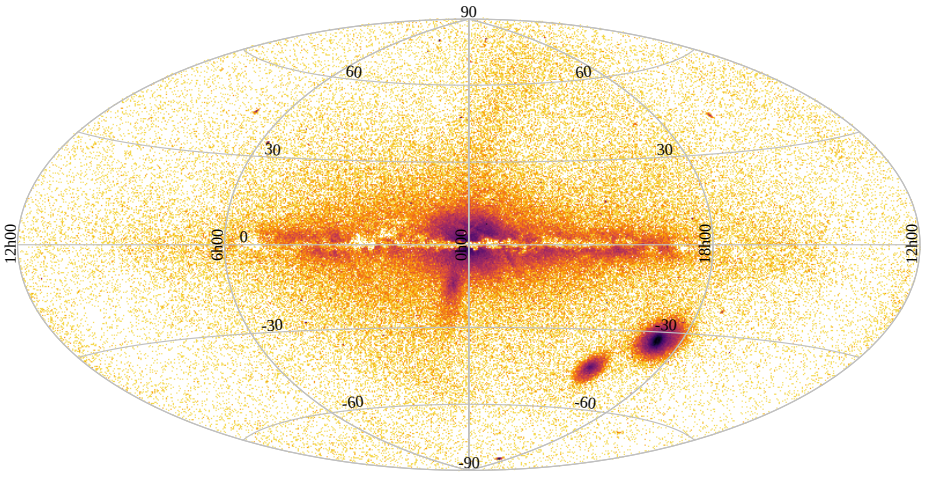

Figure 8: Sky distribution in Galactic coordinates of 270,905 confirmed RR Lyrae stars published in *Gaia* DR3. The sample includes 200,294 previously known RR Lyrae and 70,611 newly discovered by *Gaia*. Figure from Clementini et al. (2023).

[6]See `https://www.cosmos.esa.int/web/gaia/dr3` for details.
[7]See `https://www.cosmos.esa.int/web/gaia/data-release-4` for details.

Table 1: Typical uncertainties for *Gaia* DR3 astrometry (upper panels) and photometry (lower panel). Table adapted from Table 3 of Gaia Collaboration et al. (2021).

G (mag)	**Position (mas)**	**Parallax (mas)**	**Proper motion (mas yr^{-1})**
Five-parameter astrometry*			
<15	0.01–0.02	0.02–0.03	0.02–0.03
17	0.05	0.07	0.07
20	0.4	0.5	0.5
21	1.0	1.3	1.4
Six-parameter astrometry*			
<15	0.02–0.03	0.02–0.04	0.02–0.04
17	0.08	0.10	0.10
20	0.4	0.5	0.6
21	1.0	1.4	1.5
	Mean photometry uncertainty (mmag)		
G	0.3 (G<13)	1 (G=17)	6 (G=20)
G_{BP}	0.9 (G<13)	12 (G=17)	108 (G=20)
G_{RP}	0.6 (G<13)	6 (G=17)	52 (G=20)

Notes. *In *Gaia* astrometry, the five-parameter solution models each source using its position (right ascension and declination), parallax, and proper motions in both coordinates, assuming linear motion. The six-parameter solution introduces an additional parameter-typically a pseudo-colour-to account for chromatic effects or more complex motions, improving the accuracy for sources with problematic colour data or unresolved binaries.

2 Data Analysis: Manual and Automated Approaches

This chapter describes the data analysis procedures developed to identify and characterise the stellar populations of the selected UFD galaxies. The methodology combines step-by-step *manual* selection techniques - based on astrometric, photometric, and pulsation properties - with machine learning approaches.
Each step, from proper motion filtering to the application of PW relations,aims to refine the membership selection and reconstruct clean representations of the stellar populations traced by RR Lyrae members. The process is further complemented by density-based unsupervised Machine Learning (ML) algorithms, which are employed to independently explore the clustering structure of the data, providing an independent membership assessment. The manual procedure, based on classical astrometric and photometric criteria, is employed to train and then test the performance and reliability of the automated clustering.

2.1 Data Description

The data analysed in this thesis were downloaded from the *Gaia* Archive[8], specifically from Data Release 3 (DR3) which provides high-precision astrometric and photometric information for more than one billion sources observed by the *Gaia* mission (as extensively described in Section 1.3).
The UFDs analysed in this work have been selected based on multiple criteria. First, all of them host a population of RR Lyrae stars, which are essential for the variable-star-based membership analysis developed in this study. Second, each system has an available spectroscopic counterpart, which serves as an initial guide to the identification of member stars (see Section 2.1.1). This spectroscopic information is primarily drawn from the homogeneous compilation by Tau et al. (2024), which represents the reference dataset for the selection of the UFDs considered.
The selected galaxies also span a broad range of distances and structural properties. The sample includes systems as nearby as Carina II, located at approximately 38 kpc, and as distant as Ursa Major I, at nearly 100 kpc. This diversity makes the sample particularly suitable for testing the robustness and general applicability of the methodologies developed in this work across different environments.
To provide a comprehensive overview of the sample, Table 2 summarizes the main properties of the six UFDs, including their distance, absolute magnitude, and structural parameters. Figure 9 displays their spatial distribution in the sky.

Table 2: UFDs properties in Vivas et al. (2020). Distance moduli (μ_0) have been directly derived from Vivas et al. (2020) distances.

UFD	**RA** (deg)	**Dec** (deg)	**Distance** (kpc)	$\left[\frac{\mathbf{Fe}}{\mathbf{H}}\right]$ (dex)	$\mathbf{r}_h$ (arcmin)	μ_0 (mag)
Bootes I	210.0200	14.5135	66.0	-2.59	10.5	19.098
Bootes III	209.3	26.8	47.0	-2.1	60	18.360
Carina II	114.1066	-57.9991	37.4	-2.44	8.69	17.864
Coma Berenices	186.7454	23.9069	44.0	-2.25	5.67	18.217
Sagittarius II	298.1663	-22.065	73.1	-2.28	1.7	19.320
Ursa Major I	158.7706	51.9479	97.0	-2.10	8.13	19.934

[8] `https://gea.esac.esa.int/archive/`

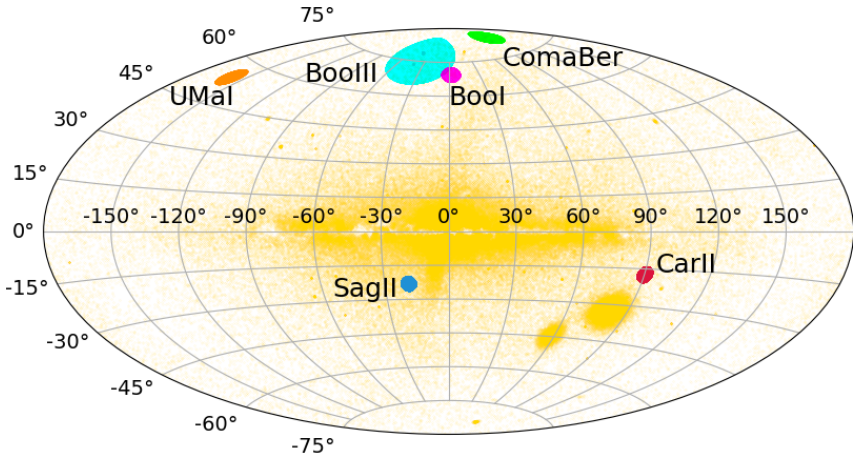

Figure 9: Aitoff Projection of RR Lyrae variables (yellow) in the MW and, highlighted in different colours, stars within 3° or 10° around the centres of the target UFDs.

To define the spatial region associated with each of the selected UFD galaxies, the central coordinates reported in Vivas et al. (2020) were adopted. Circular regions with a radius of 3° were selected around the centres of five of the targets: Boötes I, Carina II, Coma Berenices, Sagittarius II, and Ursa Major I. For Boötes III, a wider radius of 10° was used instead, following Tau et al. (2024) that report the presence of RR Lyrae stars potentially associated with Boötes III at distances greater than 3° from the nominal centre of the galaxy.

Stellar datasets within the selected regions were extracted using ADQL (Astronomical Data Query Language; Ortiz et al. 2008) queries applied to the `gaiadr3.gaia_source` catalogue. This enabled the collection of both astrometric (`ra, dec, pmra, pmdec`) and photometric parameters for all sources located within the specified angular radius of each UFD centre. For what concerns the choice of the photometric parameters, `phot_bp_mean_mag` and `phot_rp_mean_mag` parameters are considered for the $G_{\rm BP}$ and $G_{\rm RP}$ bands, while `int_average_g` parameter is used for the G-band. This choice is motivated by the different reliability of the available *Gaia* photometric measurements at the faint magnitudes of RR Lyrae stars in the target UFDs[9].
Unlike the `int_average_*` parameters, the uncertainties on the photometric quantities `phot_*_mean_mag` are not directly provided in the *Gaia* DR3 catalogue. Therefore, they have been computed through error propagation starting from the flux values,

$$\texttt{phot\_*\_mean\_error} = 1.0857 \, \frac{\texttt{phot\_*\_mean\_flux\_error}}{\texttt{phot\_*\_mean\_flux}} \tag{1}$$

as a result of the definition of the relation between flux and magnitude.

To identify variable stars, *Gaia*'s dedicated variability catalogues were used. In particular, RR Lyrae stars and Cepheids were retrieved from the `gaiadr3.vari_rrlyrae` (Clementini et al. 2023) and `gaiadr3.vari_cepheid` (Ripepi et al. 2023) catalogues, respectively. The `gaiadr3.vari_rrlyrae` table provides detailed pulsation properties for each RR Lyrae star, including the pulsation period and the classification in types (RRab, RRc and RRd) according to the pulsation mode. These quantities are essential for the subsequent steps of the analysis as to tailor the membership selection procedures according to the specific pulsation mode. The queries were applied on an all-sky basis, without spatial constraints around the UFDs.
Additionally, candidate RR Lyrae stars from the `gaiadr3.vari_classifier_result` (Rimoldini et al.

[9]The G-band magnitude, which is a broad-band magnitude spanning a wide wavelength range (300-1000 nm), is derived from the combined measurements of nine CCDs (Charge-Coupled Devices) within the astrometric field (see Fig. 7), and has much higher signal-to-noise (S/N) than the $G_{\rm BP}$ and $G_{\rm RP}$ magnitudes which are derived instead by integrating the low-resolution spectra collected by the BP and RP photometer prisms (see left panel of Fig. 7). Therefore, the `int_average_g` parameter, which is derived from a model-based integration of the G-band light curve accounting for the pulsation it is preferred over `phot_g_mean_mag` since it provides a more representative and robust mean magnitude for pulsating stars. On the other hand, the $G_{\rm BP}$ and $G_{\rm RP}$ light curves of RR Lyrae stars in the target UFDs have much lower S/N (see an example in Fig. 17, Chapter 3), hence the `phot_bp_mean_mag` and `phot_rp_mean_mag` values for $G_{\rm BP}$ and $G_{\rm RP}$ that represent simple averages of the flux measurements are preferred, since more reliable than the `int_average_bp` and `int_average_rp` values.

2023) catalogue were also considered. This catalogue provides variability classifications for a large number of sources, including those not listed in the dedicated variability catalogues, but flagged as potential variable of a certain type by the *Gaia* variability classifier. Specifically, besides the confirmed RR Lyrae stars listed in the `gaiadr3.vari_rrlyrae` table, the `gaiadr3.vari_classifier_result` catalogue contains an additional 30,000 sources classified as candidate RR Lyrae (`best_class_name` = 'RR').

This strategy, based on building datasets that combine astrometric, photometric, and pulsation information, proved to be particularly valuable, as it allowed (i) to perform a more reliable distinction between new RR Lyrae members and non-members of a given system; (ii) to reassess the membership of stars previously classified in the literature; and (iii) to confirm or refine the classification of RR Lyrae variables, by fully exploiting all available parameters.

The data analysis was conducted using Jupyter Notebooks[10], an open-source web-based interactive computing environment developed as an evolution of the IPython Project, enabling creation and sharing of documents containing live codes, equations, visualizations, and narrative text, and facilitating interactive data exploration and reproducibility in scientific workflows.

In general, sources lacking proper motion values, as well as photometric G, $G_{\rm BP}$, and $G_{\rm RP}$ magnitudes, were removed from the dataset since they could not be used in the analysis. In addition to this basic cleaning, two further preliminary steps were performed. First, for each UFD, the *Gaia* DR3 counterparts of the spectroscopically confirmed members were selected (see Section 2.1.1). Second, RR Lyrae stars possibly associated with the Sagittarius stream and/or Galactic globular clusters (GGCs) were excluded, as potential contaminants in the fields of some UFDs (see Section 2.1.2).
After this initial preparation, the manual analysis relied on four key tools: spatial distribution maps, proper motion diagrams, color-magnitude diagrams (CMDs), and the Period-Wesenheit-Metallicity relations. These tools are described in detail in Sections 2.2, 2.3, 2.4, and 2.5, respectively.

2.1.1 Identification of member stars by means of spectroscopic data

To define the sample of candidate member stars for this study, a careful selection process was carried out by incorporating both spectroscopic and photometric data from various sources.
The membership classifications were adopted from the following works: Waller et al. (2023) for Ursa Major I, Coma Berenices, and Boötes I; Carlin et al. (2018) for Boötes III; Zaremba et al. (2025) for Sagittarius II; and Ji et al. (2020) for Carina II. In particular, these studies provide radial velocities and metallicities, which were fundamental for identifying the most probable members of each system. Additionally, Waller et al. (2023) reports, for each star analysed, a membership probability parameter (P_{sat}), ranging from 0 (non-member) to 1 (highly probable member). This parameter reflects the likelihood that a given star is gravitationally bound to the system, based on a combined analysis of spatial position, kinematics, and metallicity.
For the systems: Ursa Major I, Coma Berenices, and Boötes I, only stars with $P_{sat} > 0.7$ were retained in the sample. This threshold was chosen as a balance between maximising the inclusion of members and minimising contamination from field stars. A probability cut at 0.7 ensures a relatively high confidence in membership assignment, while still preserving a sufficiently large sample size for subsequent analysis. This approach is commonly adopted in the literature, where membership is assessed through a combination of kinematic and spatial criteria, as in Fritz et al. (2018, Section 2.2).

2.1.2 Exclusion of contaminants from the Sagittarius Stream and Globular Clusters

The potential contamination from the Sagittarius Stream was carefully considered during the selection of RR Lyrae members of the target UFDs.
In this work, the recent analysis presented by Muraveva et al. (2025a) is adopted as a reference for the identification of likely members of the Sagittarius Stream. That study is based on a comprehensive cross-match between *Gaia* DR3 RR Lyrae stars and known Sagittarius members, employing three independent methods that yield distinct subsets. This combined approach enables a robust identification of Sagittarius-associated RR Lyrae stars, which are then used to flag and exclude potential contaminants overlapping with the UFDs examined in the present analysis.

In the specific case of Boötes III, a careful screening was needed to remove contamination from unrelated variable stars since Boötes III lies in a region that overlaps with the globular clusters NGC5272

[10] `https://jupyter.org/`

(M3) and NGC5466. The Catalogue of Variable Stars in Globular Clusters by Clement et al. (2001)[11] was used to identify RR Lyrae variables associated with these clusters. Any RR Lyrae star located within a 10° in radius and classified as a member of NGC5272 or NGC5466 was removed from the sample of Boötes III candidate members, in order to improve analysis reliability by reducing the contamination from potential non-members (see Section 3.1.2 for details).

2.2 Spatial distribution and mapping of stellar populations

To enhance the visualization and interpretation of the spatial distribution of stellar populations and candidate members within the regions of interest, a series of detailed maps was produced. These visualizations were designed not only to display the overall distribution of sources, but also to isolate specific subsets of stars relevant to the analysis. These maps include the following elements:

- All sources within 3° or 10° from the target centre, to provide a broad overview of stellar density and assess the level of background contamination as a function of angular distance;
- RR Lyrae stars within 3° or 10°, which are essential tracers of old stellar populations and useful for detecting possible tidal features or extended structures;
- Cepheid variables within 3° or 10°, to identify possible contamination from younger populations, although none were expected and actually detected in most target fields.

To outline the structural extent of each UFD galaxy, concentric circles corresponding to multiples of the half-light radius r_h[12] were overlaid. The r_h values were taken from Vivas et al. (2020) (see Table 2). These circles provided useful visual boundaries for identifying both the core and potential extended components of the systems.

In order to evaluate contamination and spatial overlap with known Galactic structures, additional RR Lyrae datasets were included in the mapping:

- RR Lyrae stars associated with the Sagittarius Stream, based on the candidate list from Muraveva et al. (2025a), to support the identification and exclusion of stars likely belonging to this dominant substructure of the Milky Way;
- RR Lyrae stars from the globular clusters NGC5272 (M3) and NGC5466, which spatially overlap with the region surrounding Boötes III and may act as contaminants;
- RR Lyrae candidate members from Tau et al. (2024), used for cross-validation and to assist in population analysis.

In addition, a dedicated set of maps was created to highlight spectroscopically confirmed member stars:

- All members confirmed through spectroscopy;
- Spectroscopic members cross-matched with *Gaia* DR3, which were crucial for proper motion analysis;
- RR Lyrae stars among the spectroscopically confirmed members with *Gaia* DR3 counterparts.

To provide a broader Galactic context, an all-sky map in Galactic coordinates was also produced using an Aitoff projection (see Fig. 9). This map displays all UFD galaxies studied in this work overlaid on the distribution of RR Lyrae stars in the `gaiadr3.vari_rrlyrae` catalogue, offering insights into spatial clustering and potential alignments with large-scale Galactic structures.

Finally, a colormap representation of RR Lyrae and Cepheid variables as a function of their G-band magnitudes was generated for each UFD galaxy (see Chapter 3). This visualization enables the identification of spatial groupings of stars with similar luminosities, which can be indicative of physical associations.

Together, these maps constitute a fundamental component of the analysis, allowing for visual cross-checks of membership assignments, the identification of possible contaminants, and the evaluation of spatial correlations both within and beyond the boundaries of each UFD region.

[11] `https://www.astro.utoronto.ca/~cclement/cat/listngc.html`
[12] The radius within which half of the total luminosity of the galaxy is contained.

2.3 Proper Motions

To refine the selection of potential member stars and variable stars associated with the target system, a detailed analysis of proper motions was conducted. This enabled the identification of kinematically coherent groups and the exclusion of foreground and background contaminants.

A preliminary selection was also performed to remove objects with proper motion uncertainties greater than 0.5 mas yr^{-1}. This threshold reflects the typical uncertainty of the *Gaia* instrument at G $\sim$ 20 mag (see Table 1 adapted from Gaia Collaboration et al. 2021). The stars under investigation are indeed very faint, with G-band magnitudes ranging between 18 and 20 mag.

2.3.1 Proper Motion Filtering and sample refinement

The first step consisted in generating proper motion histograms for stars located within a few multiples of the system's half-light radius. The choice of maximum radius was guided by the observed spatial distribution of spectroscopically confirmed members which have a counterpart in *Gaia* DR3.

A Gaussian fit was applied to the proper motion distributions of these spectroscopic members, allowing for the computation of the mean μ and standard deviation σ for each component (pmra and pmdec). A 3σ selection criterion was then adopted: only stars - both non-variables, RR Lyrae and Cepheids, if present - falling within 3σ of the spectroscopic mean proper motion were retained. This step aimed to isolate a kinematically coherent population for the subsequent photometric analysis and to exploit the pulsation and photometric properties of the variable stars to further distinguish likely members from non-members.

Following the application of the 3σ proper motion cut, updated spatial maps were produced, displaying only those sources which satisfied the kinematic selection. These cleaned maps offered a direct view of the spatial structure of the remaining candidate members, with significantly reduced contamination.

2.4 Color-Magnitude Diagram

To investigate the stellar populations associated with the target system, color-magnitude diagrams using *Gaia* DR3 photometry were generated, focusing specifically on stars that passed the proper motions selection criteria. These diagrams served as essential tools for identifying evolutionary sequences, mainly Horizontal Branch (HB) and Red Giant Branch (RGB) stars to disentangling actual system members from field contaminants.

2.4.1 CMDs of Proper Motion-selected stars

After applying the 3σ proper motion cut, color-magnitude diagrams for all stars within the maximum radius around the centre of each system were generated. These diagrams emphasize the main stellar populations of the systems, highlighting key features such as the HB and the RGB.
Additionally, RR Lyrae and Cepheid variables that passed the proper motion selection were overplotted to clearly visualize their distribution along the appropriate evolutionary phases of the CMD.
All available spectroscopically confirmed members were included in the CMDs to assess their alignment with the expected evolutionary sequences. This comparison served to verify the consistency between the observed CMD morphology and the stellar populations associated with each system.

In the analysis of Boötes III, to examine potential contamination caused by spatial overlap with nearby globular clusters NGC5272 (M3) and NGC5466, RR Lyrae stars associated with the two clusters were also overplotted on the galaxy CMD. Furthermore, RR Lyrae candidates from Tau et al. (2024) were displayed for a broader comparative context.

Overall, this CMD-based approach enhances the proper motion analysis by incorporating photometric and evolutionary information, thereby enhancing the reliability of membership determination and deepening the understanding of the stellar content within each system.

2.5 Period-Wesenheit Relation of RR Lyrae stars

Following the application of the proper motion selection, membership refinement and variable star classification were further improved through the use of the Period-Wesenheit-Metallicity (PWZ) relation for RR Lyrae stars and the Period-Wesenheit (PW) relation for Anomalous Cepheids, based on updated calibrations derived from *Gaia* parallaxes in Garofalo et al. (2022) and Ripepi et al. (2023). This approach provides a robust method for comparing the expected absolute magnitudes of pulsating variables - corrected for metallicity - with their observed magnitudes and distances, thereby facilitating the confirmation or rejection of membership.

2.5.1 Methodology and corrections

To distinguish likely member RR Lyrae stars from non-members, Period-Wesenheit-Metallicity diagrams were employed. The Wesenheit magnitude is, by construction, a reddening-free quantity, designed to be unaffected by extinction under the assumption of a given extinction law. It is defined as a linear combination of magnitudes and colours that effectively removes the effects of interstellar reddening. In the *Gaia* photometric system, it can be expressed as:

$$w(G, G_{\rm BP}, G_{\rm RP}) = G - \lambda \cdot (G_{\rm BP} - G_{\rm RP}) \tag{2}$$

where λ is the ratio of total-to-selective extinction in the *Gaia* bands. The value of λ depends on the adopted extinction law; for the standard MW extinction curve (e.g., with $R_V = 3.1$), typical values range between 1.8 and 2.0, depending on the specific calibration (Ripepi et al. 2019, and reference therein). According to the calibration presented in Garofalo et al. (2022), a value of $\lambda = 1.922$ was adopted in this work.
This reddening-free Wesenheit magnitude, when combined with the pulsation period, allows for a cleaner separation of genuine members from contaminants, since RR Lyrae follow tight PWZ relations that are less affected by line-of-sight extinction variations.
In the analysis, the PWZ relation from Garofalo et al. (2022) was adopted:

$$W = (-2.49^{+0.21}_{-0.20}) \log(P) + (0.14^{+0.03}_{-0.03}), [\mathrm{Fe/H}] + (-0.88^{+0.08}_{-0.09}) \tag{3}$$

which is based on the *Gaia* DR2 photometry and the *Gaia* DR3 parallaxes of about 300 MW field RRab stars (see Garofalo et al. 2022, for details) and provides the absolute Wesenheit magnitude in the *Gaia* G, $G_{\rm BP}$ and $G_{\rm RP}$ bands for fundamental mode RR Lyrae stars, with an intrinsic dispersion of $\sigma = 0.09 \pm 0.01$ mag.
It is important to note that, in order to apply this relation to RRc-type stars as well, their pulsation period was *fundamentalised* - i.e., converted to the equivalent fundamental-mode period - to be used consistently with RRab stars in the same relation. The standard transformation adopted is:

$$\log(P_{\rm fund}) = \log(P_{\rm RRc}) + 0.127 \tag{4}$$

This also applies to RRd-type stars, as the first overtone mode is generally dominant in these variables. In order to apply this relation to the different systems analysed in this study, it was shifted according to the appropriate distance modulus of each UDF galaxy that is listed in Tab. 2 (Vivas et al. 2020). This correction ensures that the relation, originally calibrated in absolute Wesenheit magnitude W, can be properly used in the apparent Wesenheit w plane for each system. The [Fe/H] metallicity values reported in Tab. 2 for each system were assumed.

2.5.2 Application and selection

Period-Wesenheit-Metallicity diagrams were constructed including:

- RRab, RRc, and RRd-type stars, using corrected and fundamentalised periods where appropriate;
- RR Lyrae stars from Tau et al. (2024);
- Spectroscopically confirmed RR Lyrae members;
- RR Lyrae stars of the Sagittarius Stream present in 3° or 10° around the centre of the UFD.

For each system, a 3σ selection was applied around the PWZ relation. Only stars within this range were retained as likely members. This cut served to exclude outliers potentially affected by blending, poor photometric quality, or misclassification, thereby improving the reliability of the RR Lyrae variables.

2.5.3 Color-Magnitude Diagrams update

After applying the PWZ-based selection, the color-magnitude diagrams were reconstructed using only those RR Lyrae stars consistent with the relation, providing a more representative depiction of the variable star population associated with each UFD galaxy.

2.6 Reverse filtering via the PWZ Relations

As a complementary step to the proper motion-based selection, a reverse filtering approach was implemented by first applying the PWZ relation to pre-select reliable variable stars before applying the kinematic (proper motion) cuts. This method allowed for the recovery of potential members that might have otherwise been excluded due to slight deviations in their proper motions, despite being consistent with the system in terms of photometric and pulsation properties.
The procedure followed the methodology previously outlined in Chap. 2.5:

- The PWZ relation for RR Lyrae stars from Garofalo et al. (2022) was applied, using the distance modulus of each UFD and the [Fe/H] values reported in Vivas et al. (2020);
- For RRc and RRd stars, periods were fundamentalised to match the relation defined for RRab stars;
- Only RR Lyrae stars lying within a 3σ band around the PWZ relation were retained.

2.6.1 Identification of misclassified Anomalous Cepheids

In some cases, variables catalogued as RR Lyrae may actually be misclassified Anomalous Cepheids (ACEPs), particularly in metal-poor environments where classification based solely on light curve morphology can be ambiguous. To investigate potential misclassifications, the Period-Wesenheit relations for ACEPs was applied to RR Lyrae stars.

For ACEPs, Ripepi et al. (2023) provides separate calibrations - based on Gaia DR3 data -, for fundamental-mode (F) and first-overtone (1O) pulsators. The general form of the Period-Wesenheit Relation for ACEPs is:

$$W = \alpha + \beta \log(P) \tag{5}$$

with the following coefficients:

- For ACEP-F: $\alpha = -1.717 \pm 0.025$, $\beta = -3.080$, $\sigma = 0.010$
- For ACEP-1O: $\alpha = -2.220 \pm 0.061$, $\beta = -3.500$, $\sigma = 0.013$

Unlike RRc (or RRd) stars, no period conversion is required for ACEPs pulsating in the first overtone, as the relations in Ripepi et al. (2023) explicitly distinguish between fundamental and first-overtone modes.

For the RR Lyrae candidates under consideration:

- Both the fundamental and first-overtone ACEP relations were tested;
- Stars that more closely matched these relations than the RR Lyrae PWZ relation were flagged as potential misclassified ACEPs;
- These stars were subsequently plotted separately in the PW diagram and in the updated color-magnitude diagram to better assess their evolutionary status.

The same procedure was applied to Cepheid stars located within the spatial extent of each UFD.

2.6.2 Proper Motion re-evaluation

Following the PWZ-based selection, the remaining RR Lyrae candidates were cross-checked against the mean proper motions of each system. This step aimed to evaluate whether any stars previously excluded by the initial kinematic filtering could be recovered based on their strong consistency with the PWZ relation.
In several cases, stars initially rejected based on proper motion criteria were found to lie just outside the 3σ boundary from the system's average values. This suggests that such stars may still be physically associated with the host galaxy, particularly in cases where proper motion uncertainties are large or the spectroscopic sample is limited.

2.6.3 Reconstruction of CMDs and Spatial Maps

Following this reverse filtering approach, both of the following graphs were reconstructed:

- Color-magnitude diagrams, based exclusively on RR Lyrae stars and candidate ACEPs selected through the PWZ/PW criteria and subsequently validated through proper motion analysis;
- Spatial maps, illustrating the cleaned, high-confidence sample of variable stars.

This method provided an alternative pathway for membership selection, starting from stellar pulsation properties and serving as a valuable cross-check to purely astrometric criteria.

2.7 Machine Learning Clustering Algorithms

Clustering stands as a fundamental unsupervised Machine Learning task, designed to group a collection of objects in such a way that those within the same group, or cluster, exhibit greater similarity to each other than to objects found in other groups (Greene et al. 2008). Distinct from supervised learning, clustering does not rely on predefined labels, it rather aims to uncover inherent structures or patterns within data by identifying similarities (Fuchs et al. 2022).

2.7.1 Definition and purpose

The core purpose of clustering lies in partitioning a dataset into meaningful subgroups, thereby allowing for a simplified representation of the data that highlights its intrinsic organization. The effectiveness of a clustering algorithm is frequently assessed by its capacity to achieve high intra-cluster similarity, meaning objects within a cluster are alike, and low inter-cluster similarity, where objects in different clusters are dissimilar. The crucial concept of *similarity* is typically defined by a distance metric, such as the Euclidean distance, or by a specific similarity function.

2.7.2 Families of Algorithms

Clustering algorithms can be broadly categorized into several families, each adopting different approaches to defining and forming clusters.

- Partitioning Methods divide data objects into a pre-specified number of non-overlapping partitions or clusters, often through iterative relocation of data points to optimize an objective function.
- Hierarchical Methods build a hierarchy of clusters; agglomerative approaches begin with individual data points as single clusters, progressively merging the closest ones until a single cluster remains or a termination condition is met; divisive approaches start with all data points in one cluster and recursively split them, culminating in a tree-like structure known as a dendrogram.
- Grid-Based Methods quantize the data space into a finite number of cells, forming a grid structure, upon which clustering is then performed, often leading to faster processing times for large datasets.
- Density-Based Methods, unlike partitioning or hierarchical techniques that rely on distance or distributional assumptions, identify clusters as regions of high data point density, separated by regions of lower density. These methods prove particularly effective at discovering clusters of arbitrary shapes and handling noise, and this chapter will explore this family of algorithms in greater detail.

Having established the core principles of clustering, the discussion now focuses on prominent algorithms representative of the density-based paradigm.

2.7.3 Density-Based Clustering

The key idea is that for each point in a cluster, the neighborhood within a given radius has to contain at least a minimum number of points, i.e. the density in the neighborhood exceeds some threshold. The shape of this neighborhood is determined by the choice of a distance function for between points p and q, denoted by $dist(p, q)$ (Ester et al. 1996). The eps-neighborhood of a point p, denoted by $N_{eps}(p)$,is defined as $N_{eps}(p) = \{q \in D | dist(p, q) \leq eps\}$. So, a region is considered dense if it contains a sufficient number of points within this radius.
Several implementations exist within the broader family of density-based clustering algorithms. Among these, DBSCAN, HDBSCAN, and OPTICS stand out as the most widely adopted and influential.

DBSCAN (Density-Based Spatial Clustering of Applications with Noise) operates by first identifying core points, i.e. points that have at least a minimum number of neighbors within the `eps` radius (Ester et al. 1996). Clusters are then formed by connecting these core points with their reachable neighbors, including border points, which are neighbors of core points but do not themselves satisfy the core point condition. Points located in low-density regions, lacking sufficient neighbors, are classified as noise.
One of the main advantages of DBSCAN is that it does not require specifying the number of clusters beforehand. It is also robust to outliers and capable of detecting clusters of arbitrary shapes and sizes. However, its performance strongly depends on the choice of the `eps` radius and the `min_samples` parameter. Additionally, DBSCAN may struggle to accurately identify clusters in datasets containing regions with varying densities.

HDBSCAN is an extension of DBSCAN designed to address its limitations with clusters of varying densities (Campello et al. 2013). It constructs a hierarchy of clusters and extracts the most stable flat clusters from this hierarchical structure. The algorithm begins by building a minimum spanning tree of the data points, which it then condenses based on cluster density. From the condensed tree, HDBSCAN selects the most stable clusters, those best representing the intrinsic data structure.
Among its strengths, HDBSCAN does not require the number of clusters to be specified in advance, is robust to clusters with varying densities, and effectively identifies noise points. It generally performs more reliably than DBSCAN on complex datasets. However, HDBSCAN can be computationally more intensive and still requires tuning parameters such as `min_cluster_size` and `min_samples` to achieve optimal results.

OPTICS (Ordering Points To Identify the Clustering Structure) is another algorithm developed to overcome DBSCAN limitations with datasets featuring clusters of varying densities (Ankerst et al. 1999). Instead of assigning points to explicit clusters, OPTICS produces an ordered list of data points alongside a reachability distance for each point.
OPTICS offers several advantages: it can detect clusters of varying densities, does not require the number of clusters to be pre-specified, and provides a visual tool (the reachability plot) to better understand the data clustering structure. On the downside, similar to DBSCAN, the choice of parameters such as `min_samples` and `min_cluster_size` remains crucial, and interpreting the reachability plot can require some expertise.

2.7.4 Application of Clustering Methods

In this study, DBSCAN and HDBSCAN algorithms were applied with the objective of determining whether the patterns and groupings previously identified via manual analysis of individual parameters could be effectively replicated using automated techniques. The main goal was to develop a reliable and robust method for the automatic detection and classification of RR Lyrae stars specifically associated with ultra-faint dwarf galaxies, a challenging astrophysical problem due to the sparse and noisy nature of the data. The manual procedure - build upon the traditional astrometric and photometric criteria - serves both as a training reference and as a validation benchmark to evaluate the performance and reliability of the automated clustering methods.

To accomplish this, a comprehensive analysis pipeline was developed and implemented in Python, making use of various clustering algorithms available through the widely used Scikit-learn library[13].

[13] `https://scikit-learn.org/stable/`

Particular emphasis was placed on evaluating the performance of density-based clustering techniques - specifically DBSCAN and HDBSCAN - which are well-suited for identifying clusters of arbitrary shapes and for effectively managing outliers. These algorithms were applied to the dataset corresponding to the Boötes I dwarf galaxy, enabling a detailed assessment of their capability to uncover meaningful stellar groupings in a complex astronomical context.

The analysis was performed on a sample of RR Lyrae stars with magnitudes $G > 18$ mag, selected from the *Gaia* `gaiadr3.vari_rrlyrae` catalogue. Given the focus on intrinsically faint objects such as UFDs, a more manageable dataset was preferred in order to reduce the computational time required by the algorithms. As an initial investigation, the astrometric features RA, Dec, pmra and pmdec were selected for use. As a possible future improvement, the inclusion of the photometric parameters G, G_{BP}, and G_{RP} could enhance the discriminatory power of machine learning techniques, particularly in distinguishing reliable members from field contaminants.

3 Results

This chapter presents the results of the data analysis performed on the six ultra-faint dwarf galaxies considered in this thesis, namely: Boötes I, Boötes III, Carina II, Coma Berenices, Sagittarius II, and Ursa Major I. For each system, the identification and characterisation of RR Lyrae stars are discussed in detail, along with a comparison with the known spectroscopic members and the evaluation of their spatial and photometric properties. The aim is to assess the likelihood of membership for each variable star and to investigate the presence of any structural or dynamical features within these faint systems. Mean proper motions for the six UFDs, computed from specroscopically confirmed member stars, are provided in Table 3, whereas Tab. 2 lists their general properties according to Vivas et al. (2020), and Fig. 9 shows their location within the Milky Way.

Table 3: Mean proper motions of the six UFDs analised in this work, computed from stars with membership confirmed through spectroscopy.

UFD	**pmra** (mas/yr)	**pmdec** (mas/yr)
Boötes I	-0.329 ± 0.687	-1.066 ± 0.833
Boötes III	-1.121 ± 0.764	-1.111 ± 0.666
Carina II	1.884 ± 0.062	0.155 ± 0.064
Coma Berenices	0.732 ± 0.566	-1.624 ± 0.334
Sagittarius II	-0.798 ± 0.067	-0.923 ± 0.012
Ursa Major I	-0.586 ± 0.733	-0.525 ± 0.980

3.1 Boötes I

Boötes I is a satellite galaxy of the Milky Way, discovered in 2006 through a systematic search for stellar overdensities in the North Galactic Cap using data from the Sloan Digital Sky Survey Data Release 5 (SDSS DR5). It is located in the constellation of Boötes, at a distance of approximately 60 kpc from Earth (Belokurov et al. 2006). Morphologically, Boötes I is described as one of the faintest galaxies known, with an absolute magnitude of approximately $M_V \approx -5.8$ mag and a half-light radius of about 220 pc, typical for Galactic dwarf spheroidal galaxies. Its isodensity contours are elongated and have an irregular shape, suggesting that it may be a disrupted dwarf spheroidal galaxy. Its color-magnitude diagram shows a well-defined turn-off, red giant branch, and extended horizontal branch, indicating an old, metal-poor stellar population.

The first discovery of RR Lyrae stars in Boötes I was reported almost simoultaneusly by Dall'Ora et al. (2006) and Siegel (2006), who detected in the galaxy a total of 16 variables: 15 RR Lyrae stars and 1 long period variable candidate.

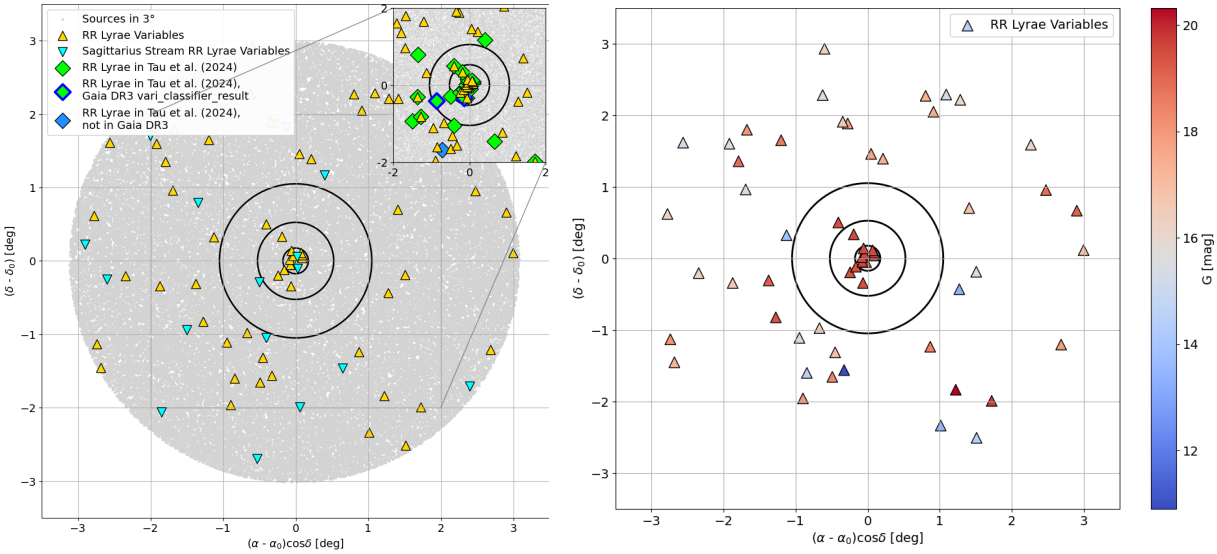

Figure 10: Left: Spatial distribution of sources (grey dots) and RR Lyrae variables (yellow triangles) within 3° around the centre of Boötes I. Cyan triangles: Sagittarius Stream RR Lyrae stars (Muraveva et al. 2025a). Green diamonds: RR Lyrae stars identified by Tau et al. (2024); those with a blue edge are stars also listed as RR Lyrae candidates in the *Gaia* `gaiadr3.vari_classifier_result` catalogue; a blue diamond refers to the star identified by Tau et al. (2024) with no correspondence in the *Gaia* DR3 catalogue. Black circles: 1, 3, 6 r_h around the centre. **Right:** G-band color-map of RR Lyrae stars within 3° around the centre of Boötes I.

3.1.1 Spatial distribution and mapping of stellar population

Within 3° around the centre of Boötes I, there are 74 RR Lyrae variables, together with two candidate RR Lyrae stars which are listed in the *Gaia* `gaiadr3.vari_classifier_result` catalogue (*Gaia* DR3 1230713292302089728 and *Gaia* DR3 1230819704412148224). There are no Cepheid variables in this region. Seventeen RR Lyrae stars that belong to the Sagittarius Stream were removed, so the initial number of variables was reduced to 57 (left panel of Fig. 10).

In Tau et al. (2024), 27 RR Lyrae stars are assigned to Boötes I. One of them is not included in the *Gaia* DR3 dataset, while two are those in the *Gaia* `gaiadr3.vari_classifier_result` catalogue. Several RR Lyrae classified as members in Tau et al. (2024) are also in the Sagittarius Stream, thus, they were discarded from the sample.

Waller et al. (2023) identified a total of 261 stars as members of Boötes I through spectroscopic analysis. Among them, 84 sources with $P_{sat} > 0.7$ have a counterpart in the *Gaia* DR3 catalogue, including six RR Lyrae variables, as shown in Fig. 11. One of these RR Lyrae stars (*Gaia* DR3 1230836437604328704) is a Sagittarius stream candidate in Muraveva et al. (2025a): this case will be brifly discussed in Chapter 3.1.4.

The right panel of Fig. 10 clearly illustrates how a simple visual inspection of the colormap already provides a hint of which objects may belong to the same system. This is based on the concept that RR Lyrae stars share similar intrinsic luminosities, being in the evolutionary phase of the horizontal branch; consequently, those belonging to the same system should also exhibit similar apparent magnitudes. Indeed, objects with comparable G-band magnitude appear spatially clustered toward the centre of the UFD galaxy, reinforcing their likely association.

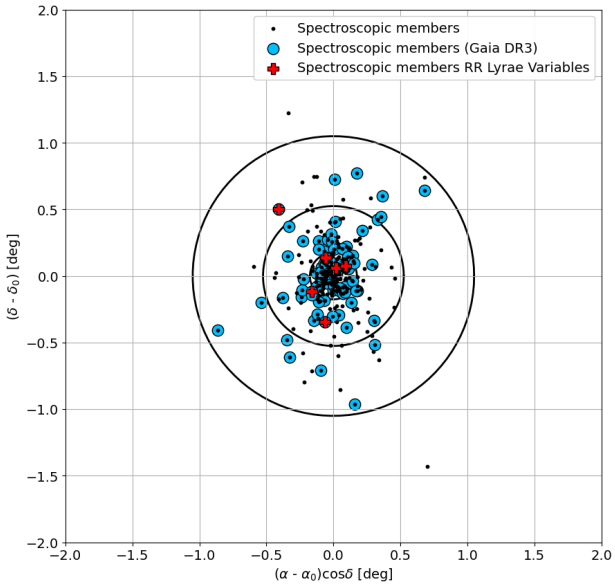

Figure 11: Spatial distribution of member stars identified through spectroscopy by Waller et al. (2023). Red crosses: RR Lyrae spectroscopic members.

3.1.2 Proper Motion and Period-Wesenheit-Metallicity Relation selections

The preliminary cut on objects with proper motion errors greater than 0.5 mas yr^{-1} excluded one faint RR Lyrae (Fig. 12).

During the analysis of proper motions, two stars among the spectroscopically confirmed members had proper motions greater than -10 mas yr^{-1}. For this reason, possible anomalies were inspected. It is likely that a crossmatch mistake had occurred during the selection done by Waller et al. (2023). By using the SIMBAD database[14], it was verified that *Gaia* DR3 1230835475531625216 had been erroneously classified as *Gaia* DR3 1230835578610843648. Waller et al. (2023) catalogue was therefore updated to correct this crossmatch mistake. The other source, *Gaia* DR3 1230833486962192640, is not listed in the *Gaia* DR3 catalogue, hence it was removed.

After these corrections, the proper motion selection was performed. The average values of the proper motions - computed using only the spectroscopic members - are listed in Tab. 3 and the proper motion distributions are shown in Fig. 13. Along with a decrease in number of sources within $6r_h$, the 3σ selection results in 35 RR Lyrae candidates being identified as Boötes I members, together with the two listed in the *Gaia* `gaiadr3.vari_classifier_result` catalogue (*Gaia* DR3 2308197044121482224 and *Gaia* DR3 2307132923020897 28).

The color-magnitude diagram in Fig. 14, shows that the retained RR Lyrae stars fall within a color range in $G_{BP} - G_{RP}$ of approximately 0.5 mag and that some of them appear to be nicely located along the horizontal branch traced by the spectroscopic members. However, a significant spread in G-band magnitude is observed, indicating the need for additional selections based on the PWZ relation.

The distribution of sources within $6r_h$ in the CMD (grey points) also differs significantly from the profile traced by the spectroscopic members. This suggests that the $6r_h$ radius is too large to statistically represent the actual physical extent of Boötes I, and that MW field stars contaminate this region of the sky.

[14] `https://simbad.cds.unistra.fr/simbad/`

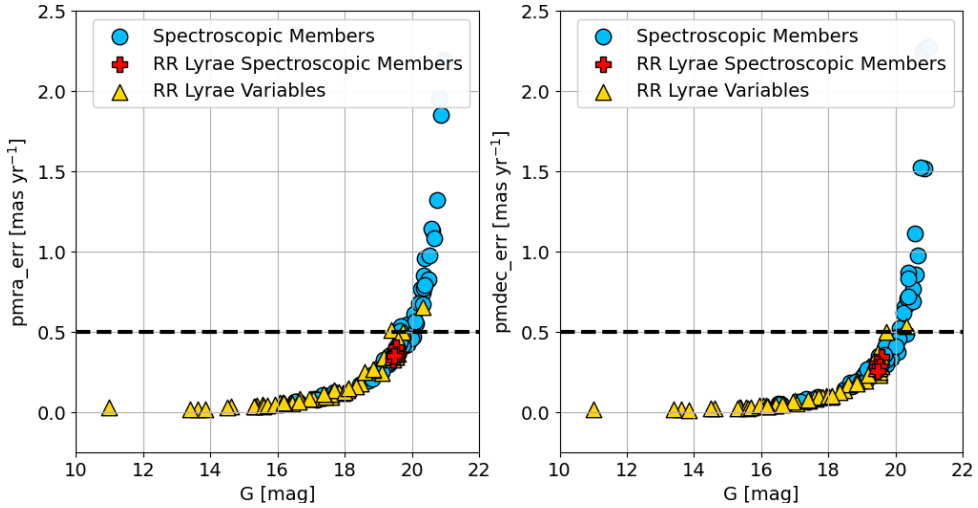

Figure 12: Proper motion errors of RR Lyrae stars (yellow triangles) and spectroscopic members (light-blue dots) within 3° around the centre of Boötes I as a function of G-band magnitude. All RR Lyrae spectroscopic members (red crosses) are located below the 0.5 mas yr^{-1} (dashed) line.

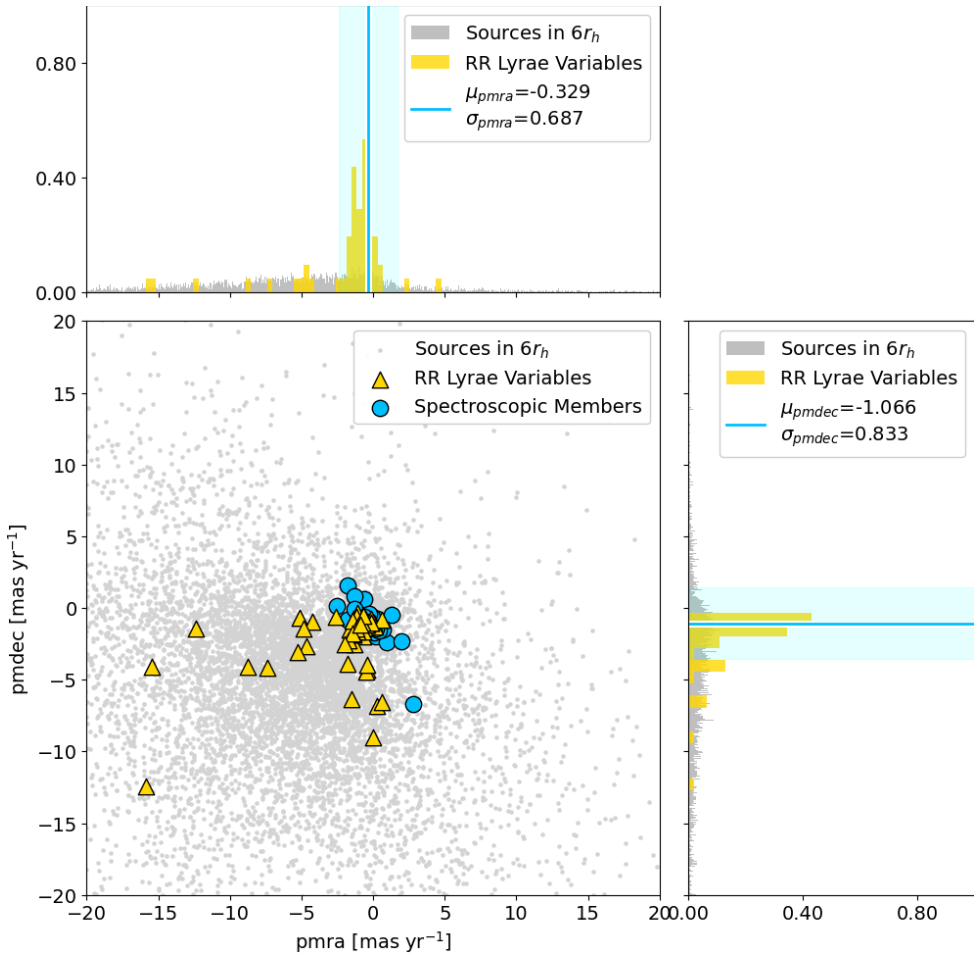

Figure 13: Proper motion distribution of sources within $6r_h$ (grey dots) and RR Lyrae stars within 3° (yellow triangles) around the centre of Boötes I. The cyan shaded bands correspond to $\pm 3\sigma$ of the mean proper motions (cyan lines) computed using the spectroscopic members (light-blue dots).

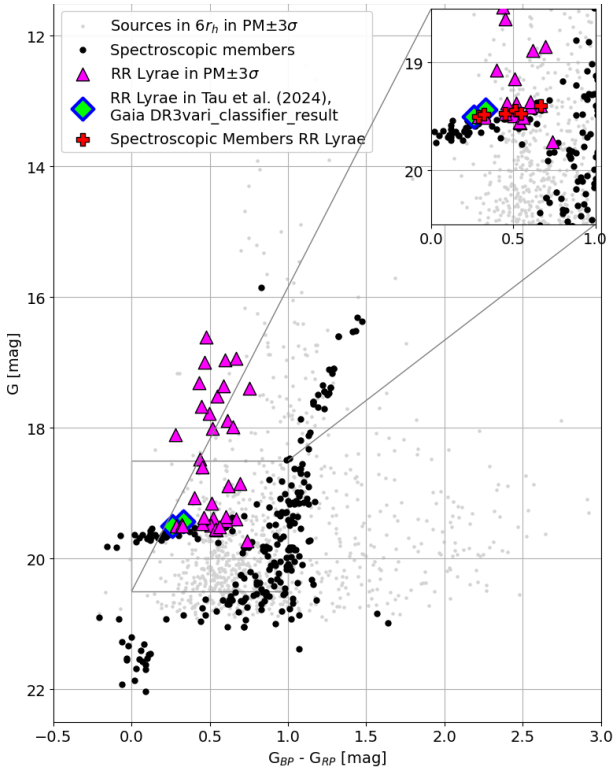

Figure 14: Color-magnitude diagram of Boötes I after proper motion selection. Spectroscopic members (black dots) delineate a well-defined stellar population sequence. Many RR Lyrae stars (magenta triangles) are found along the horizontal branch, as are the two stars included in the *Gaia* `gaiadr3.vari_classifier_result` catalogue (green diamonds).

The PWZ relation provides a robust membership criterion, as it embeds the metallicity and distance modulus characteristics of the host system. Figure 15 presents a Period-Wesenheit (Pw) diagram for the sample of 16 RR Lyrae stars that remain after the 3σ selection, comprising 6 RRab and 10 RRc types.

For *Gaia* DR3 1230819704412148224 listed in the *Gaia* `gaiadr3.vari_classifier_result` table, the pulsation period P = 0.302 days - derived from Pan-STARRS1[15] and also reported in Tau et al. (2024) - was adopted, as it is also confirmed by the analysis of the *Gaia* DR3 time series data for the star.
For *Gaia* DR3 1230713292302089728, Figure 17 shows the $G_{\rm BP}$, G and $G_{\rm RP}$ light curves, folded with P = 0.376 days. This period was derived from the analysis of the *Gaia* DR3 time series, but was not included in the *Gaia* `gaiadr3.vari_rrlyrae` table. The period reported in the literature (P ≈ 0.75 days) differs significantly, leading to a classification as an RRab star; however, this is not supported by the *Gaia* DR3 time series analysis, which instead favors a classification as RRc star.
By adopting these period values, both stars are classified as RRc-type variables and fall within the PWZ relation, as shown by the green diamonds in Fig. 15. They can therefore be considered candidate RR Lyrae members of Boötes I.

The left panel of Fig. 16 illustrates that some stars from the Sagittarius Stream fall within the PWZ relation. Nevertheless, almost all of them have [Fe/H] > -2.0 dex, making it unlikely that they belong to Boötes I ([Fe/H] = − 2.59 dex). On the other hand, three stars have [Fe/H] $<$ − 2.0 dex (Muraveva et al. 2025a) and could therefore be associated with Boötes I (cyan stars in FIg. 16): *Gaia* DR3 1230741020611316224, *Gaia* DR3 1231507655093621632, and *Gaia* DR3 1230836437604328704. The latter was also identified as member through spectroscopy by Waller et al. (2023), and - together with the other spectroscopic members -, it is well located within the PWZ relation, as shown in Fig. 15.

Tau et al. (2024) also considers *Gaia* DR3 1230914571649196544 source, which lies slightly outside the PWZ relation (right panel of Fig. 16). This star could still be a potential member in the case that the parameters of the UFD (such as distance modulus, metallicity, etc.) or the *Gaia* photometry are not entirely accurate.

[15] `https://www2.ifa.hawaii.edu/research/Pan-STARRS.shtml`

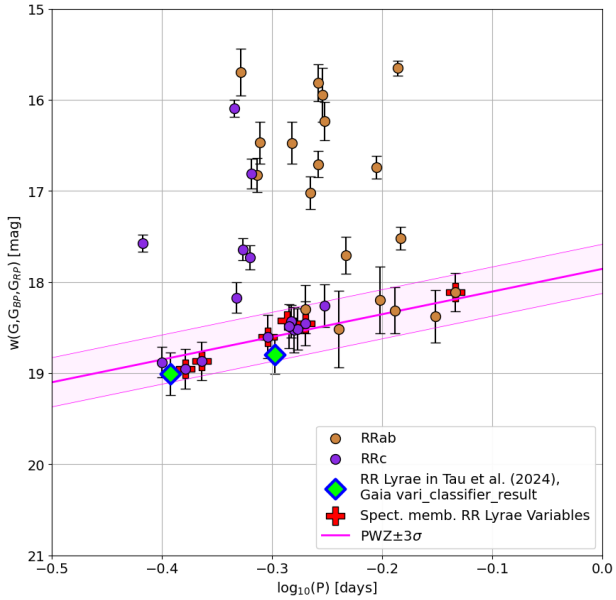

Figure 15: Pw diagram of RR Lyrae stars in Boötes I. The magenta solid line with $\pm 3\sigma$ bands shows the PWZ relation for RR Lyrae stars by Garofalo et al. (2022) shifted according to the distance modulus of Boötes I. RRab-type stars in brown; RRc-type stars in purple, whose periods have been *fundamentalized* (see Chapter 2); green diamonds (with blue edges) are the two stars in *Gaia* `gaiadr3.vari_classifier_result` catalogue also listed in Tau et al. (2024); red crosses are RR Lyrae spectroscopic members in Waller et al. (2023).

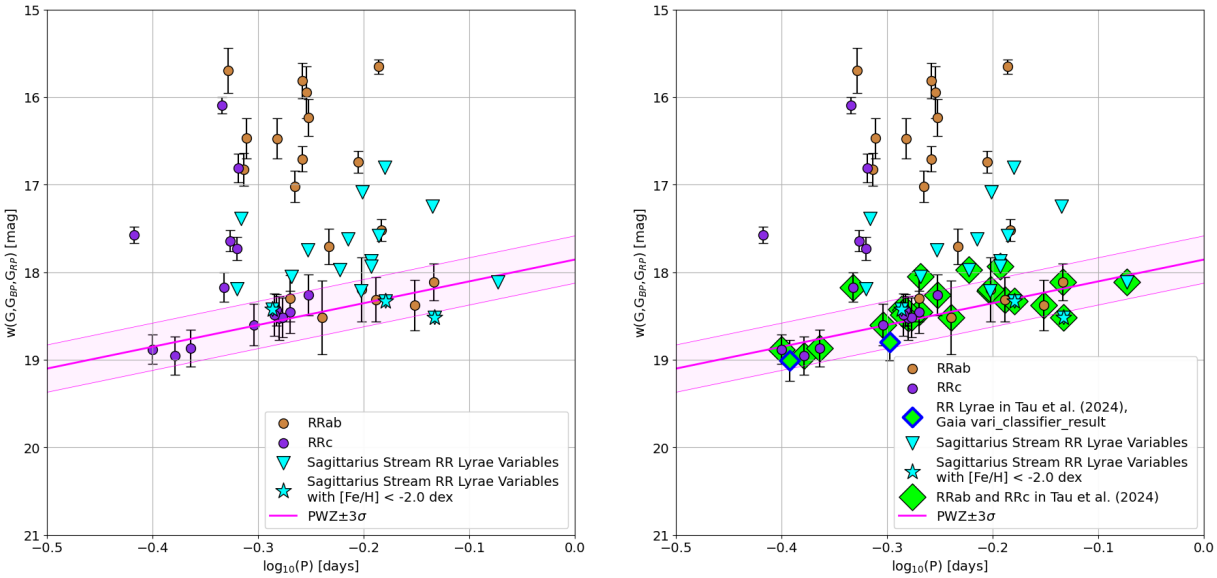

Figure 16: Pw diagrams of RR Lyrae stars (same as in Fig. 15), together with RR Lyrae stars from the Sagittarius Stream (cyan triangles; those which have [Fe/H] < -2.0 dex are marked with star $\star$ symbols) and RR Lyrae classified as Boötes I members by Tau et al. (2024) (**right panel**).

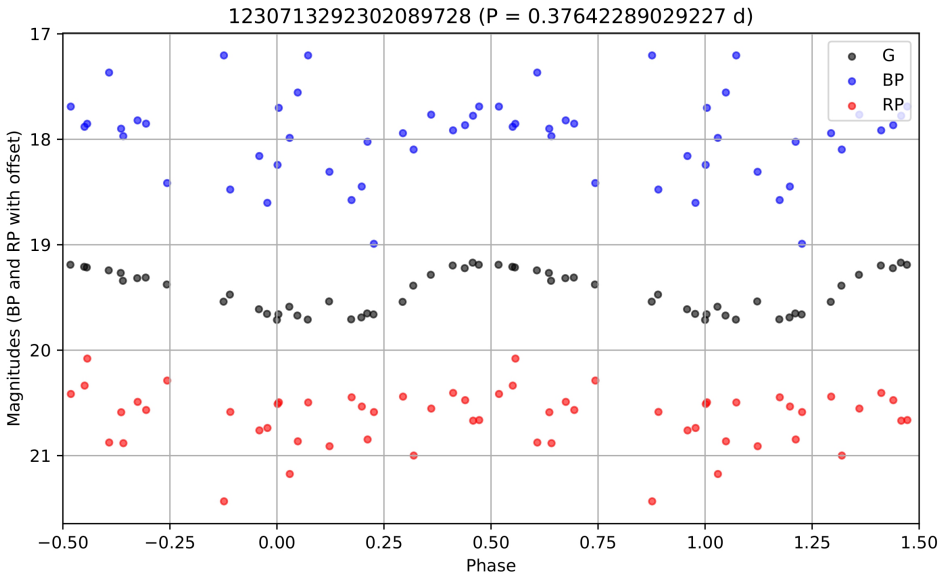

Figure 17: Light-curves of *Gaia* DR3 1230713292302089728 in the G_{BP}, G and G_{RP} bands. The G_{BP} and G_{RP} magnitudes in the plot have been offset by -1.5 mag and $+1.5$ mag, respectively.

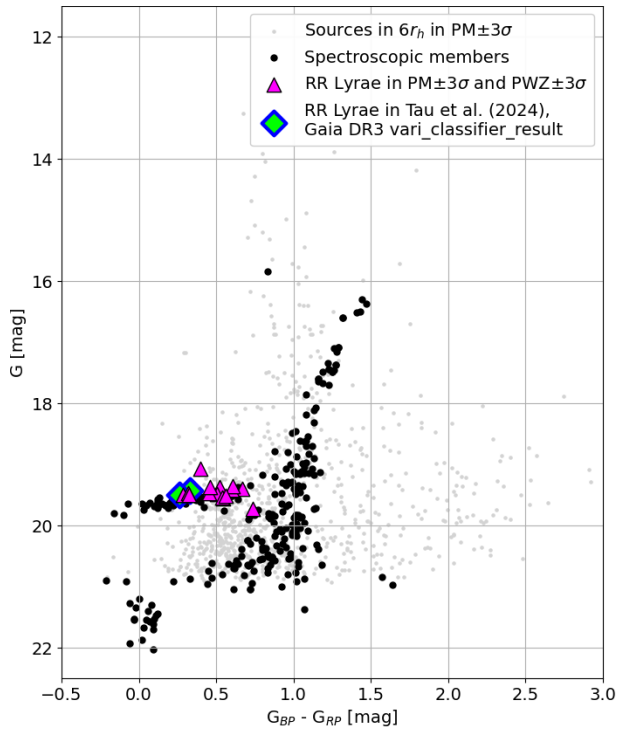

Figure 18: Color-magnitude diagram of Boötes I after applying proper motion and PWZ selections to RR Lyrae stars.

In the CMD, after applying both the proper motion and PWZ selections, the remaining RR Lyrae stars are placed well along the HB, as shown in Fig. 18. Only two stars slightly deviate: one appears brighter and the other is fainter than the expected locus. They are discussed in the following Chapter 3.1.3.

3.1.3 Reverse filtering via the PWZ relation

Repeating the analysis by applying only the PWZ selection - without any cut in proper motion - (left panel of Fig. 19) still yields the same 16 RR Lyrae stars previously identified with both criteria, together with the two sources in *Gaia* `gaiadr3.vari_classifier_result` catalogue. This confirms the robustness of the PWZ-based selection.

An investigation was also conducted into the possibility that some of the RR Lyrae stars might instead be ACEPs. As shown in the right panel of Fig.19, three RR Lyrae stars fall within the Period-Wesenheit relation for fundamental-mode ACEPs (ACEP-F), while eight align with that of first-overtone ACEPs (ACEP-1O). Upon inspection of the CMD in the left panel of Fig.20, only the *Gaia* DR3 source 1230519198435520128 emerges as an ACEP-F candidate, as it appears brighter than the others. However, since the star also lies within the PWZ relation for RR Lyrae stars, the RR Lyrae classification is considered more likely. Improved astrometry and photometry expected from *Gaia* DR4 will allow for a more definitive classification.

A similar situation arises with *Gaia* DR3 source 1226522469372990208, which is approximately 0.3 mag fainter than the other RR Lyrae stars located on the horizontal branch. Given that, this source also fits both the proper motion and PWZ relations for RR Lyrae stars, it is likely that significant uncertainties in the G-band magnitude contribute to this discrepancy.

The final proper motion distribution of the RR Lyrae candidate members of Boötes I is shown in Fig. 21 and their spatial distribution is shown in the right panel of Fig. 20. The complete catalogue of the selected RR Lyrae variables is shown in Tab. 4.

In conclusion, 18 RR Lyrae stars can be considered likely candidates for membership in Boötes I, as they satisfy both the proper motion and PWZ relation selection criteria. One of these stars requires further investigation, as it falls within the Period-Wesenheit (PW) relation for fundamental-mode Anomalous Cepheids (ACEP-F); however, this is likely due to a photometric error. Additionally, three RR Lyrae stars have been associated with the Sagittarius Stream according to Muraveva et al. (2025a), but their low metallicity suggests they may instead belong to the Boötes I system. One of these stars is also spectroscopically confirmed as a member by Waller et al. (2023), and should be re-evaluated using the improved data from *Gaia* DR4.

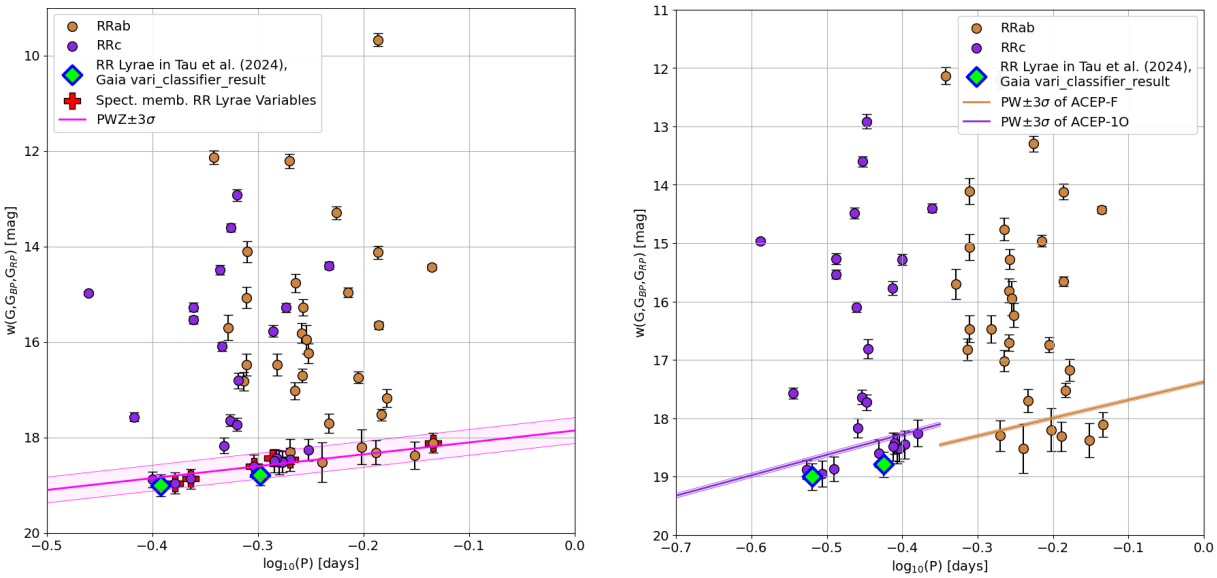

Figure 19: Pw diagram of RR Lyrae stars in Boötes I, without proper motion selection. The magenta solid line with $\pm 3\sigma$ bands shows the PWZ relation for RR Lyrae stars by Garofalo et al. (2022) (**left panel**), while in the **right panel** in brown is shown the PW relation for ACEP-F stars, and in purple is shown that for ACEP-1O stars (Ripepi et al. 2023). All the relations are shifted according to the distance modulus of Boötes I.

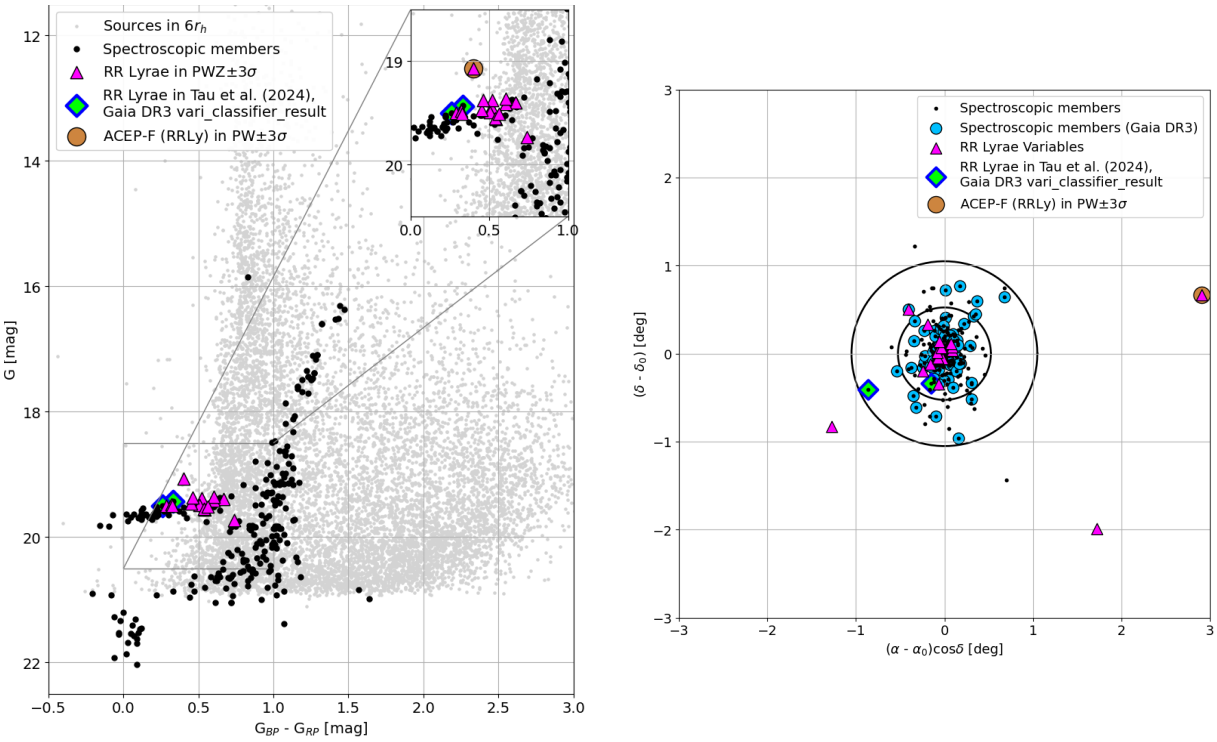

Figure 20: Left: Color-magnitude diagram after PWZ selection applied to RR Lyrae stars. All RR Lyrae stars (magenta triangles) are located along the horizontal branch. The ACEP-F candidate is shown with brown dot. **Right:** Spatial distribution of member stars identified through spectroscopy (black and light-blue dots) together with the RR Lyrae and ACEP-F candidate members of Boötes I (magenta triangles and brown dot, respectively). Black circles: 1, 3, 6 r_h around the centre.

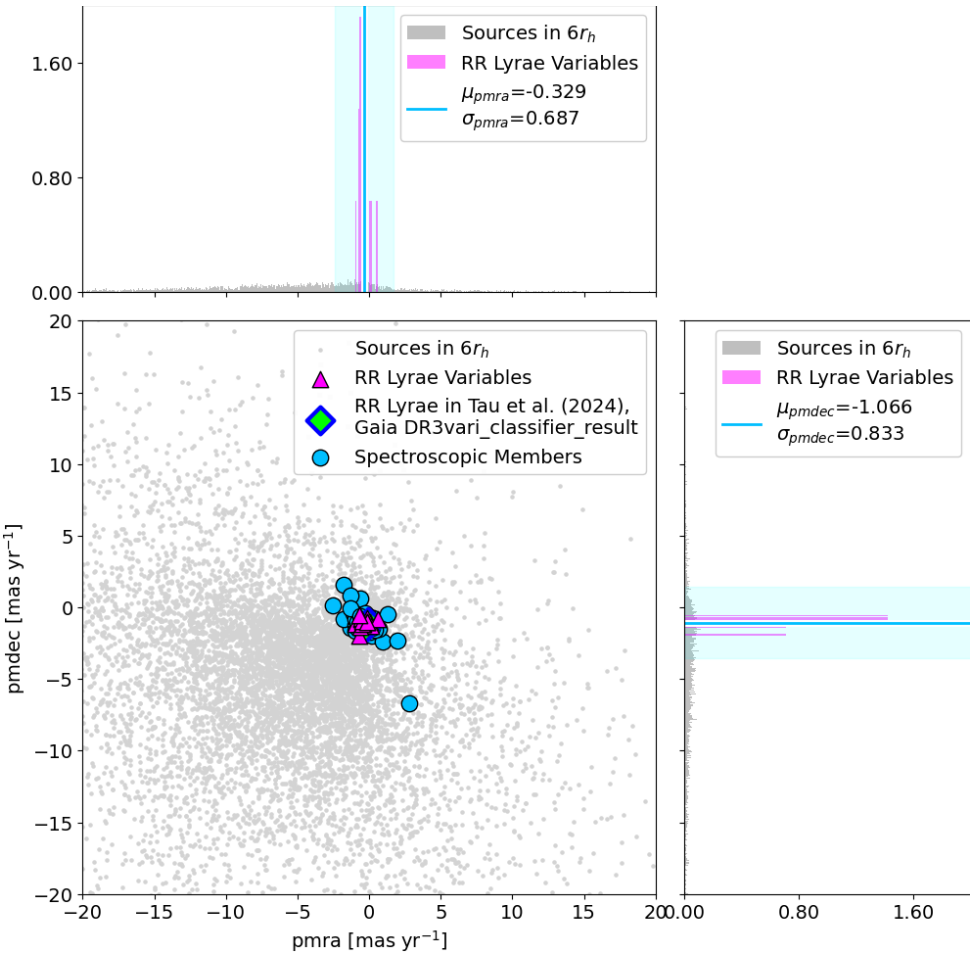

Figure 21: Proper motion distribution of RR Lyrae stars considered candidate members of Boötes I. The candidates from the `gaiadr3.vari_rrlyrae` catalogue (magenta triangles) are overplotted with those from the `gaiadr3.vari_classifier_result` catalogue (green diamonds with blue edges) and they are all consistent with the mean proper motions.

Table 4: Properties of Boötes I RR Lyrae Variables identified through multi-method approach compared with literature.

Boötes I													
source_id	RA (deg)	Dec (deg)	pmra (mas/yr)	pmdec (mas/yr)	G (mag)	G_{BP} (mag)	G_{RP} (mag)	Class.	S.M.	Tau et al. (2024)	PM + PWZ	PWZ	ACEP
1230850009701023232	209.964	14.652	-0.651	-1.332	19.504	19.631	19.345	RRc	Y	Y	Y	Y	-
1231064517547444736	209.613	15.014	-0.452	-0.925	19.470	19.661	19.208	RRc	Y	Y	Y	Y	ACEP-1O[1]
1230827538432572416	209.857	14.396	-0.128	-0.998	19.397	19.764	19.096	RRab	Y	Y	Y	Y	-
1230772597210842624	209.956	14.168	0.117	-1.277	19.440	19.669	19.156	RRc	Y	Y	Y	Y	ACEP-1O[1]
1230836437604328704	210.037	14.573	-0.989	-0.793	19.475	19.639	19.093	RRc	Y[3,5]	Y[3,5]	-	-	-
1230859630427736832	210.112	14.593	-0.582	-0.776	19.482	19.582	19.261	RRc	Y	Y	Y	Y	-
1226522469372990208	211.742	12.521	0.034	-1.035	19.731	20.048	19.310	RRab	-	Y	Y	Y	-
1230519198435520128	212.925	15.179	-0.170	-0.769	19.068	19.111	18.711	RRab	-	-	Y	Y	ACEP-F[2]
1230825339409289600	209.776	14.317	-0.969	-1.128	19.377	19.678	19.158	RRab	-	Y	Y	Y	-
1230833517027065728	209.999	14.459	-0.723	-0.532	19.415	19.673	19.071	RRc	-	Y	Y	Y	ACEP-1O[1]
1230834135502357632	209.947	14.466	0.595	-0.838	19.561	19.709	19.167	RRab	-	Y	Y	Y	ACEP-F[1]
1230834925776358912	209.941	14.528	-0.549	-0.806	19.493	19.715	19.210	RRc	-	Y	Y	Y	ACEP-1O[1]
1230835853488763008	210.107	14.552	-0.408	-1.146	19.359	19.677	19.073	RRab	-	Y	Y	Y	ACEP-F[1]
1230848326073809280	209.983	14.582	-0.724	-1.939	19.549	19.791	19.253	RRc	-	Y	Y	Y	ACEP-1O[1]

[1] = RR Lyrae stars which fall in the PW relation for Anomalous Cepheids (ACEP-F and ACEP-1O), however they are likely RR Lyrae stars.
[2] = RR Lyrae star which can be Anomalous Cepheid (ACEP-F) candidate, but further investigation is required.
[3] = RR Lyrae star from the Sagittarius Stream which is also classified as Boötes I member by Waller et al. (2023); it has [Fe/H] < -2.0 dex.
[4] = RR Lyrae stars from the Sagittarius Stream classified by Tau et al. (2024) as Boötes I members.
[5] = RR Lyrae stars from the Sagittarius Stream with [Fe/H] < -2.0 dex.
[6] = RR Lyrae star classified by Tau et al. (2024), but not obtained through the multi-method approach since it does not fall in the PWZ relation, found only if the distance modulus in Vivas et al. (2020) or the *Gaia* DR3 photometry are not correct.
[7] = Sources in *Gaia* `gaiadr3.vari_classifier_result` catalogue which are RR Lyrae candidates, they fall within the PWZ selection if the period in literature (see Chapter 3.1.2) is taken into account.

Tab. 4 continued.

Boötes I													
source_id	RA (deg)	Dec (deg)	pmra (mas/yr)	pmdec (mas/yr)	G (mag)	G_{BP} (mag)	G_{RP} (mag)	Class.	S.M.	Tau et al. (2024)	PM + PWZ	PWZ	ACEP
1230860695583613824	210.090	14.625	-0.504	-1.129	19.512	19.682	19.120	RRc	-	Y	Y	Y	ACEP-1O[1]
1231067163247260160	209.827	14.848	-0.145	-1.025	19.508	19.604	19.277	RRc	-	Y	Y	Y	ACEP-1O[1]
3728695065116355456	208.745	13.688	-0.662	-0.530	19.374	19.623	19.161	RRc	-	Y	Y	Y	ACEP-1O[1]
1243152071642576896	208.673	15.303	-1.479	-0.040	19.266	19.533	18.983	RRab	-	Y[4]	-	-	-
1229801659723433600	210.670	13.051	-1.331	-0.390	19.138	19.357	18.750	RRab	-	Y[4]	-	-	-
1230741020611316224	209.518	14.222	-0.501	-0.492	19.445	19.662	19.081	RRab	-	Y[5]	-	-	-
1230829771815569536	210.046	14.405	-0.733	-0.787	19.342	19.615	18.976	RRab	-	Y[4]	-	-	-
1230914571649196544	208.645	14.204	-1.177	-0.586	19.150	19.418	18.908	RRc	-	Y[6]	-[6]	-[6]	-
1231507655093621632	210.418	15.680	-1.320	-0.374	19.474	19.708	19.209	RRab	-	Y[5]	-	-	-
3728687334175665920	208.520	13.571	-0.928	-0.631	19.168	19.419	18.776	RRab	-	Y[4]	-	-	-
1230612927506112000	209.610	13.466	-0.993	-0.398	19.100	19.435	18.888	RRab	-	Y[4]	-	-	-
1230713292302089728	209.157	14.106	-0.063	-0.998	19.432	19.451	19.119	RRc[7]	-	Y	-[7]	-[7]	-
1230819704412148224	209.872	14.179	-0.271	-1.422	19.502	19.623	19.364	RRc[7]	-	Y	-[7]	-[7]	-

[1] = RR Lyrae stars which fall in the PW relation for Anomalous Cepheids (ACEP-F and ACEP-1O), however they are likely RR Lyrae stars.
[2] = RR Lyrae star which can be Anomalous Cepheid (ACEP-F) candidate, but further investigation is required.
[3] = RR Lyrae star from the Sagittarius Stream which is also classified as Boötes I member by Waller et al. (2023); it has [Fe/H] < -2.0 dex.
[4] = RR Lyrae stars from the Sagittarius Stream classified by Tau et al. (2024) as Boötes I members.
[5] = RR Lyrae stars from the Sagittarius Stream with [Fe/H] < -2.0 dex.
[6] = RR Lyrae star classified by Tau et al. (2024), but not obtained through the multi-method approach since it does not fall in the PWZ relation, found only if the distance modulus in Vivas et al. (2020) or the *Gaia* DR3 photometry are not correct.
[7] = Sources in *Gaia* `gaiadr3.vari_classifier_result` catalogue which are RR Lyrae candidates, they fall within the PWZ selection if the period in literature (see Chapter 3.1.2) is taken into account.

3.1.4 Clustering Algorithms

Boötes I was chosen as the starting point for applying the clustering algorithms because it represents one of the most interesting cases among the UFDs analysed in this work. It exhibits clear evidence of both contamination from the Sagittarius Stream and the presence of RR Lyrae stars listed in the `gaiadr3.vari_classifier_result` catalogue. Moreover, Boötes I can be considered as an intermediate case between the sparsely populated Sagittarius II and the more complex Boötes III.

As mentioned in Chapter 2.7, a sample of the *Gaia* `gaiadr3.vari_rrlyrae` catalogue was selected, including only sources with magnitudes $G > 18$ mag.
The initial aim was to determine whether - using standard parameter values for the clustering algorithms - it would be possible to recover the same 16 RR Lyrae stars - coming from the `vari_rrlyrae` catalogue - previously identified as candidate members of Boötes I. To this purpose, a first test was conducted with default parameters: for DBSCAN, `eps = 0.04` and `min_samples = 5`; for HDBSCAN, `min_cluster_size = 5` and `min_samples = 5`.
In both cases, the resulting clusters contained 9 out of the 16 reference RR Lyrae stars, which had been previously selected based on proper motion and the PWZ relation (Fig. 22). The corresponding cluster labels are reported in Tab. 5.

Subsequently, the algorithms were optimized for detecting stellar populations with significantly fewer confirmed members. After several trials, a parameter combination was found that maximized the recovery of the reference sample: specifically, `eps = 0.04` and `min_samples = 2` for DBSCAN, and `min_cluster_size = 4` and `min_samples = 4` for HDBSCAN. This configurations resulted in identifying 12 out of the 16 target RR Lyrae stars (Fig. 23).

During this process, it was noted that, for both algorithms, the *Gaia* DR3 source 1230825339409289600 consistently appeared in a separate cluster (label = 776 with DBSCAN, or label = 1625 with HDBSCAN) from the majority (label = 3364 with DBSCAN, or label = 1098 with HDBSCAN). A closer inspection of this secondary cluster revealed that both DBSCAN and HDBSCAN, despite identifying different numbers of members, consistently associated this group with RR Lyrae stars classified as part of the Sagittarius Stream (Muraveva et al. (2025a), Fig. 24).

It is worth mentioning that the spectroscopic member *Gaia* DR3 1230836437604328704 appears more likely to be associated with the Sagittarius Stream (see Tab. 5), rather than being clustered with the 12 objects - likely Boötes I candidate members - found with the clustering algorithms. However, further investigation and refinement of the machine learning techniques will be necessary to confirm this classification.

In conclusion, 15 RR Lyrae stars have been associated with the same label (3364 in DBSCAN, 1098 in HDBSCAN), including some of the 16 identified through the multi-method approach, as well as others listed in Tau et al. (2024) (see Tab. 5 compared with Tab. 4).

The results of these tests suggest that clustering algorithms are effective in detecting both dense and extended stellar structures, such as the Sagittarius Stream, as well as much sparser populations, like the RR Lyrae stars potentially belonging to UFD galaxies. This represents an initial, exploratory step toward evaluating how clustering methods can aid in identifying members of faint stellar systems.

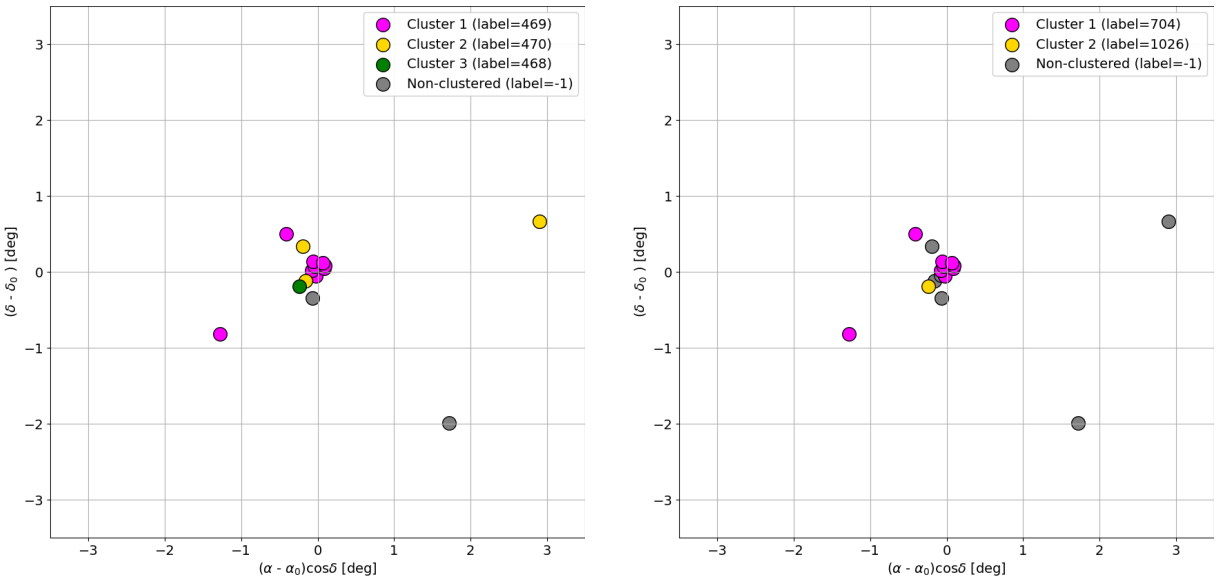

Figure 22: Left: Spatial distribution of the 16 RR Lyrae stars from the `vari_rrlyrae` catalogue identified as candidate members of Boötes I, assigned to different clusters (labels = 469, 470, 468, -1) based on the initial DBSCAN test (`eps = 0.04`, `min_samples = 5`). **Right:** Spatial distribution of the 16 RR Lyrae stars from the `vari_rrlyrae` catalogue identified as candidate members of Boötes I, assigned to different clusters (labels = 704, 1026, -1) based on the initial HDBSCAN test (`min_cluster_size = 5`, `min_samples = 5`).

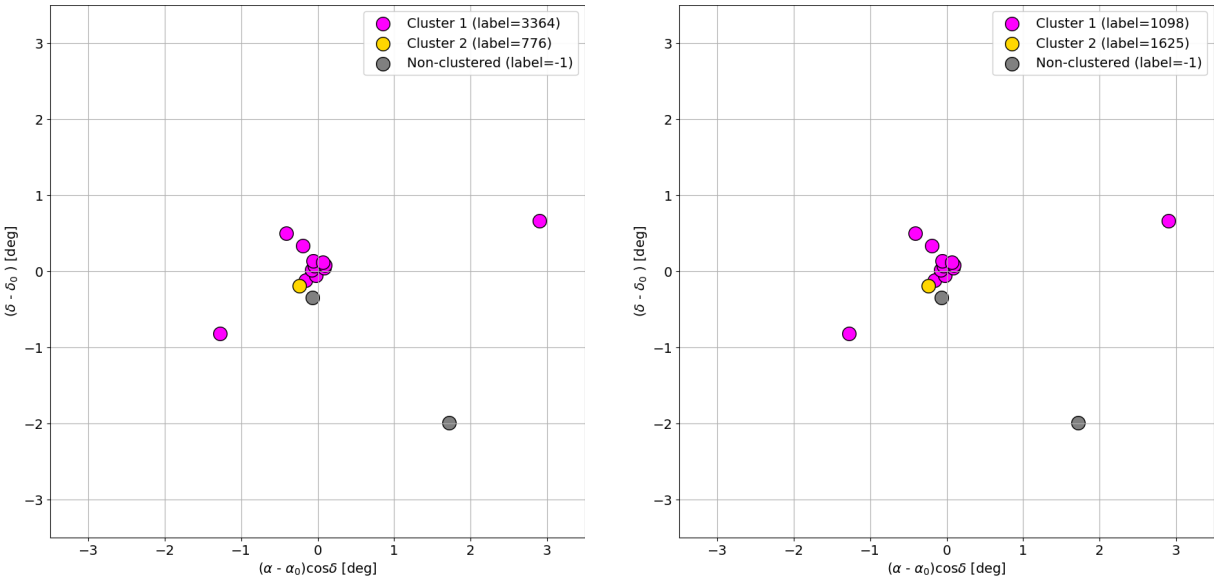

Figure 23: Left: Spatial distribution of the 16 RR Lyrae stars from the `vari_rrlyrae` catalogue identified as candidate members of Boötes I, assigned to different clusters (labels = 3364, 776, -1) based on the optimized DBSCAN test (`eps = 0.04`, `min_samples = 2`). **Right:** Spatial distribution of the 16 RR Lyrae stars from the `vari_rrlyrae` catalogue identified as candidate members of Boötes I, assigned to different clusters (labels = 1098, 1625, -1) based on the optimized HDBSCAN test (`min_cluster_size = 4`, `min_samples = 4`).

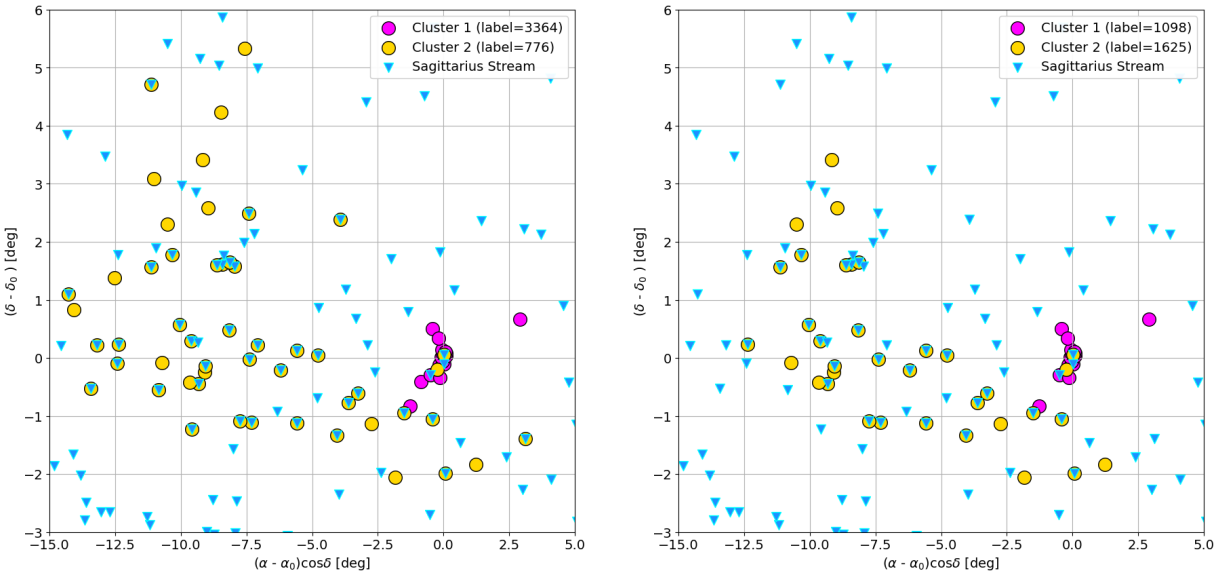

Figure 24: Left: Spatial distribution of the RR Lyrae stars within the clusters with labels = 3364 (magenta), 776 (yellow), in the optimized DBSCAN test (`eps = 0.04`, `min_samples = 2`). Comparison with Sagittarius Stream RR Lyrae stars in Muraveva et al. (2025a) (blue triangles). **Right:** Spatial distribution of the RR Lyrae stars within the clusters with labels = 1098 (magenta), 1625 (yellow), in the optimized HDBSCAN test (`min_cluster_size = 4`, `min_samples = 4`). Comparison with Sagittarius Stream RR Lyrae stars in Muraveva et al. (2025a) (blue triangles).

Table 5: Labels of DBSCAN and HDBSCAN tests associated with RR Lyrae variables of Boötes I (see Tab. 4 for comparison).

Boötes I				
source_id	Test 1 DBSCAN	Test 1 HDBSCAN	Test 2 DBSCAN	Test 2 HDBSCAN
1230850009701023232	469	704	3364	1098
1231064517547444736	469	704	3364	1098
1230827538432572416	470	-1	3364	1098
1230772597210842624	-1	-1	-1	-1
1230836437604328704	468[1]		776[1]	1635[1]
1230859630427736832	469	704	3364	1098
1226522469372990208	-1	-1	-1	-1
1230519198435520128	470	-1	3364	1098
1230825339409289600	468	1026	776	1625
1230833517027065728	469	704	3364	1098
1230834135502357632	-1	-1	-1	-1
1230834925776358912	469	704	3364	1098
1230835853488763008	469	704	3364	1098
1230848326073809280	469	704	3364	1098

[1] = RR Lyrae stars associated with a cluster outside the set of 16 candidate members of Boötes I identified via proper motion and the PWZ relation.

Tab. 5 continued.

Boötes I				
source_id	Test 1 DBSCAN	Test 1 HDBSCAN	Test 2 DBSCAN	Test 2 HDBSCAN
1230860695583613824	469	704	3364	1098
1231067163247260160	470	-1	3364	1098
3728695065116355456	469	704	3364	1098
1243152071642576896				
1229801659723433600				
1230741020611316224	469[1]	704[1]	3364[1]	1098[1]
1230829771815569536	469[1]	704[1]	3364[1]	1098[1]
1230914571649196544				
1231507655093621632				
3728687334175665920	468[1]	1026[1]	776[1]	1625[1]
1230612927506112000	468[1]	1026[1]	776[1]	1625[1]
1230713292302089728	470[1]		3364[1]	
1230819704412148224	469[1]		3364[1]	1098[1]

[1] = RR Lyrae stars associated with a cluster outside the set of 16 candidate members of Boötes I identified via proper motion and the PWZ relation.

3.2 Boötes III

Boötes III is a faint and enigmatic stellar system in the Galactic halo, first identified by Grillmair (2009) as a diffuse overdensity of stars embedded within the Styx stellar stream (Carlin et al. 2018). Detected in the Sloan Digital Sky Survey data, Boötes III appears as a ∼1 kpc-wide concentration of stars at a heliocentric distance of ∼45 kpc, exhibiting a color-magnitude diagram consistent with an old, metal-poor population. Its irregular morphology, extremely low surface brightness, and positional coincidence with the Styx stream suggest that Boötes III may be the progenitor of this stellar stream and is currently undergoing tidal disruption, potentially in the final stages of dissolution.

Subsequent studies, including Carlin et al. (2018), have provided crucial dynamical constraints using astrometric data from *Gaia* DR2. By selecting 15 spectroscopically confirmed members, along with a likely RR Lyrae variable, they measured a mean proper motion consistent with a highly eccentric, retrograde orbit. The derived orbital parameters show that Boötes III passed within ∼12 kpc of the Galactic center approximately 140 Myr ago. This close pericentric passage, combined with its structural and kinematic properties, supports the scenario that Boötes III is a disrupting dwarf galaxy responsible for generating the Styx stellar stream. Moreover, the agreement between the observed proper motion and that predicted for Styx further strengthens the physical association between the two systems. The presence of contaminating stars, particularly from the nearby disrupting globular cluster NGC 5466, complicates membership attribution, highlighting the importance of spectroscopic confirmation in disentangling Bootes III's stellar population.

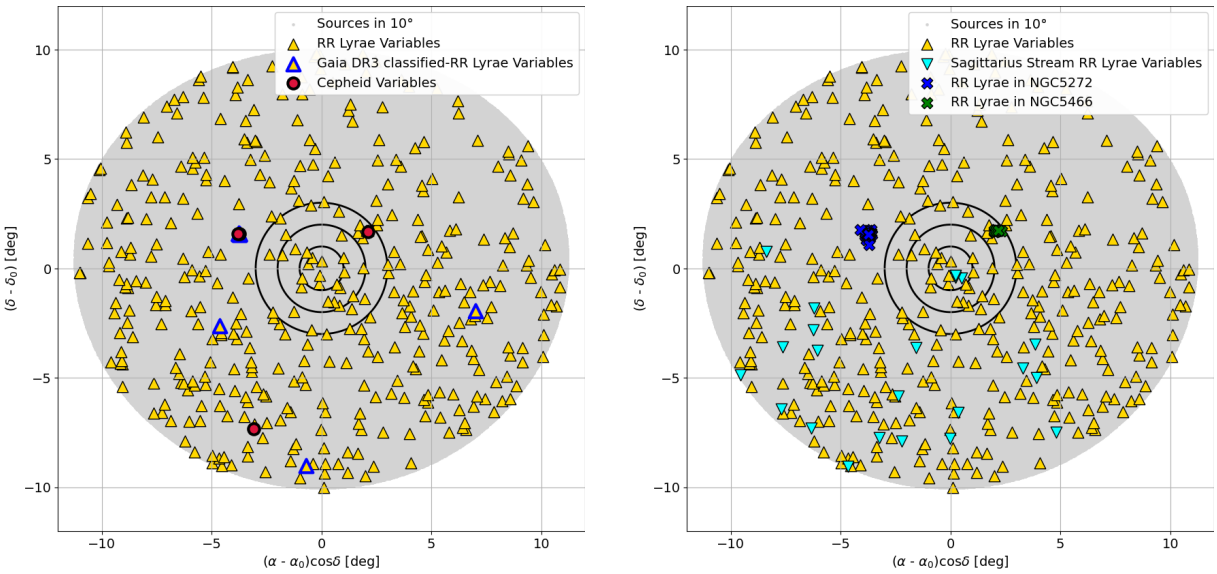

Figure 25: Left: Spatial distribution of sources (grey dots), RR Lyrae variables (yellow triangles), RR Lyrae candidates in the *Gaia* `gaiadr3.vari_classifier_result` catalogue (yellow triangles with blue edges) and Cepheid variables (red dots) within 10° around the centre of Boötes III. Black circles: 1, 2, 3 r_h around the centre. **Right:** Same as in the left panel with spatial distribution of contamination sources. Cyan triangles: Sagittarius Stream RR Lyrae stars. Blue crosses: RR Lyrae stars in NGC5272. Green crosses: RR Lyrae in NGC5466.

3.2.1 Spatial distribution and mapping of stellar population

Six hundred and twenty seven RR Lyrae variables are located within a 10° radius from the centre of Boötes III (Fig. 25 and color-map in the left panel of Fig. 26). Among them, 16 were labeled in the *Gaia* `gaiadr3.vari_classifier_result` catalogue. Except for three, all of these classified-variables are spatially aligned with the globular cluster NGC5272 (M3), suggesting they may be cluster members. In this region, four Cepheid variables were identified: two fundamental-mode Classical Cepheids (DCEP-F), one Classical Cepheid pulsating in the first overtone (DCEP-1O), and one Type II Cepheid (T2C). Three of these Cepheid stars are also well aligned with the spatial positions of NGC5272 and NGC5466 (right

panel of Fig. 25), raising the possibility that they are members of those clusters, despite having proper motions similar to those of Boötes III.

Twenty-two RR Lyrae stars from the Sagittarius stream are present in the same area. To avoid contamination, these were excluded, reducing the total number of RR Lyrae variables in the initial sample to 605.

As mentioned in Chapter 2, the presence of the globular clusters NGC5272 and NGC5466 in this field was investigated: they host 195 and 19 RR Lyrae stars, respectively.

In Tau et al. (2024), 32 RR Lyrae stars are associated with Boötes III. However, five of them are also classified as members of the Sagittarius Stream and were therefore excluded from the working sample. In Carlin et al. (2018), Boötes III members identified via spectroscopy were matched to *Gaia* DR2 sources. Since the source identifiers (`source_id`) change across *Gaia* data releases, a cross-match in coordinates with *Gaia* DR3 was made. This process yielded 39 stars identified as Boötes III spectroscopic members, including three RR Lyrae stars. Of them, two were also classified as Sagittarius Stream members and were thus excluded from further analysis (right panel of Fig. 26).

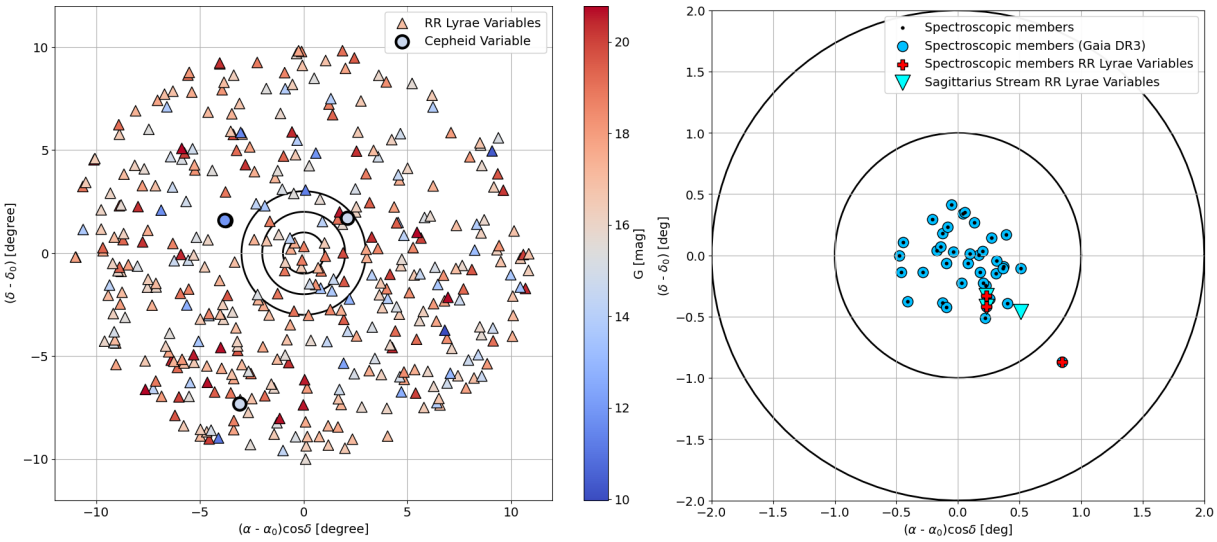

Figure 26: Left: *G*-band color-map of RR Lyrae and Cepheid stars within 10° around the centre of Boötes III. **Right:** Spatial distribution of member stars identified through spectroscopy. Black dots: members identified by Carlin et al. (2018). Light-blue dots: members also catalogued in *Gaia* DR3. Red crosses: RR Lyrae spectroscopic members. Cyan triangles: Sagittarius Stream RR Lyrae stars.

3.2.2 Proper Motion and Period-Wesenheit-Metallicity Relation selections

An initial filtering step excluded variable stars with proper motion uncertainties greater than 0.5 mas yr^{-1}, resulting in the removal of 23 sources (Fig. 27).

A preliminary proper motion analysis was conducted to assess potential contamination from the nearby globular clusters NGC5272 (M3) and NGC5466. As mentioned, some Cepheid variables were found at positions overlapping the projected locations of these clusters: *Gaia* DR3 1454784317416279168, *Gaia* DR3 1454784523573570816 seem to correspond to NGC5272, *Gaia* DR3 1452625254531322752 to NGC5466. Therefore, the mean proper motions of NGC5272 and NGC5466 were computed using their associated RR Lyrae stars and are shown in Fig. 28 and in Tab. 7. The results indicated that these Cepheid variables fall within the proper motion ranges of the two globular clusters, suggesting a likely association with the clusters (Tab. 6). However, the proper motion of the first two DCEP-F was also very similar to the average proper motion of Boötes III (Tab. 3), which complicates a reliable separation based solely on proper motion data. This underscores the challenges of member classification in overlapping regions and emphasizes the importance of considering both kinematic and spatial information when evaluating membership.

A 3σ selection around the average proper motion values was applied (Fig. 29), reducing the number of RR Lyrae stars to 217 and significantly narrowing down the total number of sources within $1r_h$ (Fig. 29). Also all the 13 RR Lyrae variables listed in the `gaiadr3.vari_classifier_result` catalogue passed this filtering, together with the two Cepheids associated with NGC5272 and the other DCEP.

The color-magnitude diagram analysis reveals that RR Lyrae stars selected based on proper motions exhibit a broad spread in the G mean magnitude (left panel of Fig. 30). This dispersion likely reflects the elongated structure of Boötes III, and the large search radius ($1\mathrm{r}_h \approx 1^\circ$) inevitably includes a considerable number of foreground and background sources. Therefore, applying the Period-Wesenheit-Metallicity (PWZ) relation is essential for more refined membership classification.

Nevertheless, it is clearly visible in the right panel of Fig. 30 that the RR Lyrae stars associated with NGC5272 and NGC5466 are located at G-band magnitudes significantly different from those expected for Boötes III, whose horizontal branch is found around 19 mag. It can be observed that the many sources in the `gaiadr3.vari_classifier_result` catalogue, in addition to being spatially aligned with NGC 5272, also share the same magnitude as the globular cluster horizontal branch (approximately 15.5 mag).

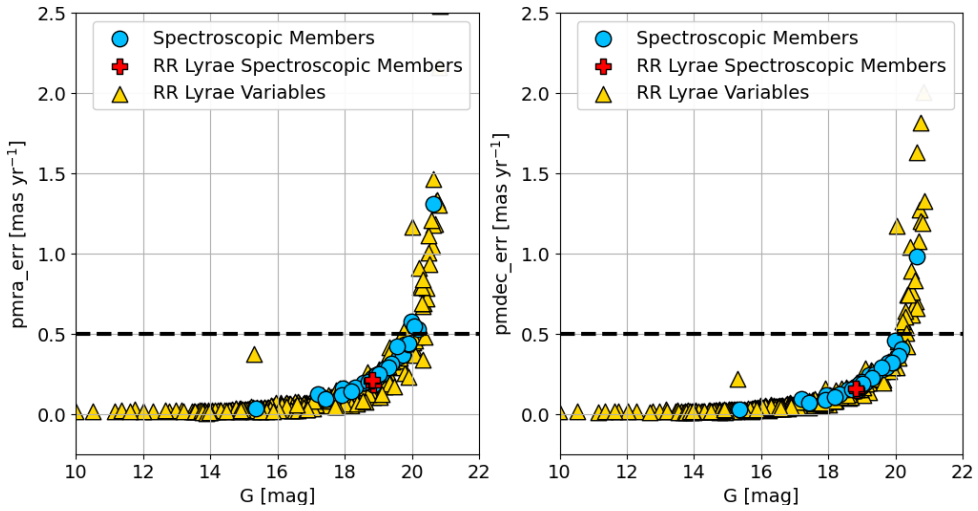

Figure 27: Proper motion errors of RR Lyrae stars (yellow triangles) and spectroscopic members (light-blue dots) within 10° around the centre of Boötes III as a function of G-band magnitude. All the RR Lyrae spectroscopic members (red crosses) are located below the 0.5 mas yr^{-1} (dashed) line.

Table 6: Properties of Cepheid variables within 10° around the centre of Boötes III.

source_id	**RA** (deg)	**Dec** (deg)	**pmra** (mas/yr)	**pmdec** (mas/yr)	**G** (mag)	**G$_{BP}$** (mag)	**G$_{RP}$** (mag)	**Class.**
1452625254531322752	211.419	28.487	-5.303	-0.770	14.686	14.862	14.471	DCEP
1454784317416279168	205.549	28.370	0.230	-2.700	12.427	12.542	11.811	DCEP
1454784523573570816	205.499	28.382	-0.166	-2.826	11.886	12.608	10.907	T2CEP
1248397910338129664	206.219	19.471	-0.213	-1.313	14.704	14.991	14.316	DCEP

Table 7: Mean proper motions of NGC5272 and NGC5466 computed with their RR Lyrae variables provided in Clement et al. (2001).

GC	**pmra** (mas/yr)	**pmdec** (mas/yr)
NGC5272	-0.083 ± 1.127	-2.690 ± 0.578
NGC5466	-5.343 ± 0.061	-0.811 ± 0.033

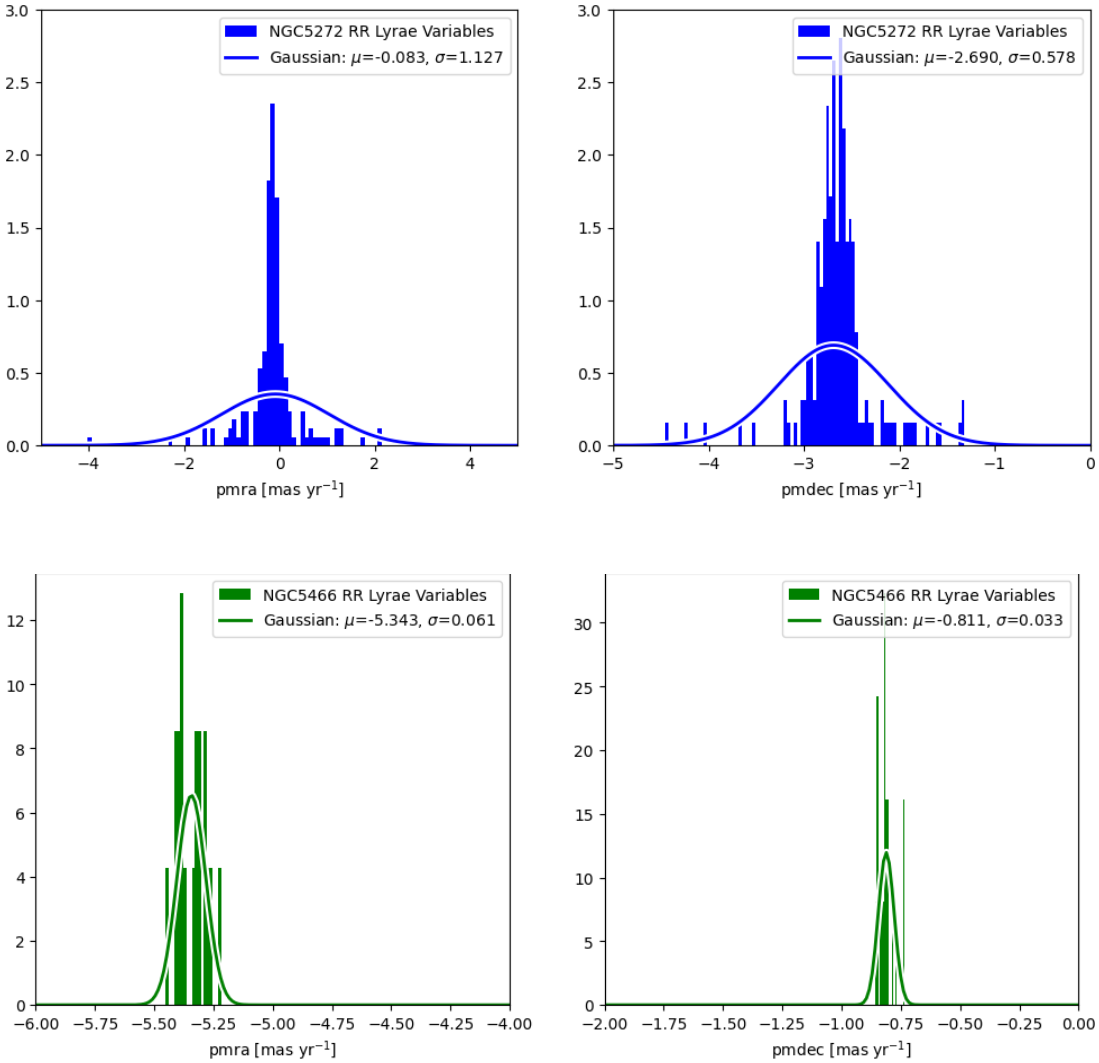

Figure 28: Upper panels: Proper motions (pmra on the left, pmdec on the right) of the RR Lyrae stars associated with NGC5272. **Lower panels:** Proper motions (pmra on the left, pmdec on the right) of the RR Lyrae stars associated with NGC5466.

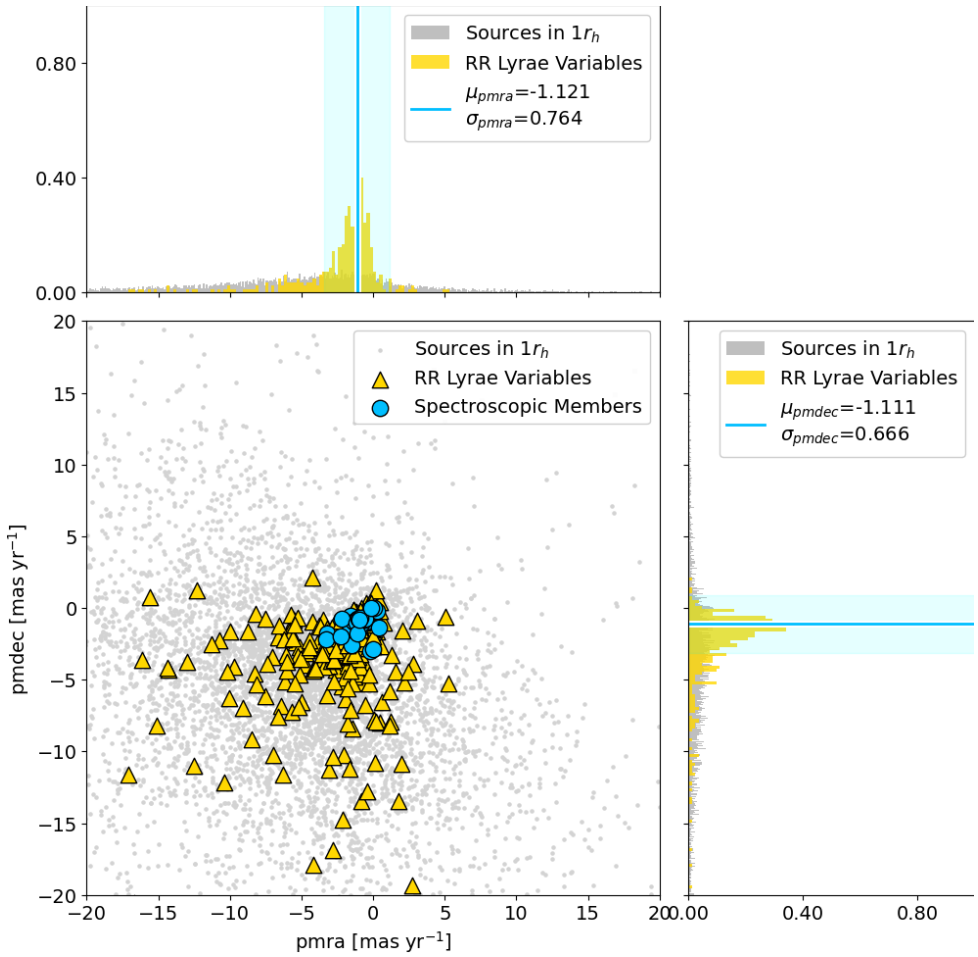

Figure 29: Proper motion distribution of sources within $1r_h$ (grey dots) and RR Lyrae stars within 10° (yellow triangles) around the centre of Boötes III. The cyan shaded bands correspond to $\pm 3\sigma$ of the mean proper motions (cyan lines) computed using the spectroscopic members (light-blue dots).

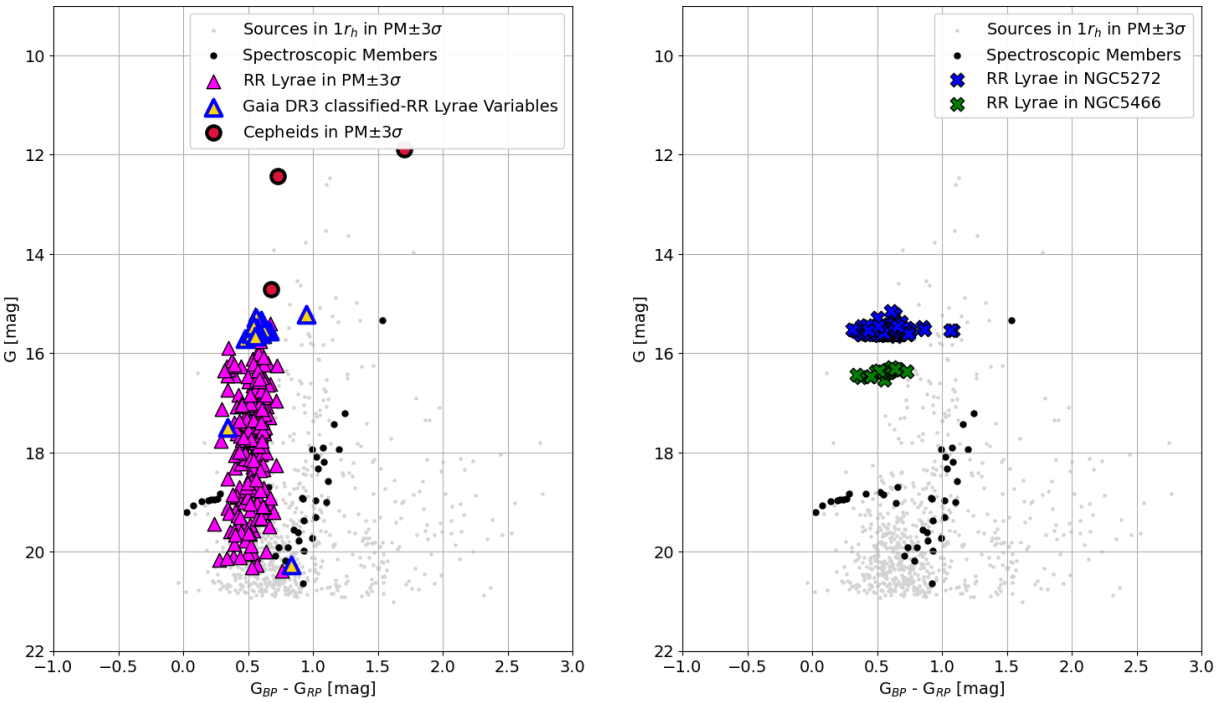

Figure 30: Left: Color-magnitude diagram of Boötes III after proper motion selection. Spectroscopic members (black dots) delineate a well-defined stellar population sequence. There is a wide spread in the G-band mean magnitude of RR Lyrae stars. **Right:** Color-magnitude diagram of Boötes III compared with the RR Lyrae stars associated with NGC5272 (blue) and NGC5466 (green).

After applying the PWZ relation selection, 38 RR Lyrae variables remain: 23 RRab, 13 RRc, and 2 RRd types (left panel of Fig. 31). Several RR Lyrae stars associated with the Sagittarius Stream also fall within the PWZ relation (right panel of Fig. 31). This may indicate overlapping physical properties or contamination between the two systems. A possible explanation should be explored. Of the 32 RR Lyrae stars from Tau et al. (2024), most are consistent with the PWZ relation, with only 7 lying outside it.

All the members confirmed through spectroscopy are well-distributed around the PWZ relation (left panel of Fig. 31), though two were excluded due to their classification as Sagittarius Stream stars. On the other hand, as expected, RR Lyrae stars belonging to NGC 5272 and NGC 5466 lie well above the PWZ relation shifted to the distance modulus of Boötes III, as shown in Fig. 32.

After applying both proper motion and PWZ-based filtering, the remaining RR Lyrae stars align more clearly along the horizontal branch defined by the spectroscopically confirmed members in the CMD (Fig. 33).

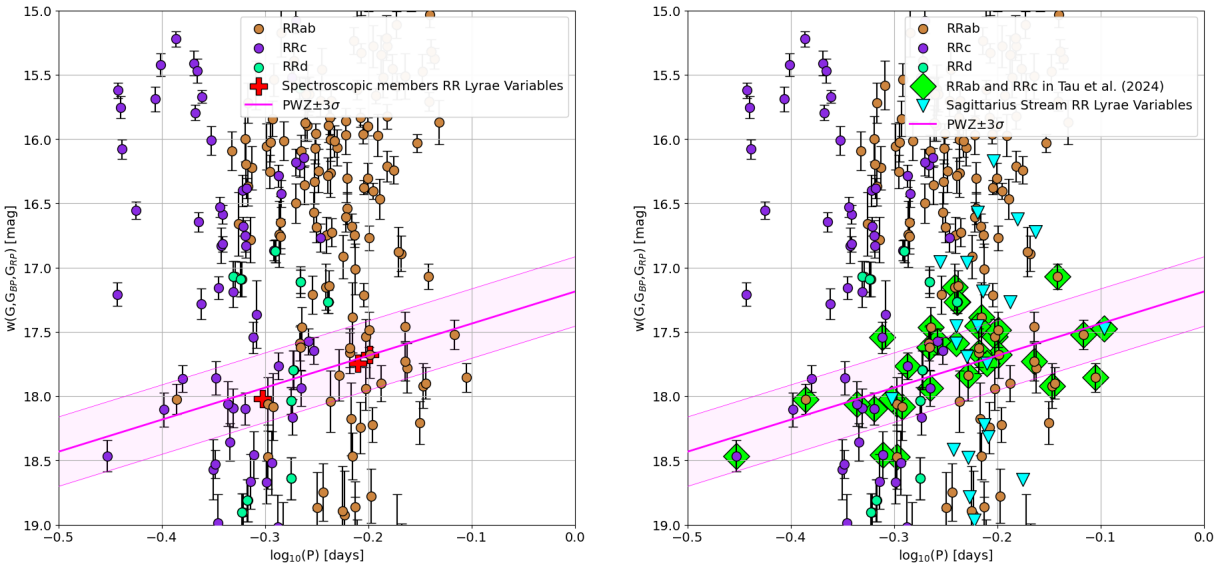

Figure 31: Left: Pw diagram of RR Lyrae stars in Boötes III. The magenta solid line with $\pm 3\sigma$ bands shows the PWZ relation for RR Lyrae stars by Garofalo et al. (2022) shifted according to the distance modulus of Boötes III. RRab-type stars in brown, RRc-type stars in purple, RRd-type stars in green. Red crosses: RR Lyrae spectroscopic members. **Right:** Same as in the left panel, with green diamonds representing the RR Lyrae stars classified as Boötes III members by Tau et al. (2024), and with cyan triangles the RR Lyrae variables belonging to the Sagittarius Stream.

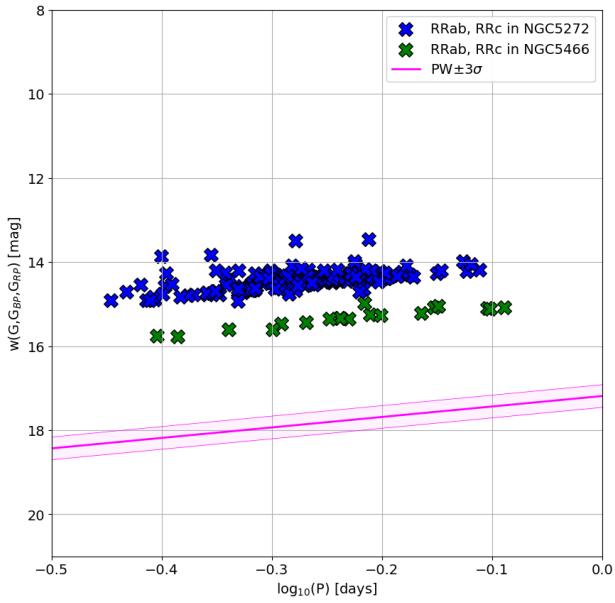

Figure 32: Pw diagram of RR Lyrae stars associated with NGC5272 (blue) and NGC5466 (green). The magenta solid line with $\pm 3\sigma$ bands shows the PWZ relation for RR Lyrae stars by Garofalo et al. (2022) shifted according to the distance modulus of Boötes III.

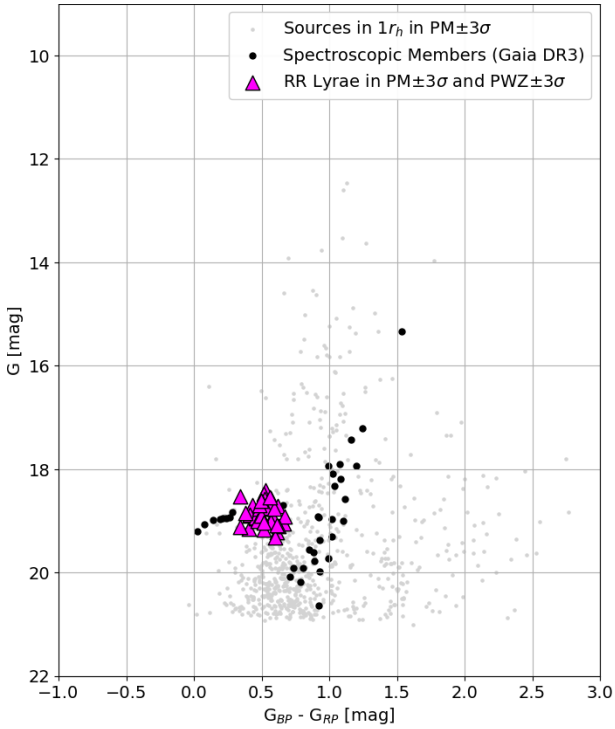

Figure 33: Color-magnitude diagram of Boötes III after applying proper motion and PWZ selections to RR Lyrae stars.

3.2.3 Reverse filtering via the PWZ relation

By repeating the analysis using only the PWZ relation, the result was the same selection of 38 RR Lyrae variables (Fig. 34). This outcome demonstrates the robustness and reliability of the PWZ-based selection.

For the sake of consistency with the previous discussion, the three Cepheids that passed the proper motion selection are not misclassified as Anomalous Cepheids belonging to Boötes III, as shown in left panel of Fig. 35. Also the Classical Cepheid likely associated with NGC5466 (*Gaia* DR3 1452625254531322752) - which pulsates in the first overtone - does not fall within the ACEP-1O relation. This further confirms that ultra-faint dwarf galaxies (UFDs), and Boötes III in particular, do not host young stellar populations or contain any detectable gas.

Additionally, the possibility that some RR Lyrae stars might actually be Anomalous Cepheids (ACEPs) was considered (rigth panel of Fig. 35). There are some RR Lyrae stars that meet the proper motion criteria but fall slightly outside the PWZ relation; these stars exhibit higher G-band magnitudes and lie within the Period-Wesenheit relation of Anomalous Cepheids, making them potential candidates for that classification (see left panel in Figure 36 and Table 8). Conversely, other stars that satisfy the PWZ relation are considered more likely to be genuine RR Lyrae members of Boötes III. It should also be noted that *Gaia* magnitudes may be subject to uncertainties, and thus these stars could indeed be bona fide RR Lyrae variables.

In conclusion, Boötes II appears to host 38 candidate RR Lyrae stars, along with 4 additional sources that may be Anomalous Cepheid candidates requiring further investigation. Two additional RR Lyrae stars, identified as spectroscopic members in Carlin et al. (2018) and as candidate members in Tau et al. (2024), are of particular interest. The final CMD and spatial distribution of RR Lyrae stars candidate members of Boötes III are shown in Fig. 36, their proper motions are shown in Fig. 37.

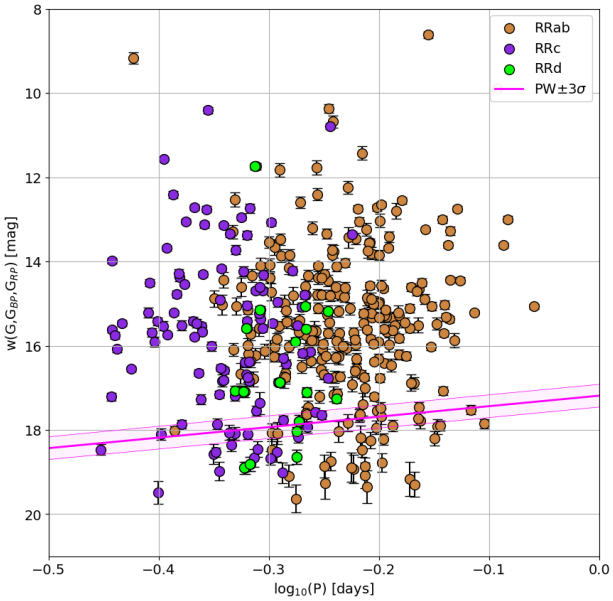

Figure 34: Pw diagram of RR Lyrae stars in Boötes III, without proper motion selection. The magenta solid line with $\pm 3\sigma$ bands shows the PWZ relation for RR Lyrae stars by Garofalo et al. (2022).

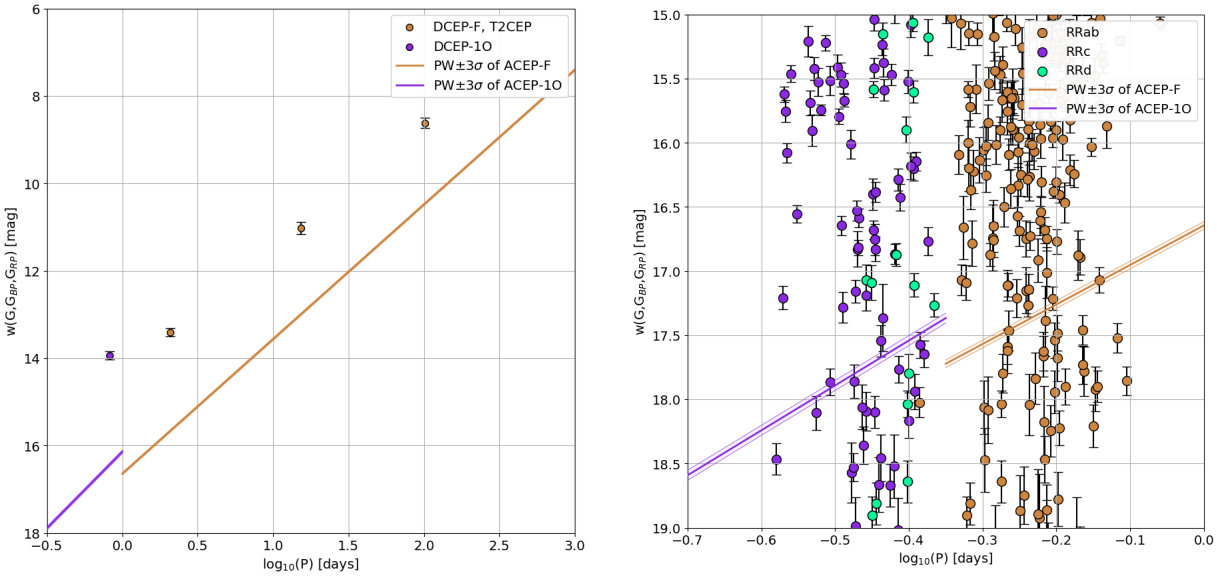

Figure 35: Pw diagram of Cepheid stars (**left panel**) and RR Lyrae stars (**right panel**) within 10° around the centre of Boötes III. The brown solid line with $\pm 3\sigma$ bands shows the PW relation for ACEP-F stars by Ripepi et al. (2023), and in purple it is shown that for ACEP-1O stars. All the relations are shifted according to the distance modulus of Boötes III.

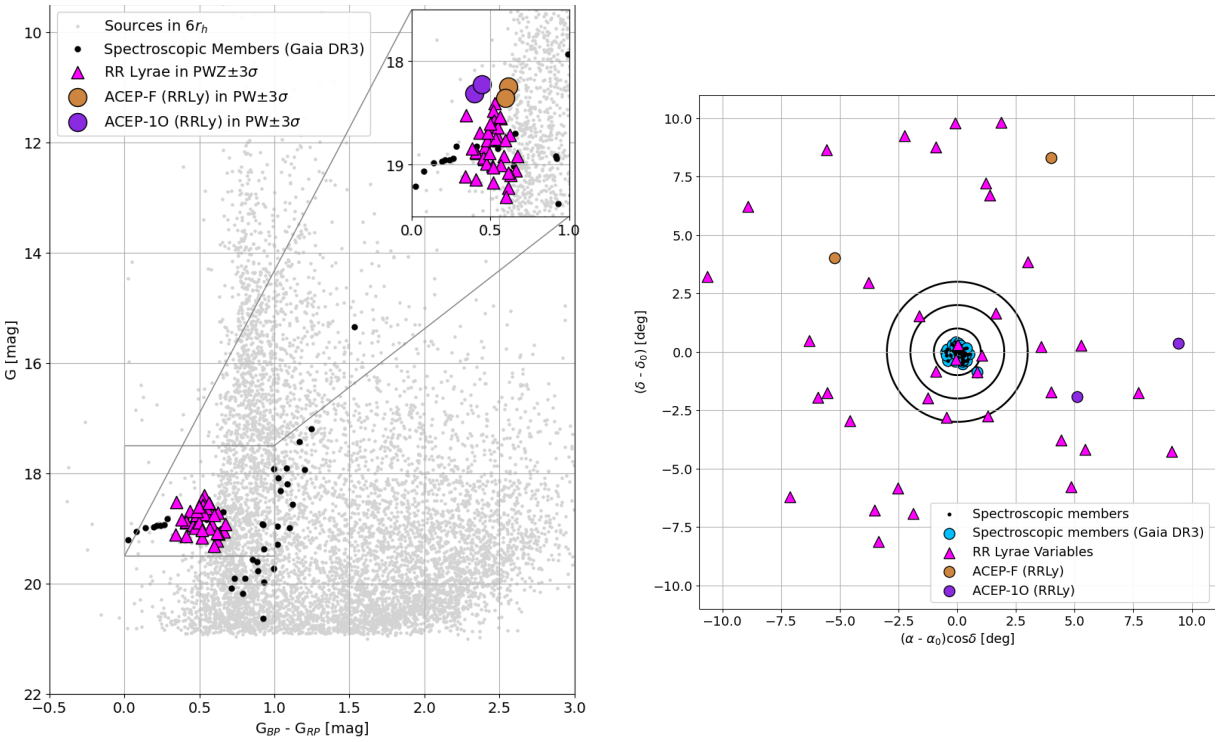

Figure 36: Left: Color-magnitude diagram of Boötes III after applying the PWZ selection to RR Lyrae stars. All RR Lyrae stars (magenta triangles) are located along the horizontal branch. The ACEP-F and ACEP-1O candidates are shown with brown and purple dots, respectively. **Right:** Spatial distribution of member stars identified through spectroscopy (black and light-blue dots) together with the RR Lyrae and ACEP candidate members of Boötes III (magenta triangles and brown/purple dots, respectively). Black circles: 1, 2, 3 r_h around the centre.

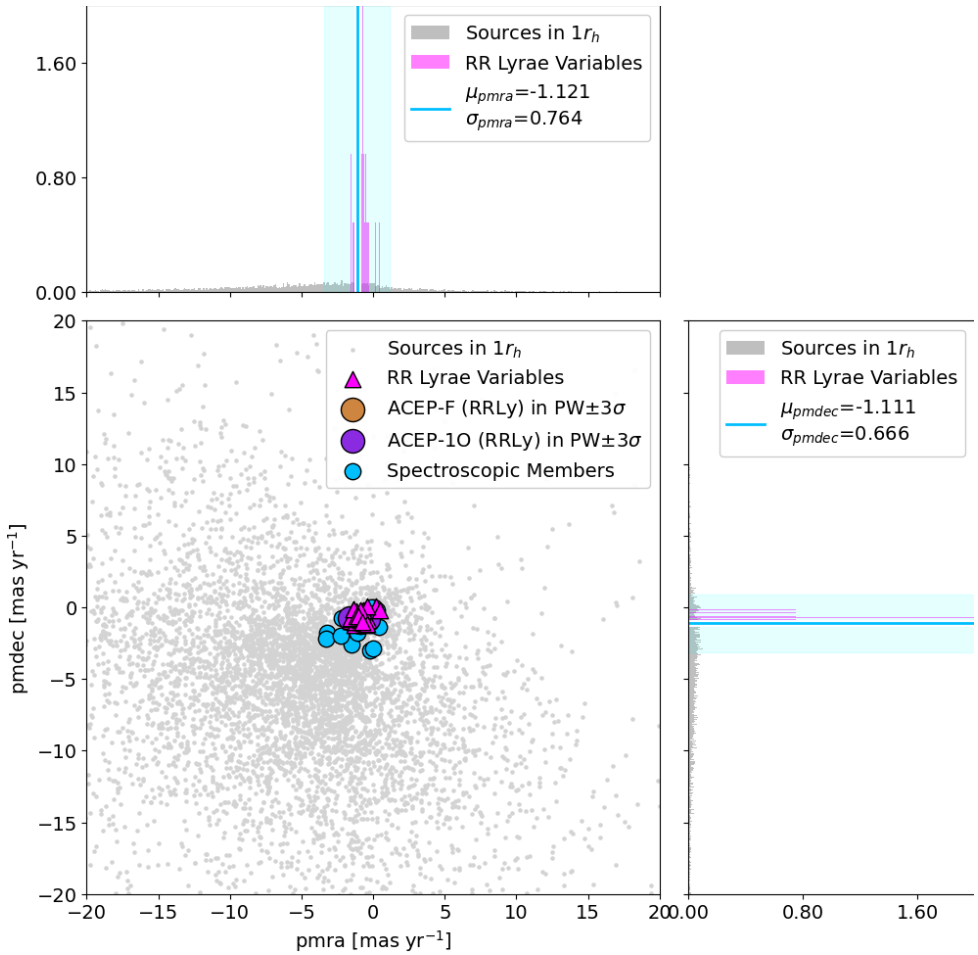

Figure 37: Proper motion distribution of RR Lyrae and ACEP candidate members of Boötes III (magenta triangles, and brown/purple dots).

Table 8: Properties of Boötes III RR Lyrae Variables identified through multi-method approach compared with literature.

Boötes III													
source_id	RA (deg)	Dec (deg)	pmra (mas/yr)	pmdec (mas/yr)	G (mag)	G_{BP} (mag)	G_{RP} (mag)	Class.	S.M.	Tau et al. (2024)	PM + PWZ	PWZ	ACEP
1258556500130302080	210.144	25.931	-1.235	-0.889	18.728	19.045	18.498	RRab	Y	Y	Y	Y	-
1450755118394910720	209.529	26.471	-1.301	-1.003	18.751	19.023	18.500	RRab	Y[3,4]	Y[3,4]	-[3,4]	-[3,4]	-
1450750170592551040	209.529	26.386	-1.260	-0.974	18.811	18.991	18.578	RRc	Y[3,4]	Y[3,4]	-[3,4]	-[3,4]	-
1242328223900152192	218.441	22.536	-0.597	-0.649	19.054	19.400	18.737	RRab	-	-	Y	Y	-
1247774689108256640	205.932	18.667	-1.102	-0.710	18.692	18.883	18.450	RRc	-	-	Y	Y	ACEP-1O[1]
1248333623267869184	207.427	19.872	-0.770	-0.277	19.145	19.297	18.888	RRc	-	-	Y	Y	-
1249231099634348544	205.783	20.013	-0.654	-1.158	18.892	19.021	18.608	RRc	-	Y	Y	Y	-
1250881947623682048	206.757	20.950	-0.845	-0.262	18.917	19.136	18.553	RRd	-	-	Y	Y	-
1252246609057063168	214.138	21.024	-0.798	-0.984	18.406	18.625	18.095	RRab	-	Y	Y	Y	ACEP-F[2]
1253064405189570816	214.746	22.613	-0.696	-0.629	19.115	19.209	18.870	RRc	-	Y	Y	Y	-
1253815887028053888	213.720	23.015	-1.365	-0.123	19.172	19.438	18.921	RRab	-	-	Y	Y	-
1255978763838231680	217.008	25.057	0.188	0.104	19.221	19.519	18.905	RRab	-	-	Y	Y	-
1257024914792212736	210.584	24.056	-1.306	-1.230	18.548	18.735	18.210	RRab	-	Y	Y	Y	-

[1] = RR Lyrae stars which fall in the PW relation for Anomalous Cepheids (ACEP-F and ACEP-1O), however they are candidates as RR Lyrae stars of Boötes III.
[2] = RR Lyrae star which can be Anomalous Cepheid (ACEP-F and ACEP-1O) candidates since they are more luminous with respect to the average (brighter then 18.5 mag).
[3] = RR Lyrae stars classified as members of Boötes III through spectroscopy (Carlin et al. (2018)) also attributed to Sagittarius Stream (Muraveva et al. (2025a)).
[4] = RR Lyrae stars from the Sagittarius Stream classified by Tau et al. (2024) as Boötes III members.
[5] = RR Lyrae star classified by Tau et al. (2024), but not obtained through the multi-method approach since it does not fall in the PWZ relation, found only if the distance modulus obtained from Vivas et al. (2020) or the *Gaia* DR3 photometry are not correct.

Tab. 8 continued.

Boötes III													
source_id	RA (deg)	Dec (deg)	pmra (mas/yr)	pmdec (mas/yr)	G (mag)	G_{BP} (mag)	G_{RP} (mag)	Class.	S.M.	Tau et al. (2024)	PM + PWZ	PWZ	ACEP
1257911670920015104	208.833	23.981	-0.928	-1.006	19.012	19.230	18.715	RRab	-	Y	Y	Y	-
1258709504045092608	210.344	26.650	-1.524	-0.967	18.830	19.028	18.564	RRc	-	Y	Y	Y	-
1258830965720483584	213.304	25.068	-1.187	-0.280	18.524	18.650	18.307	RRc	-	-	Y	Y	ACEP-1O[1]
1259629279881853568	214.578	27.065	-1.599	-0.960	18.479	18.665	18.147	RRab	-	Y	Y	Y	-
1260047442192835968	212.876	27.021	-1.270	-1.002	18.576	18.832	18.311	RRc	-	Y	Y	Y	ACEP-1O[1]
1441472182239737472	202.166	20.586	-0.523	-0.621	18.879	18.991	18.581	RRc	-	-	Y	Y	-
1443914957775067392	204.735	23.859	-0.787	-0.814	18.627	18.773	18.271	RRab	-	Y	Y	Y	-
1444925782622868992	203.354	24.845	-0.539	-1.223	19.008	19.276	18.710	RRab	-	Y	Y	Y	-
1444976909913197568	203.756	25.048	-0.707	-1.096	18.553	18.804	18.237	RRab	-	Y	Y	Y	ACEP-F[1]
1448835856425535232	202.990	27.264	0.468	-0.181	18.641	18.877	18.330	RRab	-	-	Y	Y	ACEP-F[1]
1450165337781635584	208.044	24.830	-0.672	-1.023	18.947	19.153	18.694	RRab	-	Y	Y	Y	-
1450391626723098496	208.385	25.950	-1.036	-0.687	18.933	19.132	18.677	RRc	-	Y	Y	Y	-
1450796178282259072	209.222	26.465	-0.906	-0.854	18.761	18.958	18.476	RRab	-	Y	Y	Y	-

[1] = RR Lyrae stars which fall in the PW relation for Anomalous Cepheids (ACEP-F and ACEP-1O), however they are candidates as RR Lyrae stars of Boötes III.
[2] = RR Lyrae star which can be Anomalous Cepheid (ACEP-F and ACEP-1O) candidates since they are more luminous with respect to the average (brighter then 18.5 mag).
[3] = RR Lyrae stars classified as members of Boötes III through spectroscopy (Carlin et al. (2018)) also attributed to Sagittarius Stream (Muraveva et al. (2025a)).
[4] = RR Lyrae stars from the Sagittarius Stream classified by Tau et al. (2024) as Boötes III members.
[5] = RR Lyrae star classified by Tau et al. (2024), but not obtained through the multi-method approach since it does not fall in the PWZ relation, found only if the distance modulus obtained from Vivas et al. (2020) or the *Gaia* DR3 photometry are not correct.

Tab. 8 continued.

Boötes III													
source_id	RA (deg)	Dec (deg)	pmra (mas/yr)	pmdec (mas/yr)	G (mag)	G_{BP} (mag)	G_{RP} (mag)	Class.	S.M.	Tau et al. (2024)	PM + PWZ	PWZ	ACEP
1451041850411971840	209.312	27.120	-1.539	-0.839	18.714	18.947	18.326	RRab	-	Y	Y	Y	-
1452142427191511808	207.669	28.341	-0.886	-0.769	18.750	18.923	18.392	RRab	-	Y	Y	Y	-
1452544990182058752	210.937	28.451	-0.340	-0.895	18.991	19.175	18.702	RRab	-	Y	Y	Y	-
1453431020459339008	212.308	30.651	-1.561	-0.725	18.764	19.041	18.446	RRab	-	Y	Y	Y	ACEP-F[1]
1455206869177310336	205.530	29.766	-0.728	-0.363	18.891	19.112	18.618	RRab	-	-	Y	Y	-
1462781512156370944	198.646	30.029	-0.706	-0.211	18.919	19.259	18.586	RRab	-	-	Y	Y	-
1469693415909950336	200.383	33.029	-0.400	0.078	19.103	19.296	18.669	RRab	-	-	Y	Y	-
1471422161722231424	207.060	36.052	-0.678	-0.735	18.841	18.971	18.589	RRc	-	-	Y	Y	ACEP-1O[1]
1471682642898913280	203.716	35.437	-1.401	-0.143	19.030	19.270	18.752	RRd	-	-	Y	Y	-
1481768768001796608	210.696	33.515	-0.903	-0.182	19.314	19.564	18.965	RRc	-	-	Y	Y	-
1482006163731184256	210.520	34.027	-1.182	-0.630	18.693	18.873	18.390	RRc	-	Y	Y	Y	-
1483168480663545984	208.382	35.557	-0.429	-1.156	18.603	18.828	18.331	RRc	-	-	Y	Y	-
1483331036585934976	209.199	36.582	-1.065	-0.619	18.540	18.738	18.175	RRab	-	-	Y	Y	-

[1] = RR Lyrae stars which fall in the PW relation for Anomalous Cepheids (ACEP-F and ACEP-1O), however they are candidates as RR Lyrae stars of Boötes III.
[2] = RR Lyrae star which can be Anomalous Cepheid (ACEP-F and ACEP-1O) candidates since they are more luminous with respect to the average (brighter then 18.5 mag).
[3] = RR Lyrae stars classified as members of Boötes III through spectroscopy (Carlin et al. (2018)) also attributed to Sagittarius Stream (Muraveva et al. (2025a)).
[4] = RR Lyrae stars from the Sagittarius Stream classified by Tau et al. (2024) as Boötes III members.
[5] = RR Lyrae star classified by Tau et al. (2024), but not obtained through the multi-method approach since it does not fall in the PWZ relation, found only if the distance modulus obtained from Vivas et al. (2020) or the *Gaia* DR3 photometry are not correct.

Tab. 8 continued.

Boötes III													
source_id	RA (deg)	Dec (deg)	pmra (mas/yr)	pmdec (mas/yr)	G (mag)	G_{BP} (mag)	G_{RP} (mag)	Class.	S.M.	Tau et al. (2024)	PM + PWZ	PWZ	ACEP
1483440442289558016	211.174	36.621	-0.737	-1.000	19.082	19.359	18.744	RRab	-	-	Y	Y	-
1255773498761714560	214.395	24.878	-0.336	-0.824	18.311	18.439	18.040	RRc	-	Y[5]	-	-	ACEP-1O[2]
1280319511739472256	218.725	27.160	-1.615	-0.742	18.222	18.510	18.064	RRc	-	-	-	-	ACEP-1O[2]
1456272197161366144	204.056	30.834	-0.879	-0.996	18.246	18.458	17.846	RRab	-	Y[5]	-	-	ACEP-F[2]
1250883833113992448	206.919	20.952	-1.627	-0.671	18.725	18.901	18.309	RRab	-	Y[4]	-	-	-
1443201542231710592	201.649	23.192	-1.107	-0.979	18.609	18.863	18.263	RRab	-	Y[4]	-	-	-
1447594232919176192	200.416	26.113	-0.553	-0.396	19.278	19.458	19.039	RRab	-	Y[5]	-	-	-
1449382103249666432	200.587	27.449	-1.622	-0.612	19.299	19.540	19.102	RRc	-	Y[5]	-	-	-
1450735121027824000	209.808	26.340	-1.288	-0.778	18.704	18.923	18.283	RRab	-	Y[4]	-	-	-
1456624758140656512	206.062	31.787	-0.203	-0.554	19.195	19.488	18.791	RRab	-	Y[5]	-	-	-
1258096354513939328	209.876	25.269	-0.947	-0.901	18.291	18.514	17.980	RRd	-	Y[5]	-	-	-
1254331626700904064	216.213	22.666	-0.457	-1.599	18.341	18.640	18.021	RRab	-	Y[5]	-	-	-
1479393273129815808	213.284	35.107	-0.894	-1.037	18.358	18.590	17.995	RRab	-	-	-	-	ACEP-F[2]

[1] = RR Lyrae stars which fall in the PW relation for Anomalous Cepheids (ACEP-F and ACEP-1O), however they are candidates as RR Lyrae stars of Boötes III.
[2] = RR Lyrae star which can be Anomalous Cepheid (ACEP-F and ACEP-1O) candidates since they are more luminous with respect to the average (brighter then 18.5 mag).
[3] = RR Lyrae stars classified as members of Boötes III through spectroscopy (Carlin et al. (2018)) also attributed to Sagittarius Stream (Muraveva et al. (2025a)).
[4] = RR Lyrae stars from the Sagittarius Stream classified by Tau et al. (2024) as Boötes III members.
[5] = RR Lyrae star classified by Tau et al. (2024), but not obtained through the multi-method approach since it does not fall in the PWZ relation, found only if the distance modulus obtained from Vivas et al. (2020) or the *Gaia* DR3 photometry are not correct.

3.3 Carina II

Carina II is an ultra-faint dwarf galaxy discovered as part of the Magellanic Satellites Survey (MagLiteS), in close proximity to the Large Magellanic Cloud (LMC) (Torrealba et al. 2018). Located at heliocentric distance of approximately 36 kpc and separated by only 18 arcminutes from the fainter and more compact Carina III, Carina II and III form an intriguing pair. Together with other systems discovered using the Dark Energy Camera, these satellites form a highly anisotropic cloud of galaxies in the vicinity of the Magellanic Clouds. Carina II is characterised by an old and metal-poor stellar population, an absolute magnitude of $M_V \sim -4.5$ mag and a half-light radius of ∼90 pc. The small number of RR Lyrae stars detected, three consistent with Carina II distance, is itself a feature supporting the classification of such low-mass system as a UFD galaxy.

High-resolution spectroscopic follow-up by Ji et al. (2020) provided detailed chemical abundances for nine stars in Carina II, including the first abundance measurement of an RR Lyrae star in a UFD.

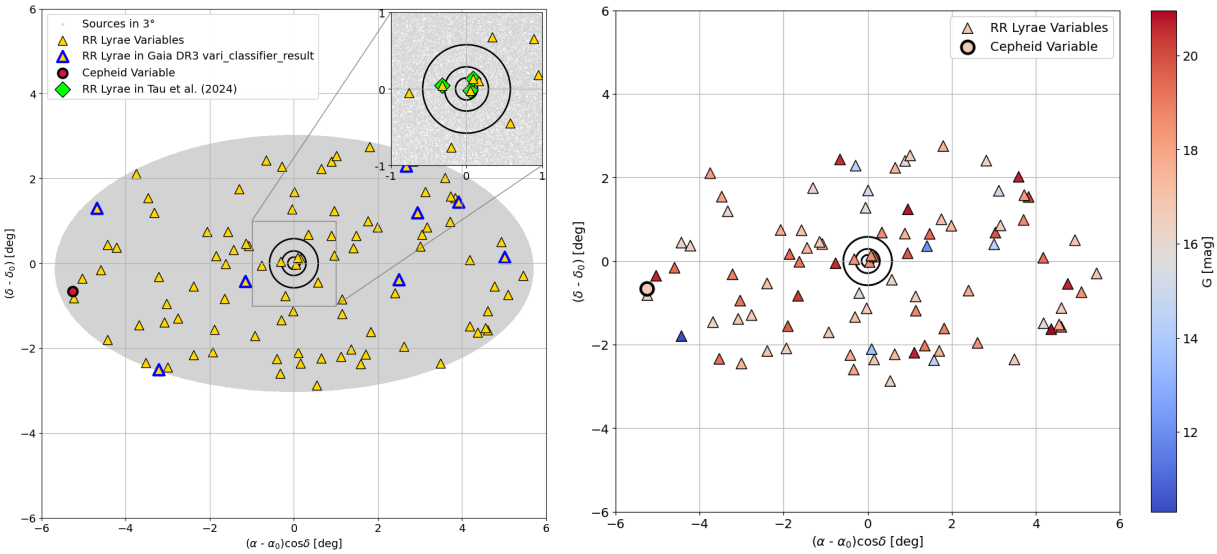

Figure 38: Left: Spatial distribution of sources (grey dots) and RR Lyrae variables (yellow triangles), RR Lyrae candidates in the *Gaia* `gaiadr3.vari_classifier_result` catalogue (yellow triangles with blue edges) and Classical Cepheid variable (DCEP-1O, red dot) within 3° around the centre of Carina II. Green diamonds: RR Lyrae stars identified by Tau et al. (2024). Black circles: 1, 2, 4 r_h around the centre. **Right:** G-band color-map of RR Lyrae and Cepheid stars within 3° around the centre of Carina II.

3.3.1 Spatial distribution and mapping of stellar population

Ninety RR Lyrae variables are found within a 3° radius from the centre of Carina II (Fig. 38). Among them, eight were labeled as RR Lyrae by the *Gaia* `gaiadr3.vari_classifier_result` catalogue. One Classical Cepheid (DCEP-1O, *Gaia* DR3 5485733892053016192) is present in this region, but its large angular distance from the center may already suggest that it is unlikely to be associate with Carina II.

The Sagittarius Stream does not cross this region of the sky. Eight of the nine stars confirmed by Ji et al. (2020) to be members of Carina II based on spectroscopic analysis are listed in *Gaia* DR3, including an RR Lyrae star (*Gaia* DR3 5293940924860019584, Fig. 39). This variable, along with two others, is classified by Tau et al. (2024) as a member of Carina II.

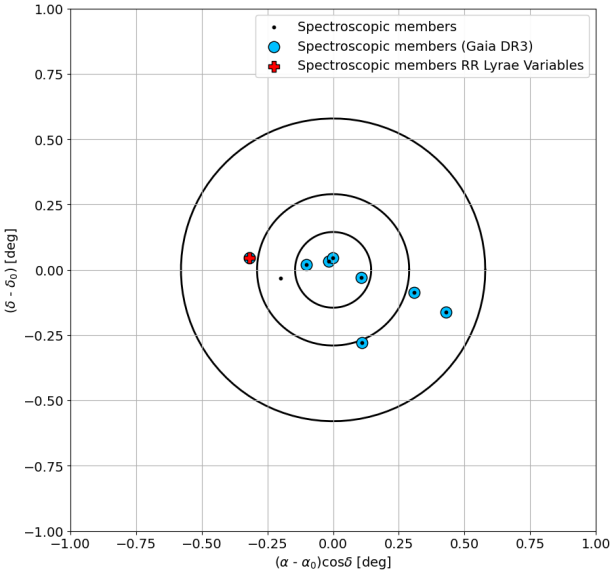

Figure 39: Spatial distribution of member stars identified through spectroscopy. Black dots: members identified by Ji et al. (2020). Light-blue dots: members also catalogued in *Gaia* DR3. Red cross: RR Lyrae spectroscopic member. Black circles: 1, 2, 4 r_h around the centre.

3.3.2 Proper Motion and Period-Wesenheit-Metallicity Relation selections

An initial filtering was performed to exclude variable stars with uncertainties on proper motions greater than 0.5 mas yr^{-1}, which resulted in the removal of 10 sources (Fig. 40)

The average values of the proper motions are reported in Tab. 3. As shown in Fig. 41, is evident that the proper motion distribution of sources within $4r_h$ significantly deviates from the average motion of the spectroscopically confirmed members. This discrepancy is likely due to the compact nature of Carina II and the substantial contamination from foreground and background field stars in its surrounding region.

Following the proper motion-based filtering, only a small number of sources remain, resulting in a sparsely populated color-magnitude diagram (left panel of Fig. 42). Nevertheless, a general stellar population profile is still discernible: the spectroscopically confirmed members appear to trace a red giant branch, and few sources hint at the presence of a horizontal branch. The three RR Lyrae variables fall along this HB, consistent with expectations for old, metal-poor populations.

A 3σ selection in the Pw plane was then applied. After the combined selection - in terms of proper motion space and PWZ relation - only the three RR Lyrae variables identified by Tau et al. (2024) remained (Fig. 42).

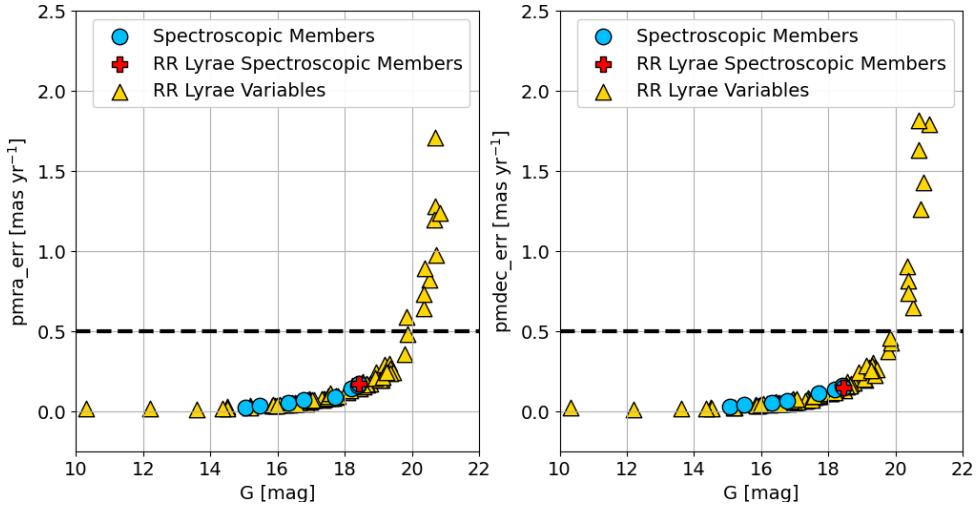

Figure 40: Proper motion errors of RR Lyrae stars (yellow triangles) and spectroscopic members (light-blue dots) within 10° around the centre of Boötes III as a function of G-band magnitude. The RR Lyrae spectroscopic member (red cross) is located below the 0.5 mas yr^{-1} (dashed) line.

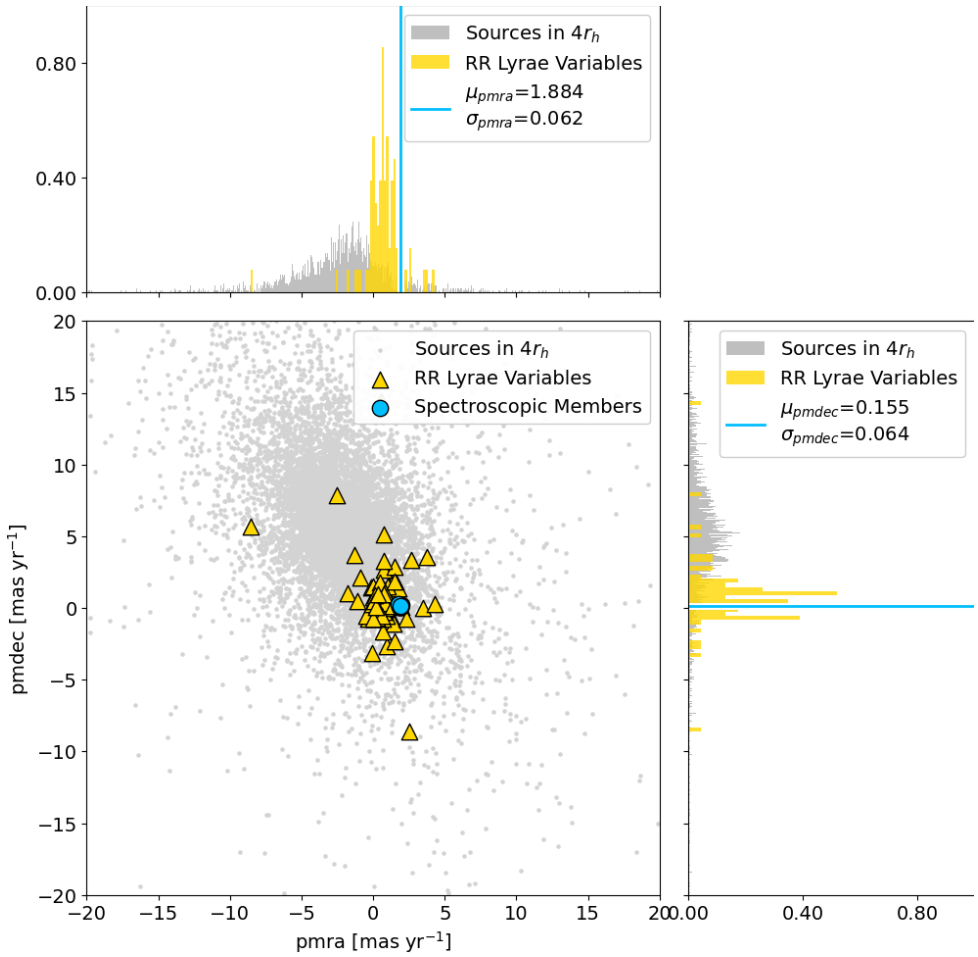

Figure 41: Proper motion distribution of sources within $4r_h$ (grey dots) and RR Lyrae stars in 3° (yellow triangles) around the centre of Carina II. The cyan shaded bands representing the $\pm 3\sigma$ dispersion of the mean proper motions (cyan lines) - computed using the spectroscopic members (light-blue dots) - are not clearly visible due to the very small value of σ (see Tab. 3).

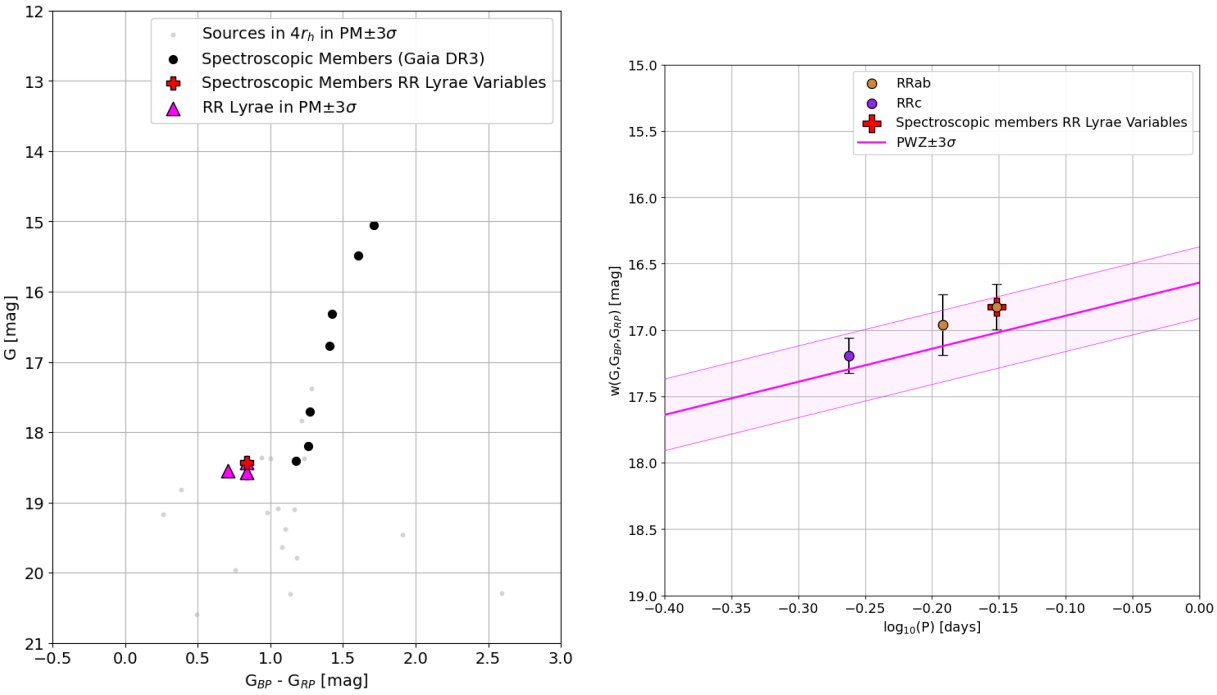

Figure 42: Left: Color-magnitude diagram of Carina II after proper motion selection. The CMD remains the same after applying the PWZ relation selection. The spectroscopic members (black dots) show a poor red giant branch profile of the stellar population. All the RR Lyrae stars (magenta triangles) are located along the horizontal branch defined by very few sources within $4r_h$. **Right:** Pw diagram of RR Lyrae stars in Carina II. The magenta solid line with $\pm 3\sigma$ bands shows the PWZ relation for RR Lyrae stars by Garofalo et al. (2022) shifted according to the distance modulus of Carina II. RRab-type star in brown, RRc-type star in purple. Red cross: RR Lyrae spectroscopic member (ab-type).

3.3.3 Reverse filtering via the PWZ relation

When applying the PWZ relation without enforcing a proper motion cut, a total of 18 variable stars fall within the expected relation boundaries (Fig. 43).

In this context, the possibility that some RR Lyrae candidates might instead be Anomalous Cepheids was also explored (left panel of Fig. 44). One object, in particular, appears to be a potential ACEP-F type candidate, even if it falls within the PWZ relation selection: *Gaia* DR3 5487437168707710976 (see left panel of Fig. 45). Other two, *Gaia* DR3 5295969347717500032 and *Gaia* DR3 5487172121982114432, could be ACEP-F candidates since they are brighter with respect to the other RR Lyrae stars which better fit the horizontal branch. However, as discussed in Chapter 3.2.3 for Boötes III, at such faint G-band magnitudes it is likely that uncertainties affect the positions of RR Lyrae stars in the color-magnitude diagram, potentially leading to incorrect placements.
Therefore, stars that fall within the Period-Wesenheit relation of Anomalous Cepheids but also within the PWZ relation of RR Lyrae stars are here classified as candidate RR Lyrae members of Carina II. Those that do not satisfy the PWZ relation may be candidate Anomalous Cepheids, but further investigation using *Gaia* DR4 data will be necessary.

As previously mentioned, the mean proper motions of the spectroscopically confirmed members differ significantly from those of the surrounding field stars within $4r_h$, indicating strong contamination. Thus, some sources (see [6] and [7] notes in Tab. 9) are extremely faint (G $>$ 19.5 mag) or exhibit pmra values as low as -3 mas yr^{-1} (Fig. 46).

Then, a separate test was conducted on the Classical Cepheid located within 3° of Carina II to assess the possibility of misclassification as an Anomalous Cepheid candidate for Carina II; however, the result was negative, confirming its classification (right panel of Fig. 44).

In conclusion, 5 RR Lyrae stars can be considered likely candidates for membership in Carina II: three of them satisfy both the proper motion and PWZ relation selections and are identified as candidates by Tau et al. (2024), and two additional stars pass only the PWZ relation selection, but their proper motions would be consistent with the mean values if better statistics on spectroscopic members were available. Four RR Lyrae stars are fainter than the others, despite falling within the PWZ relation. Three additional sources may be candidates for Anomalous Cepheids (ACEP-F) and require further investigation, particularly concerning potential variations in their astrometric and photometric parameters. The final spatial distribution is shown in right panel of Fig. 45 and the complete summary of all the considered RR Lyrae stars is in Tab. 9.

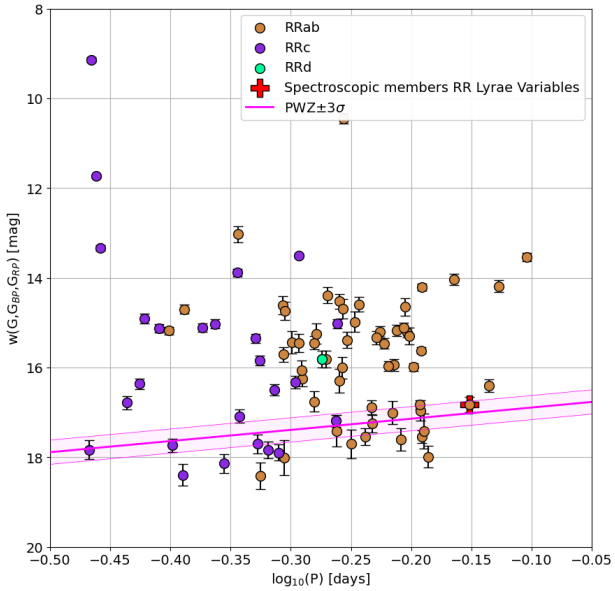

Figure 43: Pw diagram of RR Lyrae stars in Carina II. The magenta solid line with $\pm 3\sigma$ bands shows the PWZ relation for RR Lyrae stars by Garofalo et al. (2022) shifted according to the distance modulus of Carina II. RRab-type stars in brown, RRc-type stars in purple, RRd-type star in green. Red crosses: RR Lyrae spectroscopic member.

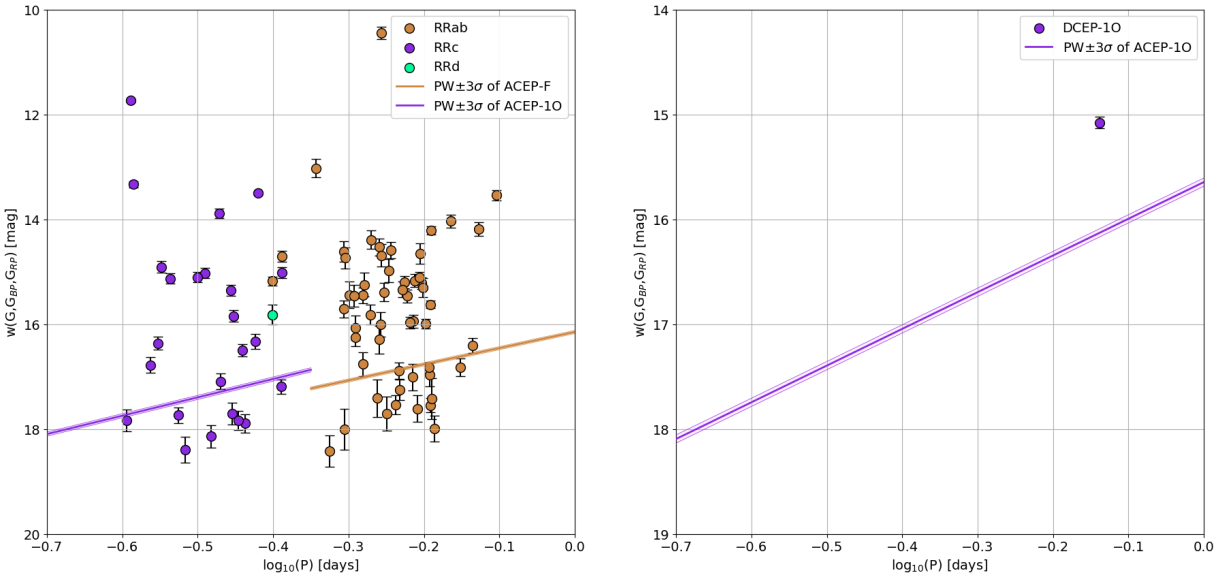

Figure 44: Pw diagram of RR Lyrae stars (**left panel**) and a Cepheid star (**right panel**) within 3° around the centre of Carina II. The brown solid line with $\pm 3\sigma$ bands shows the PW relation for ACEP-F stars by Ripepi et al. (2023), and in purple it is shown that for ACEP-1O stars. All the relations are shifted according to the distance modulus of Carina II.

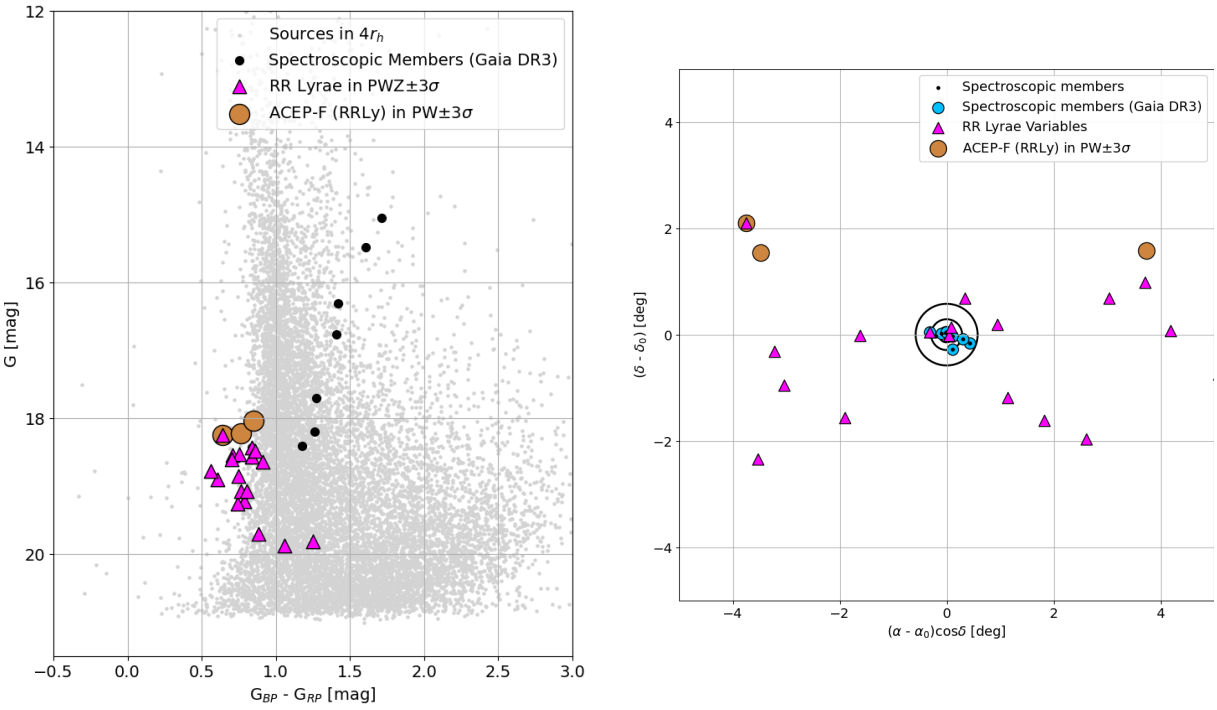

Figure 45: Left: Color-magnitude diagram of Carina II after applying the PWZ selection to RR Lyrae stars. A few RR Lyrae stars (magenta triangles) are located along the horizontal branch of Carina II. The ACEP-F candidates are shown with brown dots. **Right:** Spatial distribution of member stars identified through spectroscopy (black and light-blue dots) together with the RR Lyrae and ACEP-F candidates of Carina II (magenta triangles and brown dots, respectively). Black circles: 1, 2, 4 r_h around the centre.

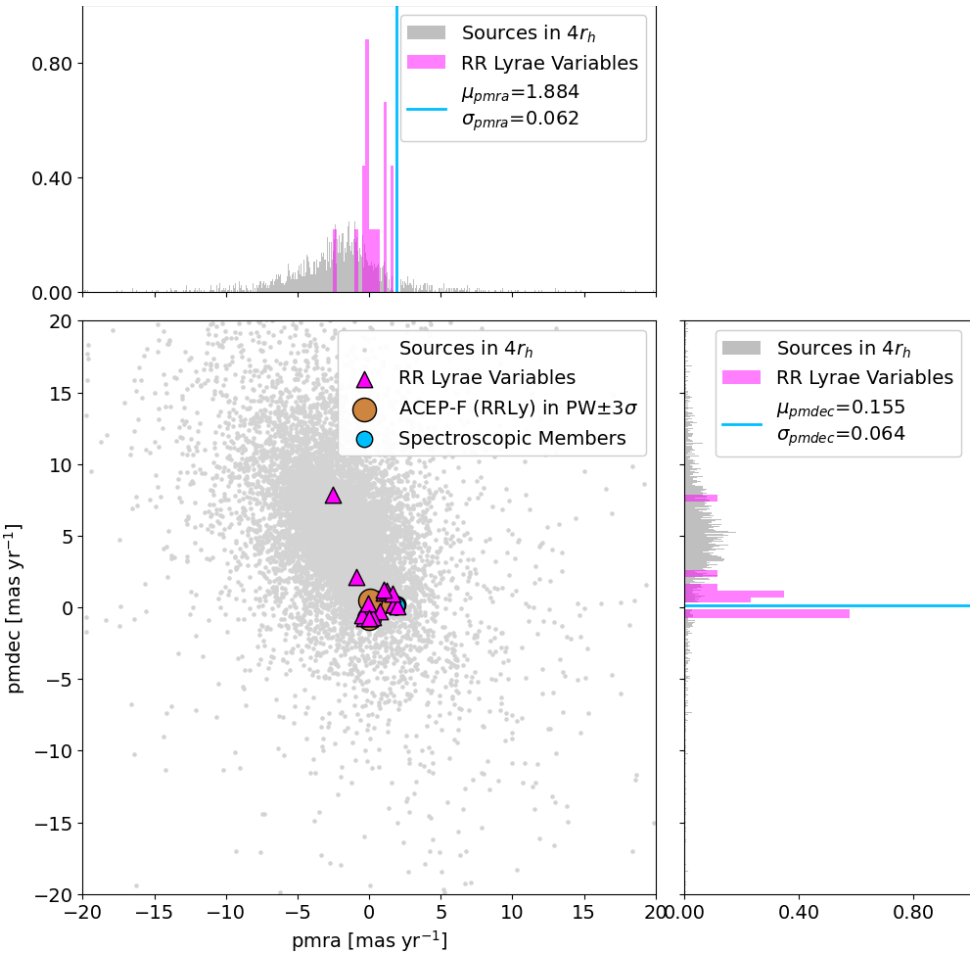

Figure 46: Proper motion distribution of RR Lyrae and ACEP-F candidate members of Carina II (magenta triangles).

Table 9: Properties of Carina II RR Lyrae Variables identified through multi-method approach compared with literature.

Carina II													
source_id	RA (deg)	Dec (deg)	pmra (mas/yr)	pmdec (mas/yr)	G (mag)	G_{BP} (mag)	G_{RP} (mag)	Class.	S.M.	Tau(2024)	PM + PWZ	PWZ	ACEP
5293940924860019584	113.788	-57.954	1.909	0.170	18.429	18.779	17.944	RRab	Y	Y	Y	Y	-
5293948136108013696	114.154	-58.021	1.716	0.236	18.571	18.931	18.092	RRab	-	Y	Y	Y	ACEP-F[1]
5293954286501519616	114.191	-57.865	1.999	0.105	18.548	18.797	18.091	RRc	-	Y	Y	Y	-
5292765130315857536	115.929	-59.613	-0.091	0.178	18.898	19.195	18.590	RRc	-	-	-	Y[6]	-
5292845811275694720	115.254	-59.186	0.048	-0.744	18.783	19.029	18.468	RRc	-	-	-	Y[6]	-
5293092028866831872	110.576	-60.340	1.036	1.058	19.221	19.530	18.741	RRab	-	-	-	Y[4]	-
5293702223460092928	112.208	-59.555	1.208	1.147	19.701	20.163	19.282	RRab	-	-	-	Y[5]	-
5294053379987211392	116.724	-59.958	-0.346	-0.750	18.480	18.826	17.965	RRab	-	-	-	Y	ACEP-F[1]
5294230676236196608	119.197	-58.742	-0.108	-0.042	18.531	18.846	18.096	RRc	-	-	-	Y[6]	-
5294515346670136576	118.287	-57.921	-0.461	-0.571	19.260	19.594	18.855	RRc	-	-	-	Y[4,6]	-

[1] = RR Lyrae stars which fall into the Period-Wesenhiet relation of Anomalous Cepheids (ACEP-F), however they are likely RR Lyrae stars.
[2] = RR Lyrae star which fall into the Period-Wesenhiet relation of ACEP-1O stars, however it is too faint to be classified as Anomalous Cepheid of Carina II, maybe it belongs to another system.
[3] = RR Lyrae stars which could be classified as Anomalous Cepheids (ACEP-F) because are brighter than the others.
[4] = RR Lyrae stars with *G*-band magnitude between 19 mag and 19.5 mag.
[5] = RR Lyrae stars identified through Period-Wesenhiet-Metallicity relation only, however excluded since they are fainter (G > 19.5 mag) with respect to the others which better fit the horizontal branch, maybe they belong to other systems.
[6] = RR Lyrae stars with pmra < -0.7 mas yr^{-1}.

Tab. 9 continued.

Carina II													
source_id	RA (deg)	Dec (deg)	pmra (mas/yr)	pmdec (mas/yr)	G (mag)	G_{BP} (mag)	G_{RP} (mag)	Class.	S.M.	Tau(2024)	PM + PWZ	PWZ	ACEP
5295345271794444032	117.148	-57.319	-0.898	2.149	19.869	19.869	18.810	RRc	-	-	-	Y[5,6]	ACEP-1O[2]
5295368189734737152	117.819	-57.015	0.723	-0.265	18.645	19.012	18.101	RRab	-	-	-	Y	ACEP-F[1]
5295408394924225792	115.058	-57.811	-2.528	7.889	19.816	19.709	18.462	RRab	-	-	-	Y[5,6]	-
5485574011894723456	111.072	-58.946	1.640	0.994	19.078	19.361	18.596	RRab	-	-	-	Y[4]	-
5485660843248015360	110.891	-58.317	0.242	-0.645	18.847	18.972	18.224	RRab	-	-	-	Y[6]	-
5486013472946989056	112.481	-58.017	1.041	1.254	19.078	19.459	18.658	RRab	-	-	-	Y[4]	-
5486139298310439680	114.446	-57.316	-0.058	0.256	18.602	18.831	18.128	RRab	-	-	-	Y[6]	-
5487437168707710976	110.359	-55.895	-0.037	-0.725	18.242	18.397	17.754	RRab	-	-	-	Y[3,6]	ACEP-F[3]
5295969347717500032	117.836	-56.421	0.821	0.328	18.227	18.500	17.738	RRab	-	-	-	-	ACEP-F[3]
5487172121982114432	110.634	-56.458	0.037	0.493	18.032	18.404	17.558	RRab	-	-	-	-	ACEP-F[3]

[1] = RR Lyrae stars which fall into the Period-Wesenhiet relation of Anomalous Cepheids (ACEP-F), however they are likely RR Lyrae stars.
[2] = RR Lyrae star which fall into the Period-Wesenhiet relation of ACEP-1O stars, however it is too faint to be classified as Anomalous Cepheid of Carina II, maybe it belongs to another system.
[3] = RR Lyrae stars which could be classified as Anomalous Cepheids (ACEP-F) because are brighter than the others.
[4] = RR Lyrae stars with G-band magnitude between 19 mag and 19.5 mag.
[5] = RR Lyrae stars identified through Period-Wesenhiet-Metallicity relation only, however excluded since they are fainter (G > 19.5 mag) with respect to the others which better fit the horizontal branch, maybe they belong to other systems.
[6] = RR Lyrae stars with pmra < -0.7 mas yr^{-1}.

3.4 Coma Berenices

Coma Berenices, first discovered by Belokurov et al. (2007), is located at a heliocentric distance of approximately 44 kpc. It is characterised by very low luminosity ($M_V \sim -4.1$ mag) and an extremely metal-poor stellar population, with an average metallicity of [Fe/H] ~ -2.3 dex (Simon 2019). Despite its small size and low stellar mass, Coma Berenices exhibits a significant velocity dispersion ($4.6^{+0.8}_{-0.8}$ km s$^-$1; McConnachie 2012; Muñoz et al. 2018, and references therein), which implies a high dark matter content and supports its classification as a dark matter-dominated system (Muñoz et al. 2018; Simon 2019, and references therein).
Several spectroscopic studies have investigated its chemical properties and internal kinematics (Simon 2019). The galaxy shows signs of a narrow metallicity spread, indicating a brief and early episode of star formation, consistent with expectations for ultra-faint dwarf galaxies. Its relative proximity and isolated environment make Coma Berenices a particularly suitable laboratory for probing the properties of ancient stellar populations in low-mass dark matter halos. Three RR Lyrae stars have been identified in this system (Musella et al. 2009; Vivas et al. 2020), providing valuable distance estimates and further constraints on its stellar content.

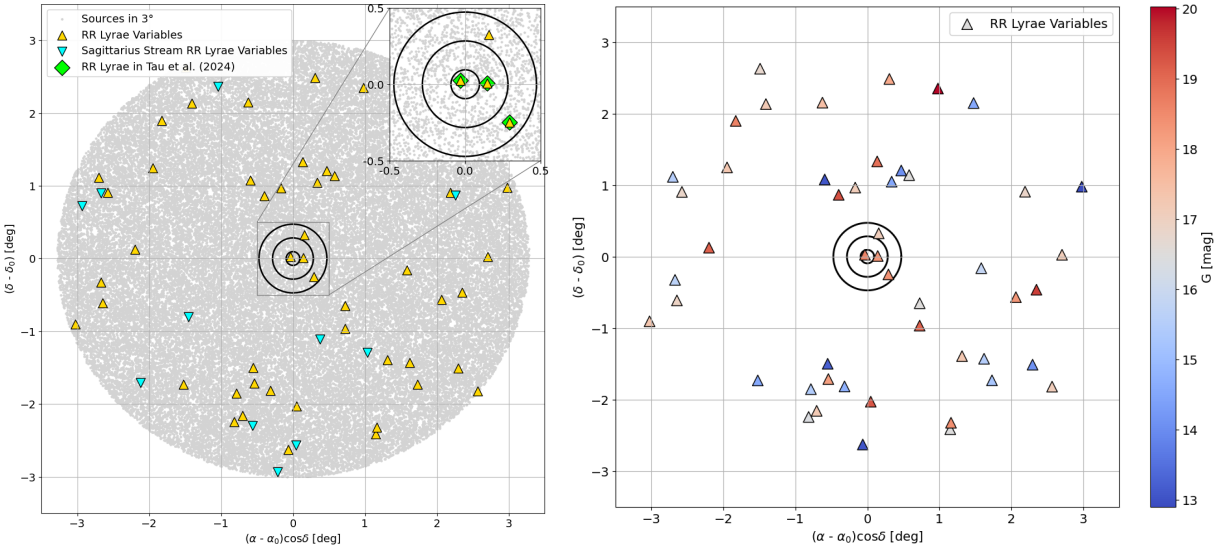

Figure 47: Left: Spatial distribution of sources (grey dots) and RR Lyrae variables (yellow triangles) within 3° around the centre of Coma Berenices. Cyan triangles: Sagittarius Stream RR Lyrae stars. Green diamonds: RR Lyrae stars identified by Tau et al. (2024). Black circles: 1, 3, 5 r_h around the centre. **Right:** G-band color-map of RR Lyrae stars within 3° around the centre of Coma Berenices.

3.4.1 Spatial distribution and mapping of stellar population

Sixty-one RR Lyrae variables are within 3° around the centre of Coma Berenices (see Fig. 47). No Cepheid variables are present in this region. The Sagittarius Stream passes through this area and contributes with 12 RR Lyrae stars: these were excluded, reducing the sample to 49 variables.

According to Tau et al. (2024), 3 RR Lyrae stars are associated with Coma Berenices. In Waller et al. (2023), 43 stars were spectroscopically identified as members of Coma Berenices. Of them, 6 are also present in the *Gaia* DR3 catalogue, including one RR Lyrae variable also mentioned in Tau et al. (2024).

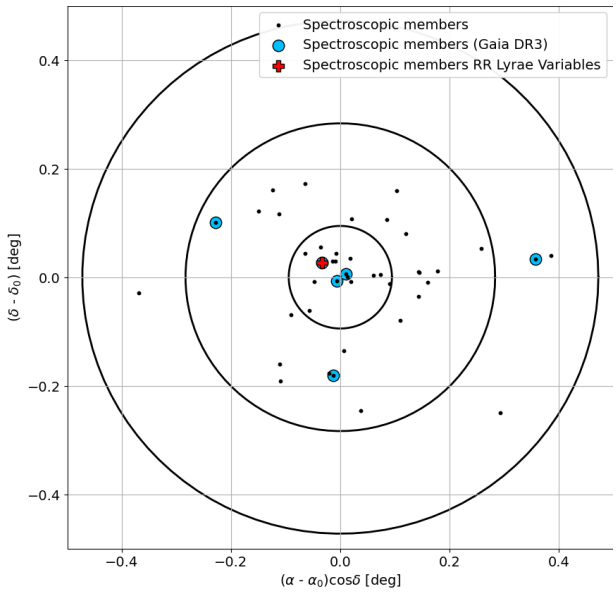

Figure 48: Spatial distribution of member stars identified through spectroscopy. Black dots: members identified by Waller et al. (2023). Light-blue dots: members also catalogued in *Gaia* DR3. Black circles: 1, 3, 5 r_h around the centre.

3.4.2 Proper Motion and Period-Wesenheit-Metallicity Relation selections

The preliminary cut based on proper motion errors further reduced the number to 48 (Fig. 49).

The average values of the proper motions are reported in Tab. 3. A 3σ selection around the mean values was applied, reducing the number of RR Lyrae stars to 11.
Several RR Lyrae stars lie along the horizontal branch region defined by the spectroscopic members (left panel of Fig. 51). However, a significant scatter in G mean magnitude is present.
Despite the relatively wide search radius ($5r_h$) around the centre of Coma Berenices, the selected sources appear sparsely distributed in the CMD and do not strongly reinforce the stellar population profile traced by the spectroscopic sample.

After applying the PWZ selection, 6 RR Lyrae stars remain: 4 RRab and 2 RRc types (Fig. 52). Some stars from the Sagittarius Stream fall within the PWZ relation (cyan triangles in the right panel of Fig. 52). However, almost all of them have [Fe/H] > -2.0 dex, making it unlikely that they belong to Coma Berenices for which [Fe/H] = -2.25 dex. On the other hand, two stars have [Fe/H] < -2.0 dex and could therefore be associated with Coma Berenices: *Gaia* DR3 4002439414227271936 and *Gaia* DR3 3952751964076400384 (cyan stars in the right panel of Fig. 52). The RR Lyrae spectroscopic member lies very nicely on the PWZ relation, as shown in left panel of Fig. 52.

In the CMD, after applying both proper motion and PWZ selections, the remaining RR Lyrae stars align well along the horizontal branch (right panel of Fig. 51).

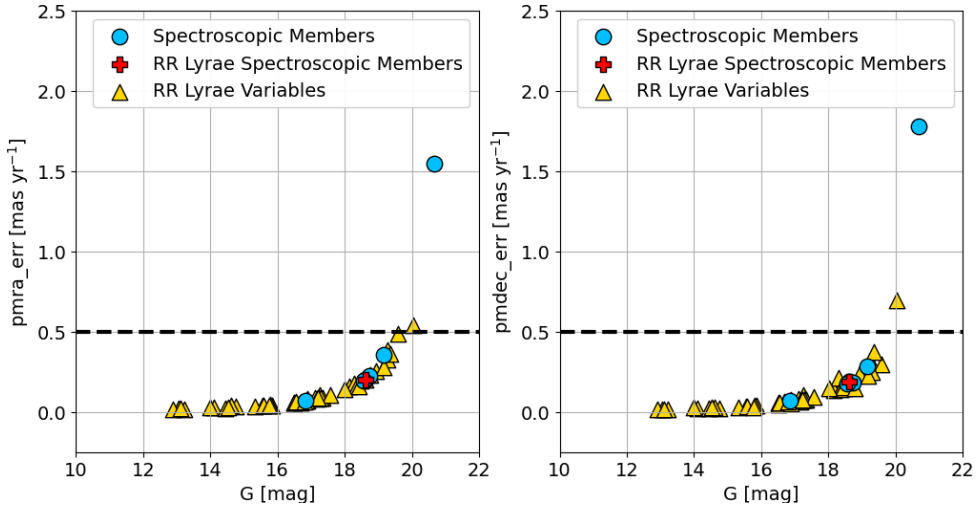

Figure 49: Proper motion errors of RR Lyrae stars (yellow triangles) and spectroscopic members (light-blue dots) within 3° around the centre of Coma Berenices as a function of G-band magnitude. The RR Lyrae spectroscopic member (red cross) is located below the 0.5 mas yr^{-1} (dashed) line.

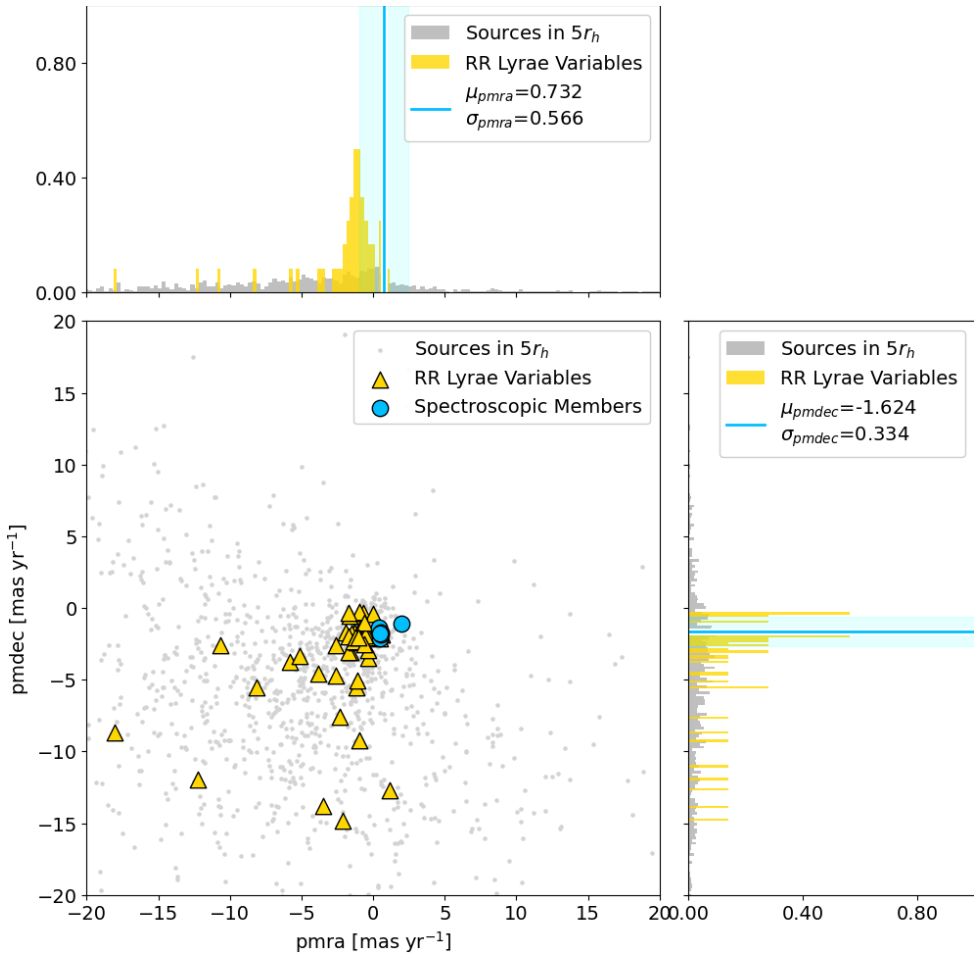

Figure 50: Proper motion distribution of sources in $5r_h$ (grey dots) and RR Lyrae stars in 3° (yellow triangles) around the centre of Coma Berenices. The cyan shaded bands represent $\pm 3\sigma$ of the mean proper motions (cyan lines) computed using the spectroscopic members (light-blue dots).

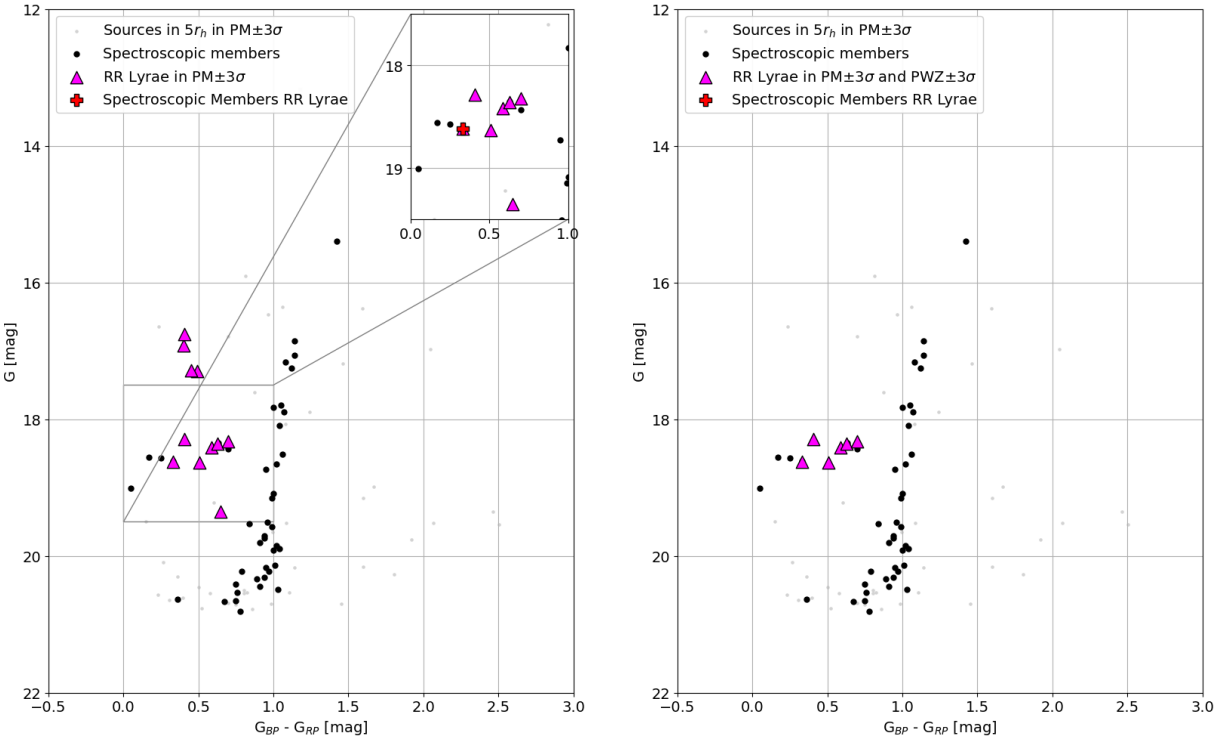

Figure 51: Color-magnitude diagram of Coma Berenices after proper motion selection only (**left panel**) and combined with PWZ selection (**right panel**). Spectroscopic members (black dots) delineate a well-defined stellar population sequence.

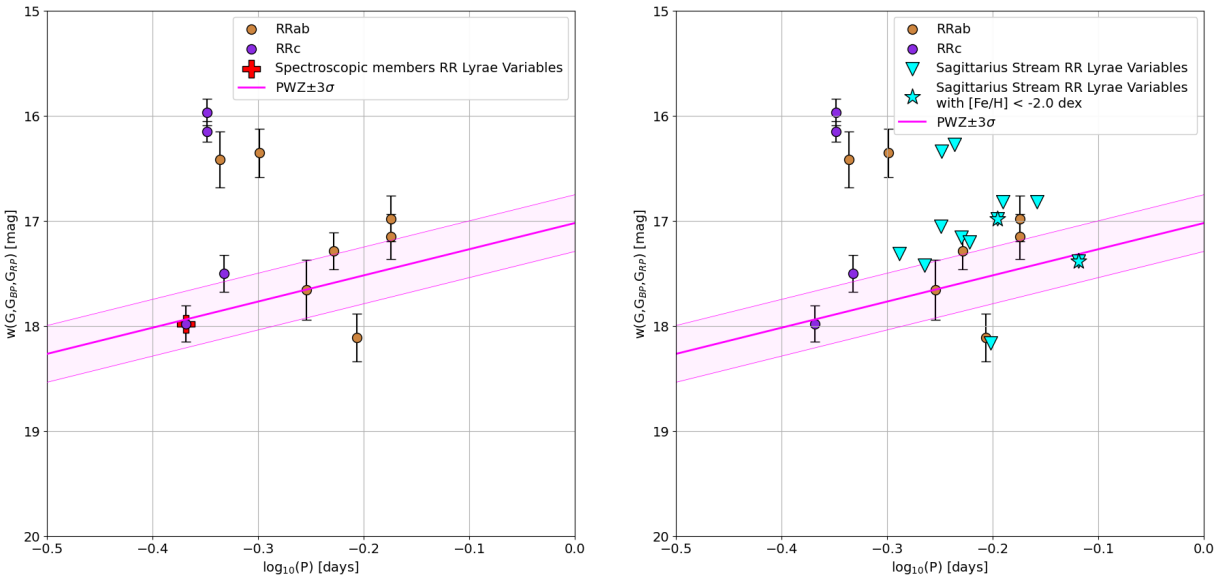

Figure 52: Pw diagram of RR Lyrae stars in Coma Berenices. The magenta solid line with $\pm 3\sigma$ bands shows the PWZ relation for RR Lyrae stars by Garofalo et al. (2022) shifted according to the distance modulus of Coma Berenices. RRab-type stars in brown; RRc-type stars in purple. Red cross (**left panel**): RR Lyrae spectroscopic member in Waller et al. (2023). Cyan triangles (**right panel**): RR Lyrae stars from Sagittarius Stream; RR Lyrae stars with [Fe/H] < -2.0 dex have been marked with a star ($\star$) symbol.

3.4.3 Reverse filtering via the PWZ relation

Repeating the analysis using only the PWZ relation, without applying any proper motion cut, yields 8 RR Lyrae stars (left panel of Fig. 53). The two additional variables (*Gaia* DR3 3958967640747443328 and *Gaia* DR3 3960293170734066560) are fainter in the G-band compared to the six retained in the proper motion selection (left panel of Fig. 53). As previously mentioned, the DR3 G magnitudes of this two stars may be inaccurate, and with the improved data from *Gaia* DR4, these RR Lyrae stars may align more consistently with the horizontal branch.
Upon inspecting their proper motion distribution, the group of 8 RR Lyrae stars clusters near the centroid defined by the spectroscopic members (Fig. 55). This suggests that a less restrictive 3σ threshold in the proper motion selection might have retained these additional stars.

The possibility that some RR Lyrae stars might instead be Anomalous Cepheids was investigated, but none of them was found to match the expected characteristics of ACEP-F or ACEP-1O types (right panel of Fig. 53).

In conclusion, 6 RR Lyrae stars can be considered likely candidates for membership in Boötes I, as they satisfy both the proper motion and PWZ relation selection criteria. Additionaly, two fainter RR Lyrae should be re-evaluated using the improved data from *Gaia* DR4. The CMD and spatial distribution of the RR Lyrae candidate members of Coma Benenices are shown in Fig. 54, while their properties are provided in Tab. 10.

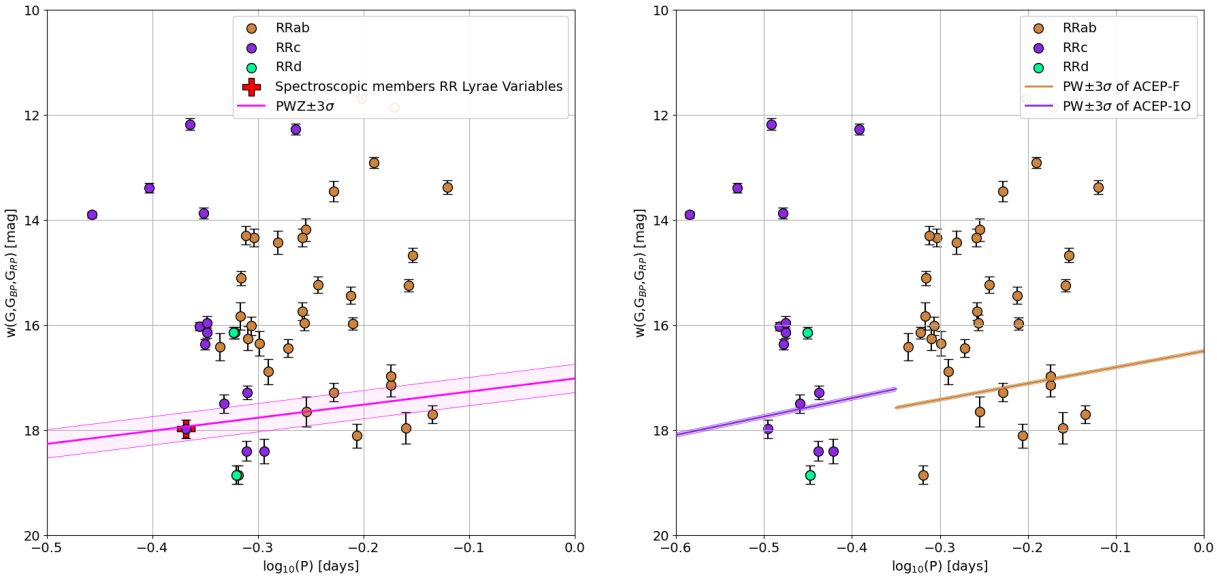

Figure 53: Pw diagram of RR Lyrae stars in Coma Berenice, without proper motion selection. The magenta solid line with $\pm 3\sigma$ bands shows the PWZ relation for RR Lyrae stars by Garofalo et al. (2022) (**left panel**), while in the **right panel** in brown is shown the PW relation for ACEP-F stars, and in purple is shown that for ACEP-1O stars (Ripepi et al. 2023). All the relations are shifted according to the distance modulus of Coma Berenices.

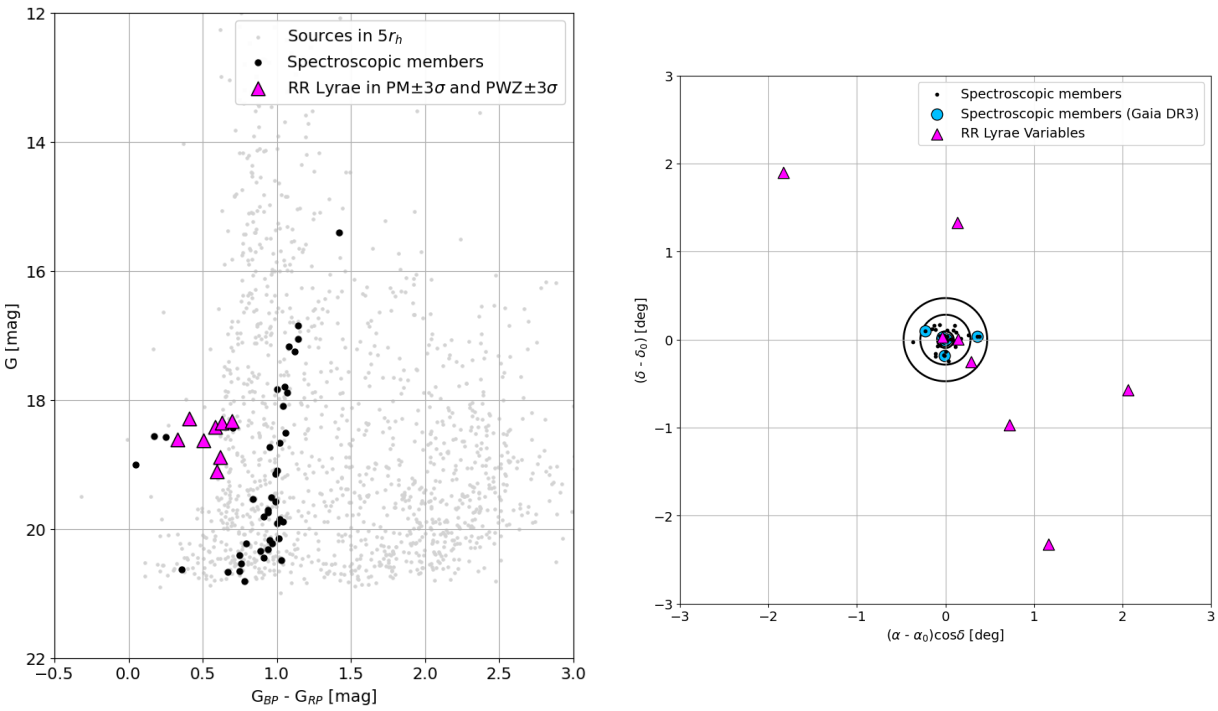

Figure 54: Left: Color-magnitude diagram of Coma Berenices after applying the PWZ selection to RR Lyrae stars. All RR Lyrae stars (magenta triangles) are located along the horizontal branch, with the exception of two which are fainter. **Right:** Spatial distribution of member stars identified through spectroscopy (black and light-blue dots) together with the RR Lyrae candidate members of Coma Berenices (magenta triangles). Black circles: 1, 3, 5 r_h around the centre.

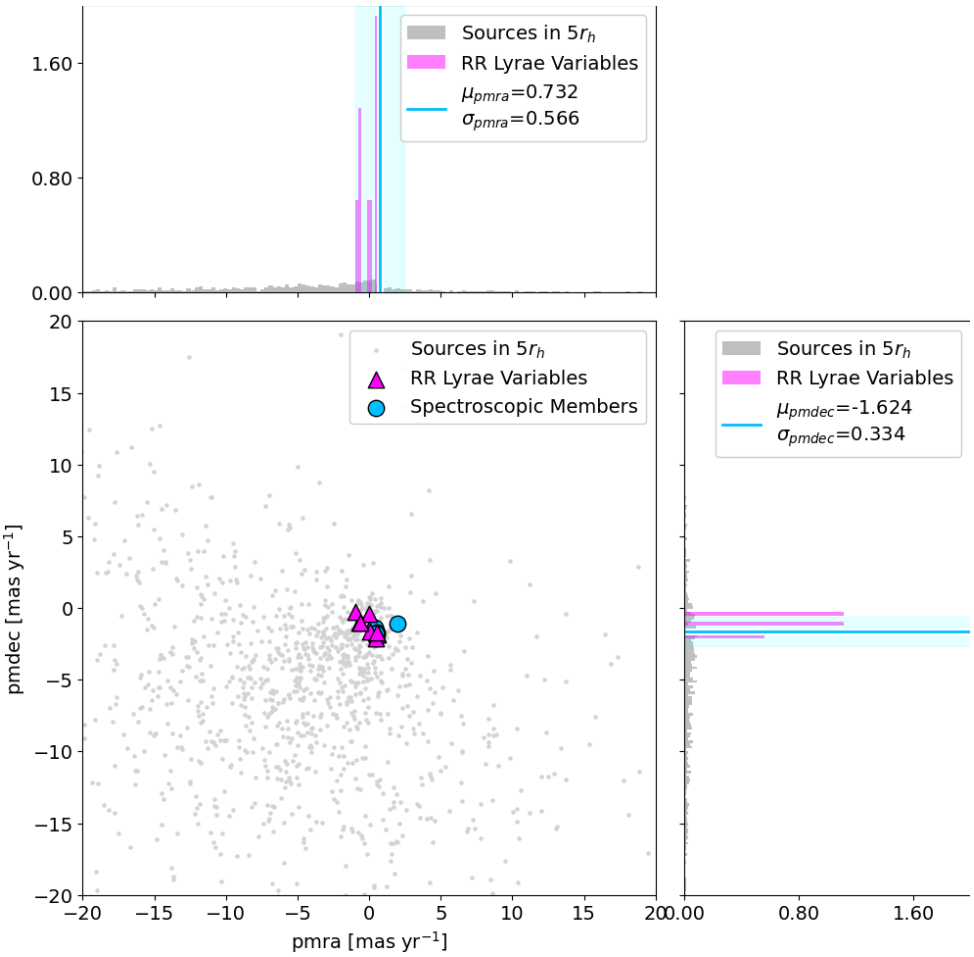

Figure 55: Proper motion distribution of RR Lyrae candidate members of Coma Berenices (magenta triangles).

Table 10: Properties of Coma Berenices RR Lyrae Variables identified through multi-method approach compared with literature.

Coma Berenices													
source_id	RA (deg)	Dec (deg)	pmra (mas/yr)	pmdec (mas/yr)	G (mag)	BP (mag)	RP (mag)	Class.	S.M.	Tau et al. (2024)	PM + PWZ	PWZ	ACEP
3959868763541740544	186.712	23.933	0.458	-2.089	18.619	18.704	18.372	RRc	Y	Y	Y	Y	-
3952621465790994304	187.908	21.583	0.031	-1.655	18.414	18.641	18.055	RRab	-	-	Y	Y	ACEP-F[1]
3958901704409542272	188.810	23.339	-0.695	-1.026	18.287	18.494	18.086	RRc	-	-	Y	Y	ACEP-1O[1]
3959816395004385152	187.038	23.658	0.612	-1.853	18.358	18.595	17.965	RRab	-	Y	Y	Y	ACEP-F[1]
3959870167995015936	186.890	23.915	0.535	-1.687	18.322	18.636	17.937	RRab	-	Y	Y	Y	ACEP-F[1]
4008518236060449408	184.916	25.805	-0.631	-1.000	18.631	18.846	18.339	RRab	-	-	Y	Y	-
3958967640747443328	187.472	22.942	0.003	-0.377	19.108	19.465	18.873	RRab	-	-	-	Y[2]	-
3960293170734066560	186.882	25.238	-0.945	-0.297	18.890	19.099	18.484	RRab	-	-	-	Y[2]	-

[1] = RR Lyrae stars which fall in the PW relation for Anomalous Cepheids (ACEP-F and ACEP-1O), however they are likely RR Lyrae stars.
[2] = RR Lyrae stars identified only through PWZ relation, their pmra are within 3σ of average proper motion, while pmdec within 4σ: these two RR Lyrae stars are candidates as members of Coma Berenices, even if they are fainter with respect to the others.

3.5 Sagittarius II

Sagittarius II is an ultra-faint stellar system discovered by Laevens et al. (2015) in the Pan-STARRS1 3Π survey as a compact stellar overdensity. Located at a heliocentric distance of 67 ± 5 kpc, Sgr II occupies a peculiar position in the size-luminosity plane - either representing the most compact dwarf galaxy or the most extended GC in its luminosity range ($M_V = -5.2 \pm 0.4$ mag, $r_h \sim 37$ pc). Its spatial location intriguingly coincides with the predicted path of the trailing arm of the Sagittarius stream, suggesting it may have originally been a satellite of the Sagittarius dwarf spheroidal galaxy (Sgr dSph), later accreted into the MW halo. The nature of Sgr II remains ambiguous and further spectroscopic investigation will be needed to determine whether it is a disrupting dwarf galaxy or an unusually extended star cluster.

Joo et al. (2019) studied the variable star population of Sgr II and identified six RR Lyrae stars using optical time-series photometry and G-band data from *Gaia* DR2. Of them, five variables - two RRab and three RRc stars - are located within three half-light radii of the galaxy, indicating strong membership probability. The RR Lyrae stars yield a heliocentric distance of $\sim 64 \pm 3$ kpc and an average metallicity of [Fe/H] $\sim -2.1 \pm 0.3$, indicating that Sgr II is an ancient, metal-poor system with an estimated age of ~ 12 Gyr. Its compact nature and metal-poor content underscore the importance of Sgr II as a transitional object between star clusters and UFD galaxies and as a key tracer of early accretion events in the Milky Way halo.

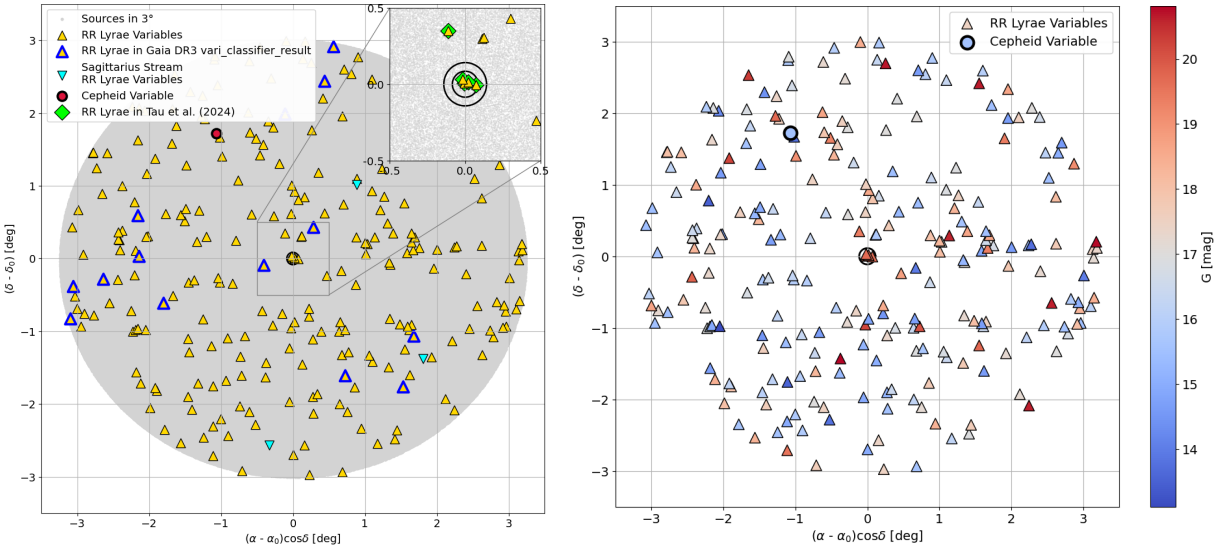

Figure 56: Left: Spatial distribution of sources (grey dots), RR Lyrae variables (yellow triangles), RR Lyrae candidates in the *Gaia* `gaiadr3.vari_classifier_result` catalogue (yellow triangles with blue edges) and a Cepheid variable (red dot) within 3° around the centre of Sagittarius II. Cyan triangles: Sagittarius Stream RR Lyrae stars. Green diamonds: RR Lyrae stars identified by Tau et al. (2024). Black circles: 1, 2, 3 r_h around the centre. **Right:** G-band color-map of RR Lyrae and Cepheid stars within 3° around the centre of Sagittarius II.

3.5.1 Spatial distribution and mapping of stellar population

Within 3° around the centre of Sagittarius II, there are 247 RR Lyrae variables, 14 of which are labeled as RR Lyrae by the *Gaia* `gaiadr3.vari_classifier_result` catalogue (Fig. 56). A Type II Cepheid (T2C) (*Gaia* DR3 6868588425062089984) is also present in the dataset. The Sagittarius Stream has 3 RR Lyrae stars in this area, leading to a reduction of the initial number of variables to 244.

According to Tau et al. (2024), five RR Lyrae stars are assigned to Sagittarius II. In Zaremba et al. (2025), a total of three sources were identified as Sagittarius II members through spectroscopic analysis, which have a correspondence in *Gaia* DR3 catalogue (Fig. 57).

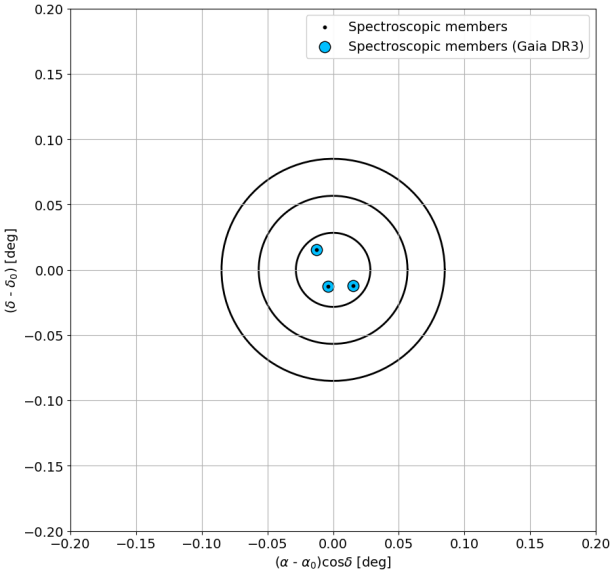

Figure 57: Spatial distribution of Sagittarius II member stars identified through spectroscopy. Black dots: members identified by Waller et al. (2023). Light-blue dots: members also catalogued in *Gaia* DR3. Black circles: 1, 2, 3 r_h around the centre.

3.5.2 Proper Motion and Period-Wesenheit-Metallicity Relation selections

The initial filtering to exclude variable stars with proper motion uncertainties greater than 0.5 mas yr^{-1} was not applied (Fig. 58), since the RR Lyrae stars in Sagittarius II are expected to be very faint ($G \sim 20$ mag).

The mean proper motion values are reported in Tab. 3. A selection was applied using a 3σ criterion from the mean values, which reduced the number of RR Lyrae stars to two (Fig. 59 and left panel in Fig. 60). None of the stars identified solely by the `gaiadr3.vari_classifier_result` catalogue, nor the Type II Cepheid, survived this filtering step.

The analysis of the color-magnitude diagram in left panel of Fig. 60 shows that one RRab Lyrae star (*Gaia* DR3 6864422993976659968) lies along the sparsely populated horizontal branch and survives the PWZ selection (right panel of Fig. 60, Fig. 61). This star is also reported by Tau et al. (2024).

Due to the small number of available stars (only three) from the Zaremba et al. (2025) catalogue - given the limited size of Sagittarius II - the uncertainties on the mean proper motions are very small, resulting in a very restrictive cut (Fig. 59). With a larger sample of spectroscopic members, the statistics would be more reliable and the CMD could be more populated.

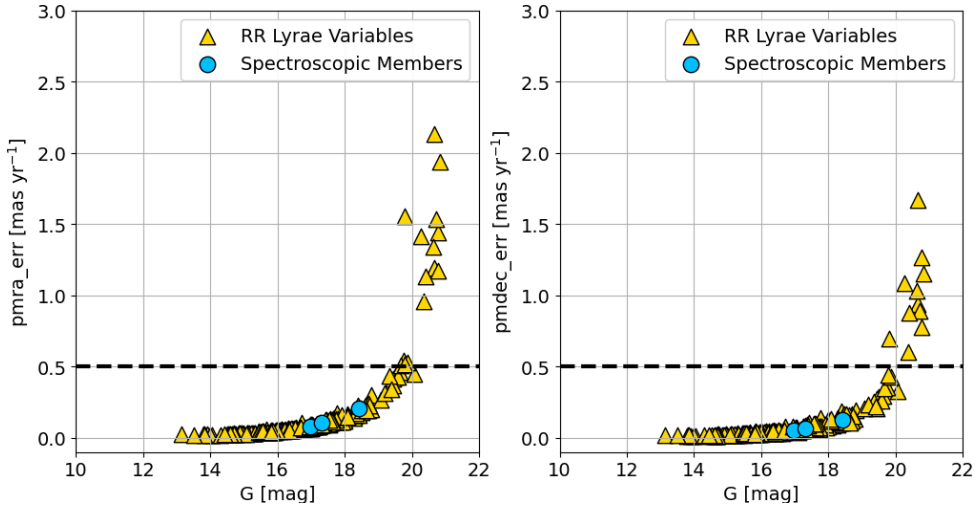

Figure 58: Proper motion errors of RR Lyrae stars (yellow triangles) and spectroscopic members (light-blue dots) within 3° around the centre of Sagittarius II as a function of G-band magnitude.

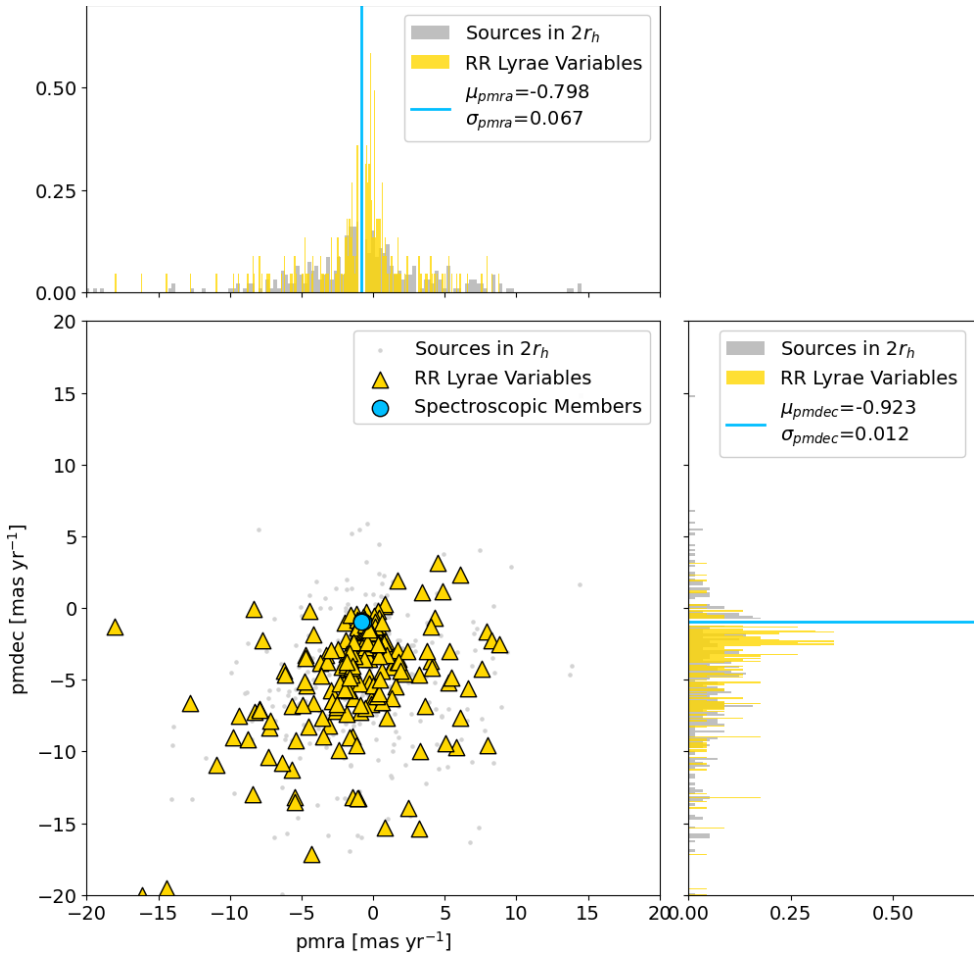

Figure 59: Proper motion distribution of sources within $2r_h$ (grey dots) and RR Lyrae stars in 3° (yellow triangles) around the centre of Sagittarius II. The cyan shaded bands representing the $\pm 3\sigma$ dispersion of the mean proper motions (cyan lines) - computed using the spectroscopic members (light-blue dots) - are not clearly visible due to the very small value of σ (see Tab. 3).

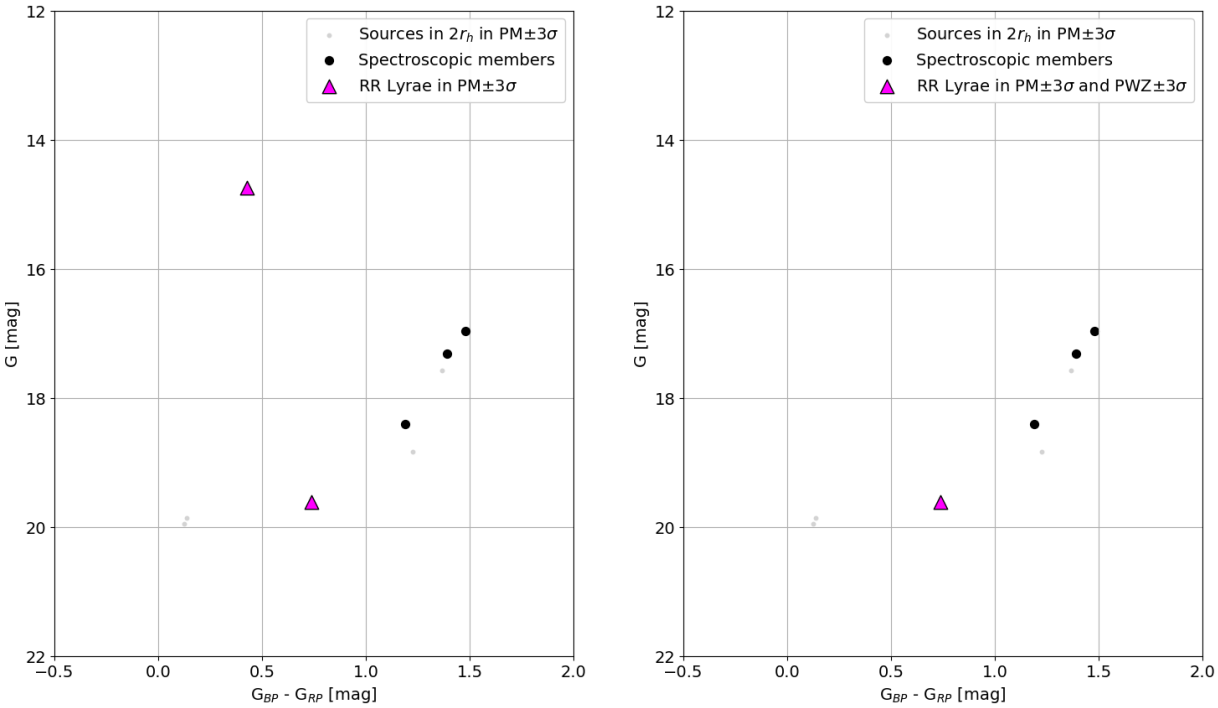

Figure 60: Color-magnitude diagram of Sagittarius II after proper motion selection only (**left panel**) and combined with PWZ selection (**right panel**). The spectroscopic members (black dots) show a poor red giant branch profile of the stellar population. An RR Lyrae star (magenta triangle) is located along the horizontal branch which is defined by very few sources within $2r_h$.

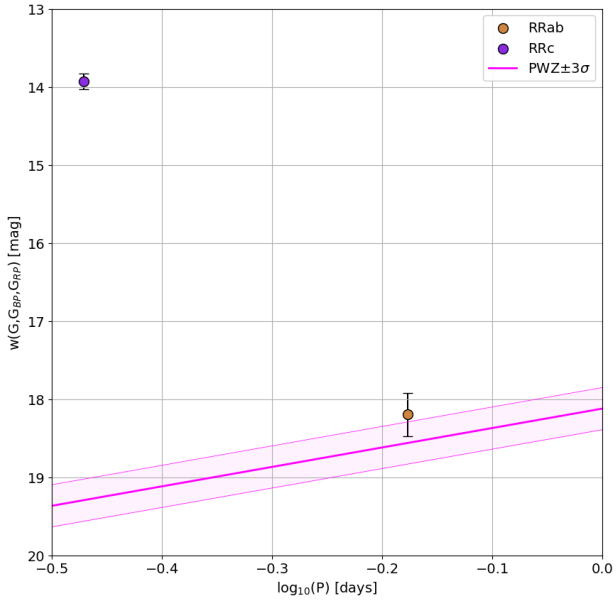

Figure 61: Pw diagram of RR Lyrae stars in Sagittarius II. The magenta solid line with ±3σ bands shows the PWZ relation for RR Lyrae stars by Garofalo et al. (2022) shifted according to the distance modulus of Sagittarius II. RRab-type star in brown, RRc-type star in purple.

3.5.3 Reverse filtering via the PWZ relation

When repeating the analysis using only the PWZ selection, seven RR Lyrae stars are retained. Four of them are identified by Tau et al. (2024), with the addition of *Gaia* DR3 6864423994704275200 (Fig. 62) which can be a candidate member if the parameters given in literature (such as distance modulus, metallicity, etc.) or whether the photometry in *Gaia* DR3 were not correct.

As mentioned earlier, the proper motion slicing is highly stringent due to the limited statistics on faint objects. This is further confirmed when examining the RR Lyrae stars selected only via the PWZ relation (Fig. 65): four out of the seven lie very close to the average proper motion values derived from the spectroscopic members (see Tab. 11).
Gaia DR3 6868610282153787648 displays divergent values in both pmra and pmdec, but its G-band magnitude is consistent with the potential position on the horizontal branch (left panel of Fig. 64), and so does *Gaia* DR3 6852036965426508544, even if it has pm_error > -0.5 mas yr^{-1}.
Gaia DR3 6863916741889551104 is instead less brighter than the others and has pm_error > -0.5 mas yr^{-1}, so it is likely that it is not a member of Sagittarius II. This again suggests that a better statistical sample on the astrometric and photometric parameters could allow a better identification of RR Lyrae variables associated with Sagittarius II.

The possibility that some of the RR Lyrae candidates might instead be Anomalous Cepheids was also explored (left panel of Fig. 63). However, although some stars fall within the Period-Wesenheit (PW) relation, they are more likely to be accurately classified as RR Lyrae variables.

A separate test was applied on the Type II Cepheid located within 3° of Sagittarius II to assess whether it might be an Anomalous Cepheid of Sagittarius II, but result was negative (right panel of Fig. 63).

In conclusion, 4 RR Lyrae stars can be considered likely candidates for membership in Sagittarius II, as they satisfy both a wider proper motion and the PWZ relation selection criteria. Additionaly, two fainter RR Lyrae stars and another one selected by Tau et al. (2024) should be re-evaluated using improved data from *Gaia* DR4.

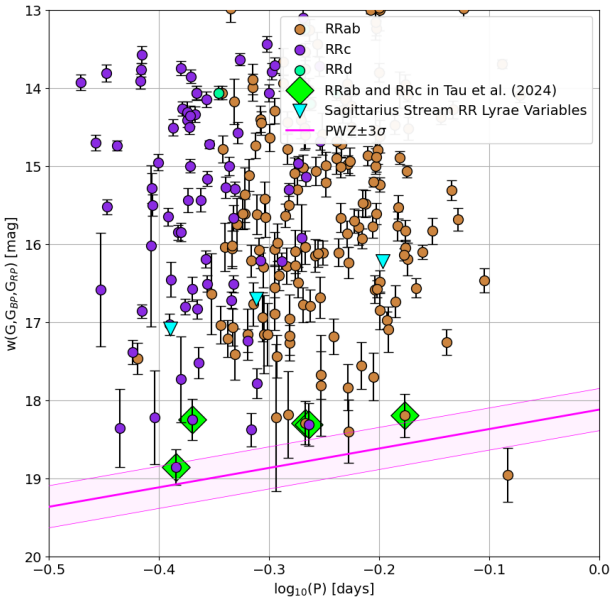

Figure 62: Pw diagram of RR Lyrae stars in Sagittarius II, without proper motion selection. The magenta solid line with $\pm 3\sigma$ bands shows the PWZ relation for RR Lyrae stars by Garofalo et al. (2022) shifted according to the distance modulus of Sagittarius II. Cyan triangles: RR Lyrae variables belonging to the Sagittarius Stream. Green diamonds: RR Lyrae stars classified as Sagittarius II members by Tau et al. (2024).

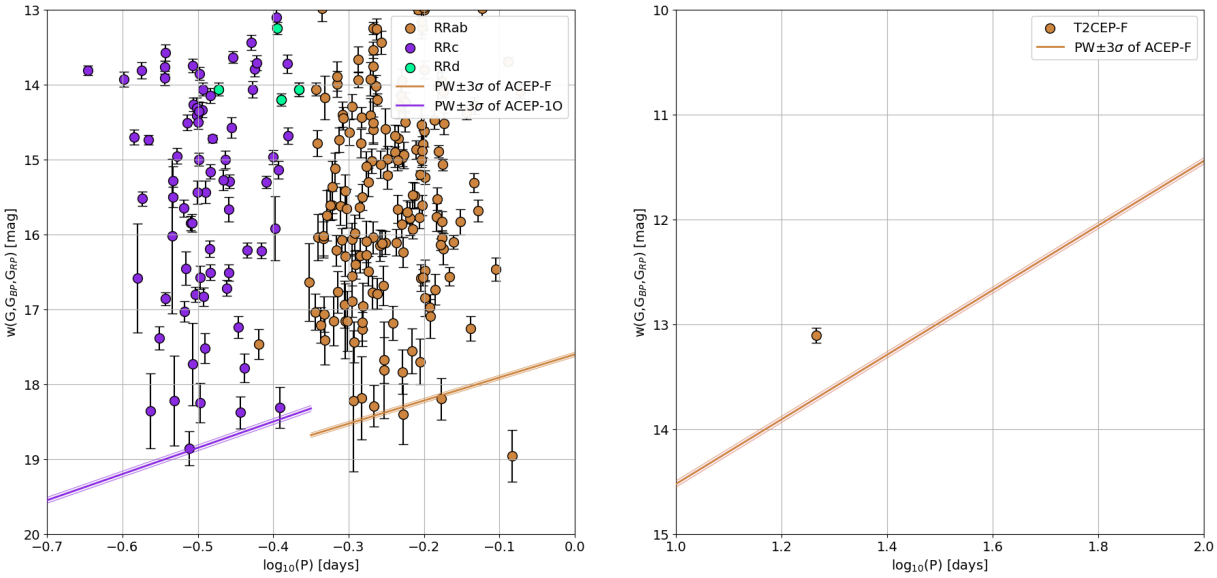

Figure 63: Pw diagram of RR Lyrae stars (**left panel**) and a Cepheid star (**right panel**) within 3° around the centre of Sagittarius II. The brown solid line with $\pm 3\sigma$ bands shows the PW relation for ACEP-F stars by Ripepi et al. (2023), and in purple it is shown that for ACEP-1O stars. All the relations are shifted according to the distance modulus of Sagittarius II.

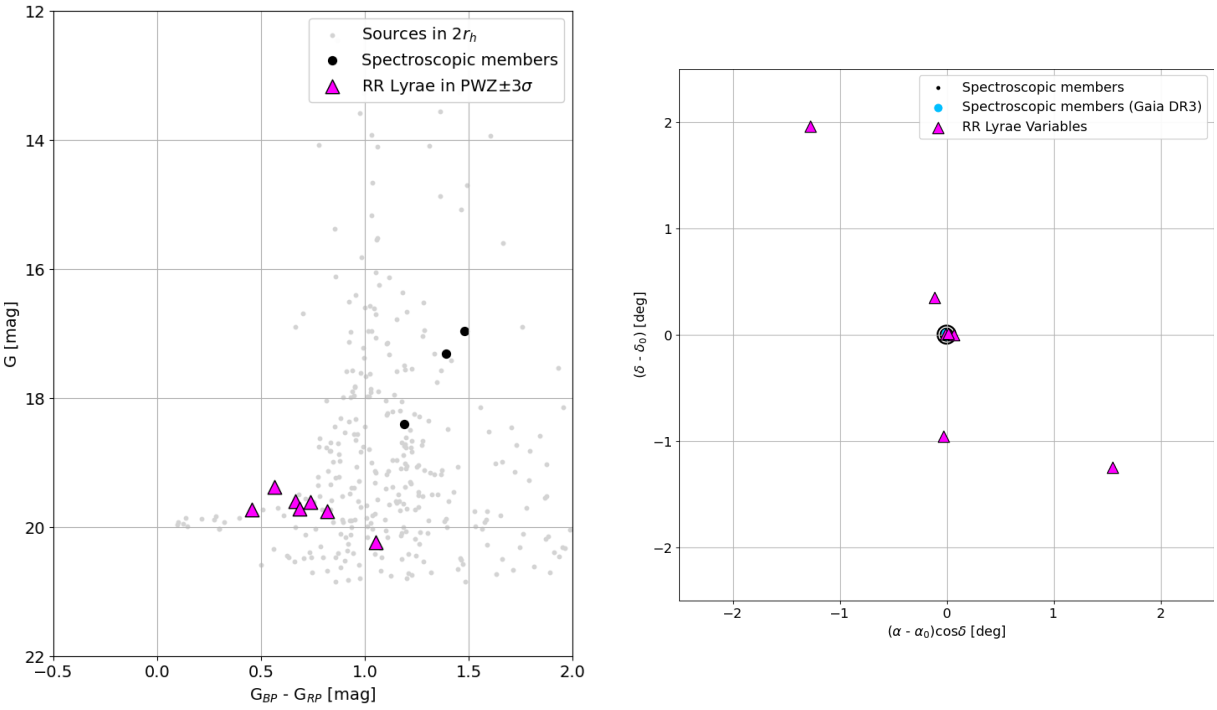

Figure 64: Left: Color-magnitude diagram of Sagittarius II after applying the PWZ selection to RR Lyrae stars. Almost all RR Lyrae stars (magenta triangles) are located along the potential horizontal branch of Sagittarius II. **Right:** Spatial distribution of member stars identified through spectroscopy (black and light-blue dots) together with the RR Lyrae candidate members of Sagittarius II (magenta triangles). Due to the very small half-light radius ($r_h = 1.7$ arcmin), it is not possible to clearly distinguish the 1, 2, and 3 r_h contours.

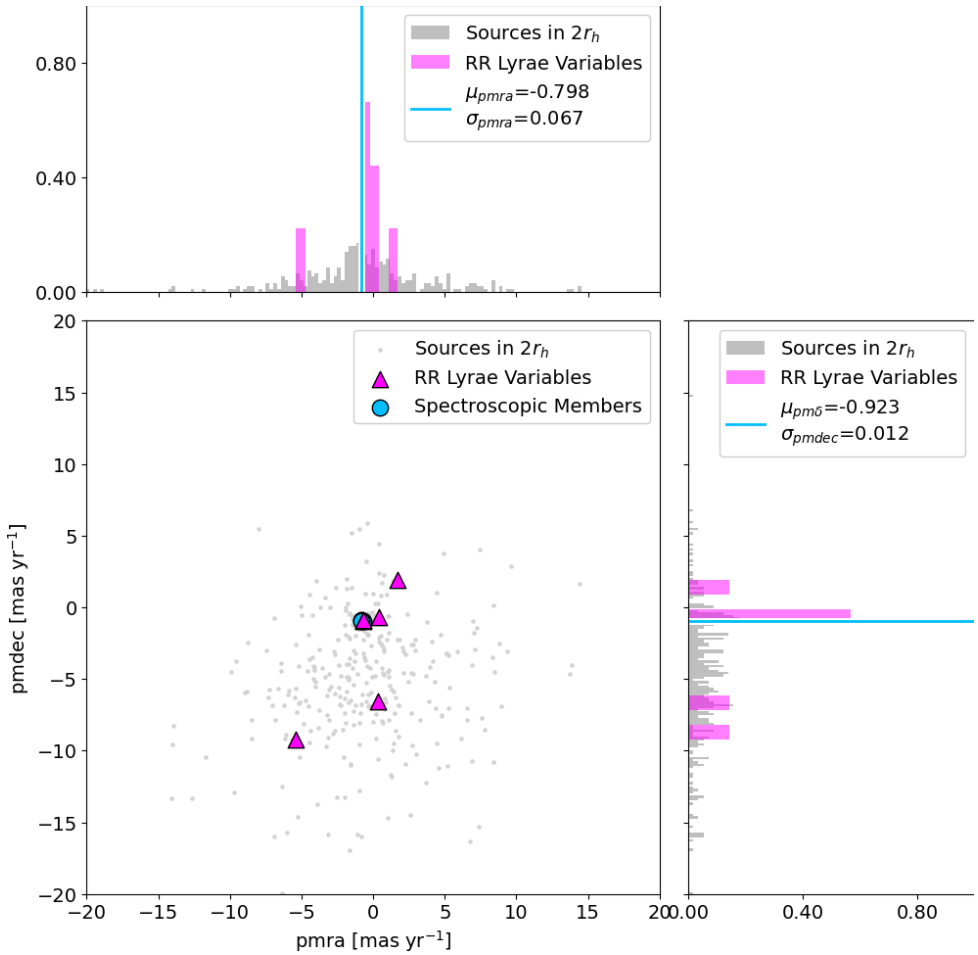

Figure 65: Proper motion distribution of RR Lyrae star candidate members (magenta triangles) of Sagittarius II after the PWZ relation selection only.

Table 11: Properties of Sagittarius II RR Lyrae Variables identified through multi-method approach compared with literature.

Sagittarius II												
source_id	RA (deg)	Dec (deg)	pmra (mas/yr)	pmdec (mas/yr)	G (mag)	BP (mag)	RP (mag)	Class.	Tau et al. (2024)	PM + PWZ	PWZ	ACEP
6864422993976659968	298.185	-22.051	-0.718	-0.909	19.615	19.922	19.184	RRab	Y	Y	Y	ACEP-F[1]
6852036965426508544	299.720	-23.311	0.311	-6.569	19.763	19.405	18.585	RRab	-	-	Y	ACEP-F[2]
6863916741889551104	298.138	-23.020	-5.380	-9.198	20.242	20.043	18.992	RRab	-	-	Y[3]	ACEP-F[3]
6864048408410304896	298.159	-22.058	0.372	-0.670	19.734	19.982	19.526	RRc	Y	-	Y	ACEP-1O[1]
6864422757758521984	298.236	-22.069	-0.676	-0.977	19.597	19.689	19.022	RRc	Y	-	Y	ACEP-1O[1]
6865195302117134336	298.055	-21.716	-0.683	-0.881	19.377	19.643	19.078	RRab	Y	-	Y	ACEP-F[1]
6868610282153787648	296.889	-20.104	1.717	1.895	19.715	19.598	18.913	RRab	-	-	Y	ACEP-F[2]
6864423994704275200	298.150	-22.033	0.064	-0.529	19.700	19.648	18.894	RRc	Y	-	-[4]	-
6853734473941355776	301.349	-21.861	-3.672	-3.795	20.767	21.384	19.847	RRab	-	-	-	ACEP-F[5]

[1] = RR Lyrae stars which fall into the PW relation for Anomalous Cepheids (ACEP-F and ACEP-1O), however they are likely RR Lyrae stars.
[2] = RR Lyrae stars which are consistent with the horizontal branch location, even if they have proper motions different with respect to the average or errors higher than 0.5 mas yr^{-1}.
[3] = RR Lyrae star too faint to belong to Sagittarius II, and it is also unlikely to be an Anomalous Cepheid.
[4] = RR Lyrae star classified by Tau et al. (2024), but not obtained through the multi-method approach since it does not fall in the PWZ relation, obtained only if the parameters in Vivas et al. (2020) or the photometry in *Gaia* DR3 are not correct.
[5] = RR Lyrae too faint to be an Anomalous Cepheid of Sagittarius II.

3.6 Ursa Major I

Ursa Major I is a MW UFD satellite, discovered by Willman et al. (2005) as an overdensity of red, resolved stars in the Sloan Digital Sky Survey (SDSS) data. Located at coordinates (α_{2000}, δ_{2000}) = (158.72°, 51.92°), in the constellation of Ursa Major, the system was initially noted for its striking similarity to the Sextans dwarf spheroidal galaxy in terms of its color-magnitude diagram, despite containing approximately an order of magnitude fewer stars. Deeper follow-up observations confirmed that Ursa Major I hosts an old and metal-poor stellar population and is situated at a heliocentric distance of roughly 100 kpc. Its total luminosity, estimated at $M_V \sim -6.75$ mag, is several times fainter than that of the faintest previously known Milky Way dwarf galaxies, while its half-light radius of ~ 250 pc places it well within the typical size range of classical dwarf spheroidals. Although uncertainties remain regarding its exact magnitude and structural parameters, UMa I is considered one of the lowest-luminosity and lowest surface brightness galaxies identified to date.

The first characterisation of the variable star population in Ursa Major I was done by Garofalo et al. (2013) using time-series photometry in optical bands. A total of seven RR Lyrae stars were identified- five RRab and two RRc types. The isodensity contour maps of RGB and HB stars, including the RR Lyrae variables, revealed an S-shaped morphology, suggestive of tidal disruption due to interactions with the MW gravitational field as already noticed in previous studies (Okamoto et al. 2008, and references therein).

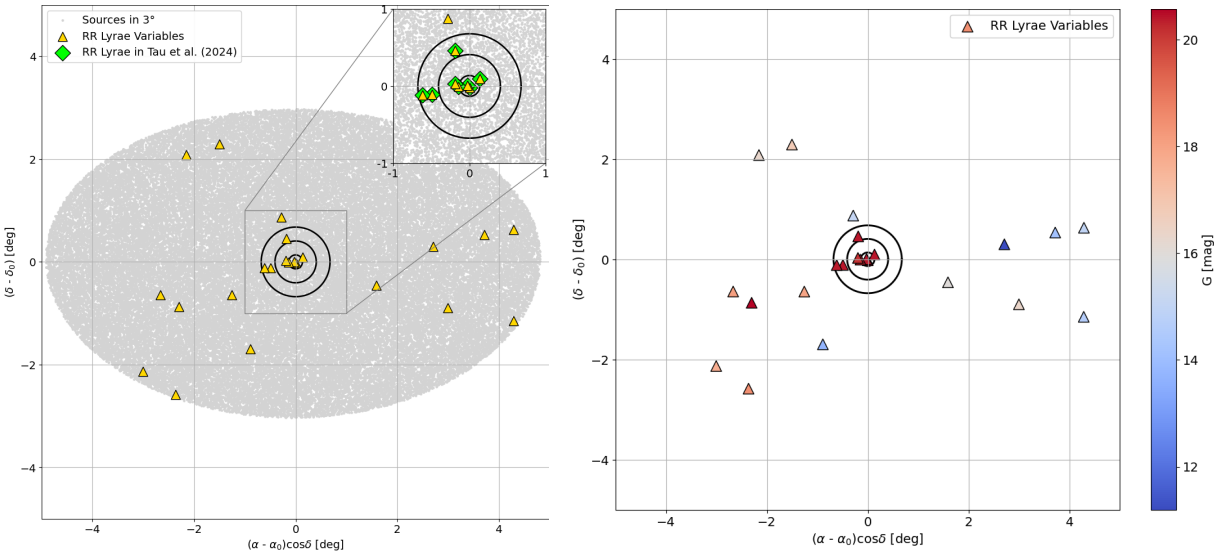

Figure 66: Left: Spatial distribution of sources (grey dots) and RR Lyrae variables (yellow triangles) in 3° around the centre of Ursa Major I. Green diamonds: 8 RR Lyrae variables listed by Tau et al. (2024). Black circles: 1, 3, 5 r_h around the centre. **Right:** G-band color-map of RR Lyrae stars within 3°around the centre of Ursa Major I.

3.6.1 Spatial distribution and mapping of stellar population

Within a 3° radius from the centre of Ursa Major I, 23 RR Lyrae variables are identified (left panel of Fig. 66). No Cepheid variables were found, and the Sagittarius Stream is not present in this portion of the sky. According to Tau et al. (2024), 8 RR Lyrae stars are associated with Ursa Major I, as shown in Fig. 67. Fifty-six member stars are identified through spectroscopic analysis by Waller et al. (2023): 28 of them are also present in the *Gaia* DR3 catalogue, including 5 RR Lyrae variables that are also reported by Tau et al. (2024) (left panel of Fig. 66).

As previously mentioned, a visual inspection of the colormap already provides an indication of which objects may belong to the same system, based on the expectation that RR Lyrae stars share similar intrinsic luminosities and are typically located along the horizontal branch. Stars with similar G-band magnitude appear clustered toward the centre of Ursa Major I (right panel of Fig. 66).

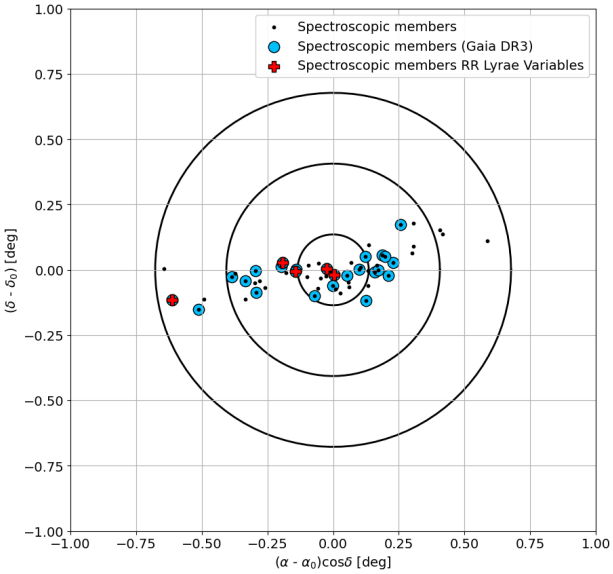

Figure 67: Spatial distribution of member stars identified through spectroscopy. Black dots: members identified by Waller et al. (2023). Light-blue dots: members also catalogued in *Gaia* DR3. Red crosses: RR Lyrae members. Black circles: 1, 3, 5 r_h around the centre.

3.6.2 Proper Motion and Period-Wesenheit-Metallicity Relation selections

In the case of Ursa Major I, all the RR Lyrae stars identified as spectroscopic members exhibit proper motion errors around 0.5 mas yr^{-1}, as they are intrinsically faint objects (Fig. 68). For this reason, the preliminary cut on proper motion errors - typically applied to account for increased uncertainties in *Gaia* measurements at magnitudes fainter than 20 mag - was not imposed.

The average proper motion values - computed using the spectroscopic members - are listed in Tab. 3 and the proper motion distributions are shown in Fig. 69. After the 3σ selection, the number of RR Lyrae stars decreased to 14.

The analysis of the color-magnitude diagram (left panel of Fig. 70), following the proper motion selection, shows that the RR Lyrae stars are predominantly located along the horizontal branch traced by the spectroscopic members. However, a peculiar scatter in the G-band magnitudes is observed, indicating the need for an additional selection criterion based on the Period-Wesenheit-Metallicity relation.

By considering sources within $5r_h$, it becomes clear that their spatial distribution deviates from that of the spectroscopic members. This discrepancy may be attributed to contamination from Milky Way field stars.

After applying the PWZ relation, 7 RR Lyrae stars remain: 5 of type RRab and 2 of type RRc (see Fig. 71, Tab. 12).
All spectroscopic members align well within the PWZ relation, with the exception of one RRab-type star (*Gaia* DR3 847520295882556928). As discussed for similar cases, this discrepancy may be attributed to uncertainties in the G_{BP} and G_{RP} photometry at such faint magnitudes. Furthemore, this is the most distant UFD in the sample, with the horizontal branch located at $G > 20$ mag, so these uncertainties are expected to be even more pronounced.

In the color-magnitude diagram (right panel of Fig. 70), after applying both the proper motion and Period-Wesenheit-Metallicity selections, the remaining RR Lyrae stars are well aligned along the horizontal branch.

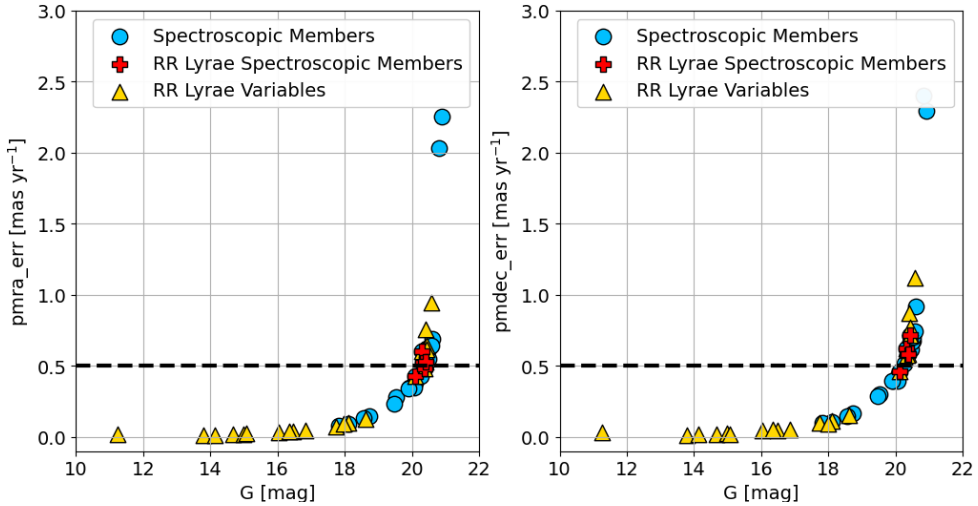

Figure 68: Proper motion errors of RR Lyrae stars (yellow triangles) and spectroscopic members (light-blue dots) within 3° around the centre of Ursa Major I as a function of G-band magnitude. Almost all the RR Lyrae spectroscopic members cross the 0.5 mas yr^{-1} (dashed) line, so the preliminary cut on proper motion errors was not applied.

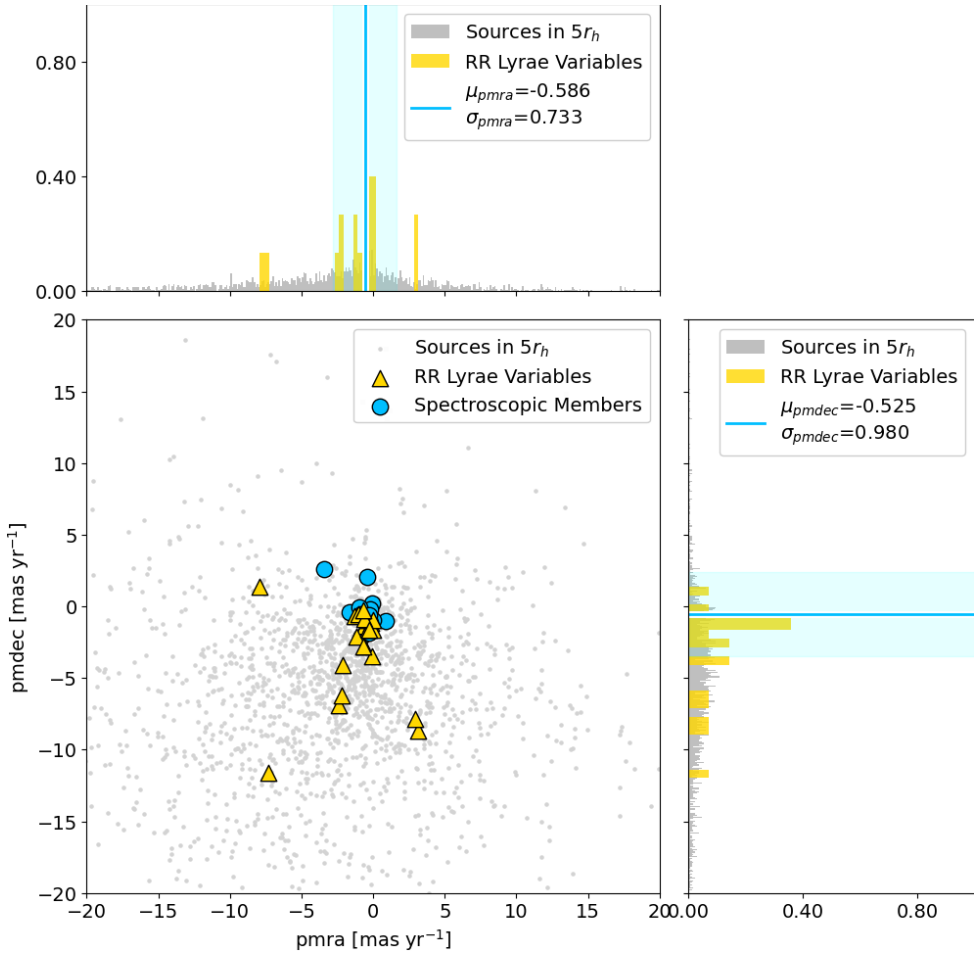

Figure 69: Proper motion distribution of sources within $5r_h$ (grey dots) and RR Lyrae stars in 3° (yellow triangles) around the centre of Ursa Major I. The cyan shaded bands represent $\pm 3\sigma$ of the mean proper motions (cyan lines) computed using the spectroscopic members (light-blue dots).

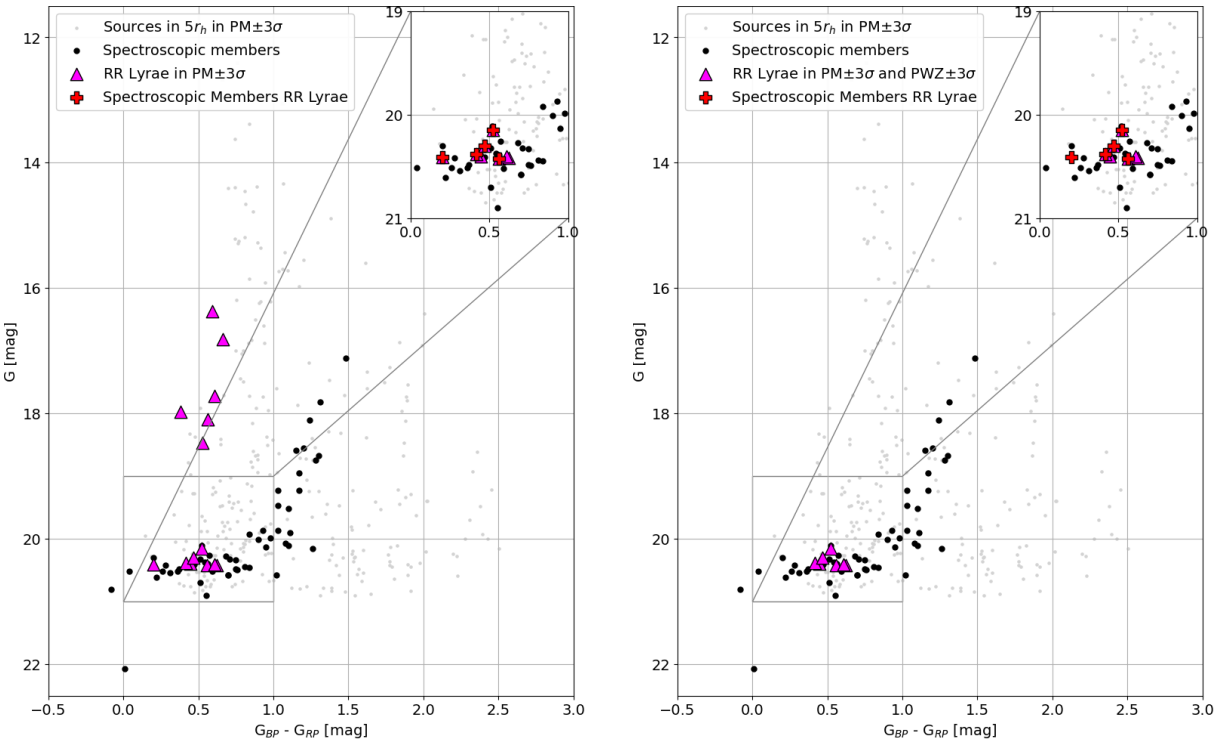

Figure 70: Color-magnitude diagram of Ursa Major I after proper motion selection only (**left panel**) and combined with the PWZ selection (**right panel**). Spectroscopic members (black dots) delineate a well-defined stellar population sequence. Many RR Lyrae stars (magenta triangles) are located along the horizontal branch, as well as the spectroscopic member RR Lyrae stars.

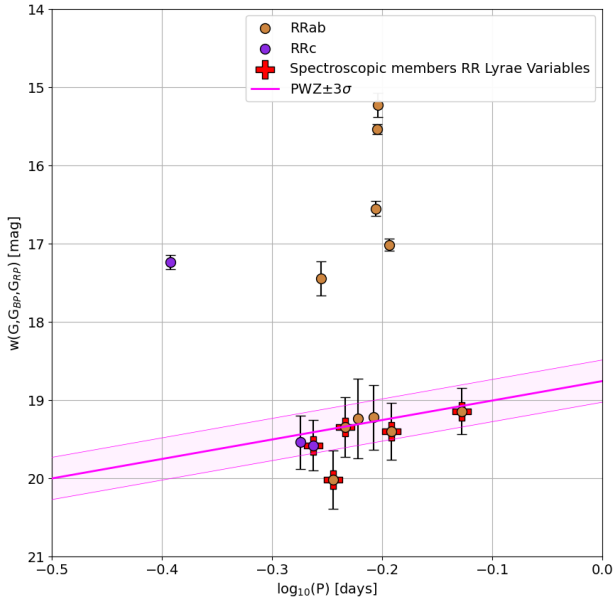

Figure 71: Pw diagram of RR Lyrae stars in Ursa Major I. The magenta solid line with ±3σ bands shows the PWZ relation for RR Lyrae stars by Garofalo et al. (2022) shifted according to the distance modulus of Ursa Major I. RRab-type stars in brown, RRc-type stars in purple. Red crosses: RR Lyrae spectroscopic members.

3.6.3 Reverse filtering via the PWZ relation

When repeating the analysis using only the Period-Wesenheit-Metallicity selection, without applying a proper motion cut, the same 7 RR Lyrae stars are recovered as in the previous combined selection (left panel of Fig. 72). This consistency confirms the robustness and reliability of the PWZ-based criterion.

Additionally, it was investigated the possibility that some of the RR Lyrae candidates might instead be Anomalous Cepheids. Although two stars (*Gaia* DR3 847779132087730816 and *Gaia* DR3 849022228766244992) fall into the PW relation for ACEP-F (right panel of Fig. 72), they are more likely classified in a correct way as RR Lyrae because they lie along the horizontal branch (left panel of Fig. 73).

In conclusion, 8 RR Lyrae stars can be considered likely candidates for membership in Ursa Major I, as they satisfy both the proper motion and PWZ relation selection criteria. Among these, the spectroscopic RR Lyrae star (*Gaia* DR3 847520295882556928) - not falling within the PWZ relation - was included, since its photometry should be re-evaluated using the improved data from *Gaia* DR4. The final proper motion distribution of the RR Lyrae candidates in shown in Fig. 74, and the complete catalogue of the analysed RR Lyrae variables is shown in Tab. 12.

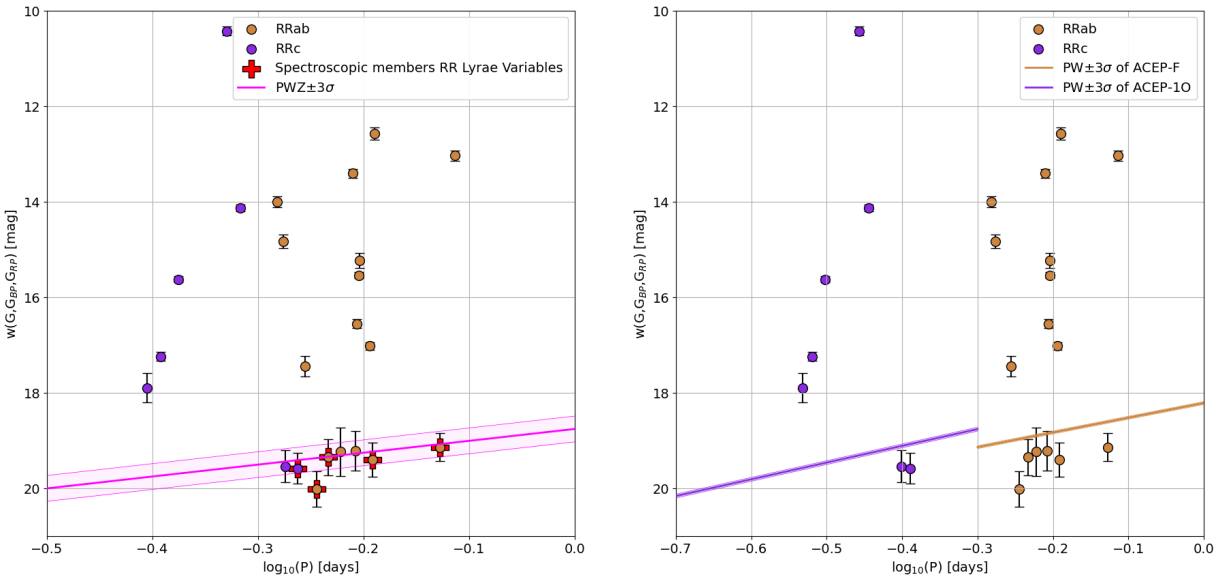

Figure 72: Left: Pw diagram of RR Lyrae stars in Ursa Major I. The magenta solid line with $\pm 3\sigma$ bands shows the PWZ relation for RR Lyrae stars by Garofalo et al. (2022) shifted according to the distance modulus of Ursa Major I. **Right:** Pw diagram of RR Lyrae stars within 3° around the centre of Ursa Major I. The purple solid line with $\pm 3\sigma$ bands shows the PW relation for ACEP-1O stars by Ripepi et al. (2023).

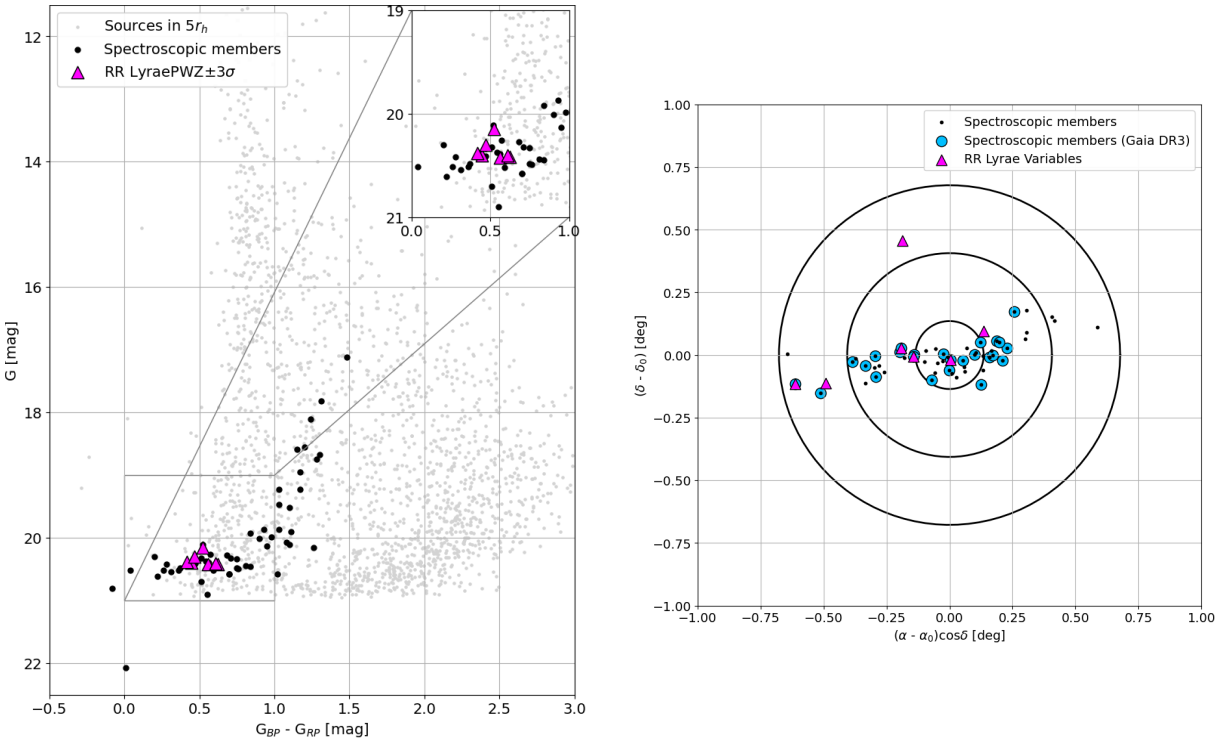

Figure 73: Left: Color-magnitude diagram after PWZ selection applied to RR Lyrae stars. All RR Lyrae stars (magenta triangles) are located along the horizontal branch. **Right:** Spatial distribution of member stars identified through spectroscopy (black and light-blue dots) together with the RR Lyrae candidate members of Ursa Major I (magenta triangles). Black circles: 1, 3, 5 r_h around the centre.

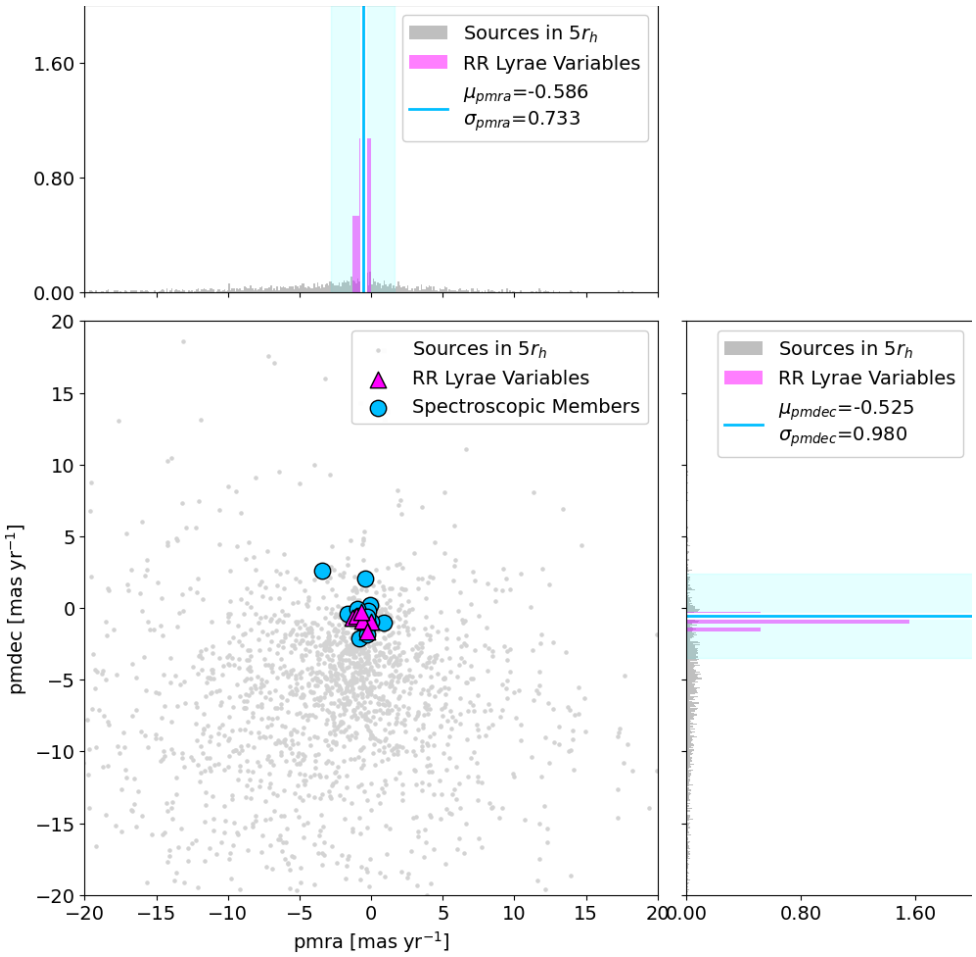

Figure 74: Proper motion distribution RR Lyrae candidate members of Ursa Major I (magenta triangles).

Table 12: Properties of Ursa Major I RR Lyrae Variables identified through multi-method approach compared with literature.

Ursa Major I													
source_id	RA (deg)	Dec (deg)	pmra (mas/yr)	pmdec (mas/yr)	G (mag)	BP (mag)	RP (mag)	Class.	S.M.	Tau et al. (2024)	PM + PWZ	PWZ	ACEP
847520295882556928	158.747	51.952	-0.137	-1.168	20.408	20.289	20.089	RRab	Y	Y	-[2]	-[2]	-
847706663103625984	158.628	51.941	-1.039	-0.537	20.304	20.510	20.041	RRab	Y	Y	Y	Y	-
847707728255299712	158.578	51.975	-0.644	-0.877	20.150	20.243	19.720	RRab	Y	Y	Y	Y	-
847519849205957760	158.773	51.928	-0.424	-0.964	20.423	20.638	20.079	RRab	Y	Y	Y	Y	-
847701990178947840	158.157	51.832	-0.007	-0.928	20.380	20.489	20.074	RRc	Y	Y	Y	Y	-
847700718868881792	158.280	51.835	-1.340	-0.651	20.399	20.481	20.035	RRc	-	Y	Y	Y	-
847779132087730816	158.584	52.405	-0.267	-1.621	20.418	20.606	19.984	RRab	-	Y	Y	Y	ACEP-F[1]
849022228766244992	158.907	52.043	-0.722	-0.243	20.404	20.735	20.129	RRab	-	Y	Y	Y	ACEP-F[1]

[1] = RR Lyrae stars which fall in the PW relation for Anomalous Cepheids (ACEP-F), however they are likely RR Lyrae stars.
[2] = RR Lyrae star classified by Waller et al. (2023) and by Tau et al. (2024), but not obtained through the multi-method approach since it does not fall in the PWZ relation., found only if the distance modulus in Vivas et al. (2020) or the photometry in *Gaia* DR3 are not correct.

4 Conclusions

Table 13: Summary of RR Lyrae candidate members for each UFD analysed in this work, using both the classical approach (first three columns) and the machine learning (ML) approach (only Boötes I). For consistency, the number of RR Lyrae stars identified as spectroscopic members (S.M.) and those reported by Tau et al. (2024) are also provided.

UFD	RR Lyrae candidate members	RR Lyrae*	ACEP*	ML	S.M.	Tau et al. (2024)
Boötes I	17	$3^{[a]} + 1^{[b]}$	1	$15^{[e]}$	6	27
Boötes III	38	$2^{[a]}$	4		3	32
Carina II	5	$4^{[c]}$	3		1	3
Coma Berenices	6	$2^{[c]}$	-		1	3
Sagittarius II	4	$2^{[d]}$	-		-	5
Ursa Major I	8	-	-		5	8

Notes. * = RR Lyrae and Anomalous Cepheid stars which require further investigation for their membership identification and classification. [a] = Sagittarius Stream RR Lyrae which fall within the PWZ relation. [b] = RR Lyrae stars in Tau et al. (2024), but not selected with the multi-method approach. [c] = PWZ-selected RR Lyrae stars fainter than the UFD's horizontal branch. [d] = PWZ-selected RR Lyrae stars with proper motions higher than the average. [e] = Only RR Lyrae stars from the *Gaia* DR3 `gaiadr3.vari_rrlyrae` catalogue with $G > 18$ mag were used for the ML test.

In this thesis, the RR Lyrae population around a sample of six ultra-faint dwarf (UFD) galaxies was explored using astrometric and photometric data from the *Gaia* Data Release 3.

A classical approach based on proper motion selection, color-magnitude diagram analysis, and the Period-Wesenheit-Metallicity (PWZ) relation of RR Lyrae stars was applied to the six UFDs in order to associate RR Lyrae stars most likely members to their respective host galaxies, cleaning the samples from contamination caused by variables belonging to other systems and substructures, among which, most noteworthy RR Lyrae in the Sagittarius Stream.

A machine learning-based approach, employing density-based clustering algorithms to identify statistically coherent stellar groups based on their astrometric and photometric properties, was also applied and tested on the Boötes I UFD.

The analysis showed that the combined application of the two approaches can provide a more robust framework for RR Lyrae membership identification in environments which are sparse and sensitive to contamination, such as the UFDs. This, in turn, allows for a more accurate characterisation of the stellar populations of these systems, which is crucial to unravel their contribution to the assembly of the Galactic halo.

The results obtained for the six target UFDs, summarised in Table 13, suggest that the RR Lyrae classifications reported in the literature by Tau et al. (2024) may be affected by contamination or may be incomplete.

The results of this work open several avenues for future research both for the classical and machine learning approaches. The latter include the introduction of non-variable sources to test the broader applicability of clustering methods, the exploration of alternative algorithms such as OPTICS or hierarchical models, and the integration of additional photometric features to improve the discriminatory power of classification techniques.

The application of statistical tests such as the Hopkins statistic (Hopkins et al. 1954; Banerjee et al. 2004) could provide a quantitative measure of the *clusterability* of different parameter spaces (e.g., astrometric vs. photometric), offering insights into which features are more effective for unsupervised classification.

On the other hand, the upcoming *Gaia* Data Release 4 (DR4) will provide more precise astrometric and photometric measurements, along with radial velocities for a larger sample of RR Lyrae stars. These improvements will enable more reliable membership assessments and facilitate detailed kinematic studies, even in the most challenging regions of the sky.

Expanding this analysis to larger samples of UFDs and extending it to other classes of variable stars will support the development of a more comprehensive understanding of the formation and evolution of the Milky Way halo. Integrating *Gaia* data with forthcoming spectroscopic surveys, such as those planned with WEAVE[16] and 4MOST[17], will supply the complementary chemical information necessary to fully reconstruct the Galaxy's accretion history. Furthermore, photometric metallicity estimates for RR Lyrae stars, either via relations between metal abundance, pulsation period, and Fourier decomposition parameters of the light curve (see, e.g., Muraveva et al. 2025b, and refernces therein) or directly from *Gaia* G-band light curves (Monti et al. 2025), could offer an alternative to spectroscopic observations, helping refine the chemical characterisation of UFD systems.

The methodologies developed in this thesis should be extended to the full sample of known UFD galaxies. Once optimized, they can help determine whether similar RR Lyrae associations exist across other systems, potentially revealing the structure, chemical evolution, and accretion history of the Milky Way halo.

The framework developed in this thesis represents a useful starting point for future work aimed at refining our knowledge of the Milky Way's UFD satellites through upcoming data and improved methodologies.

[16] `https://weave-project.atlassian.net/wiki/spaces/WEAVE/overview`
[17] `https://www.eso.org/sci/observing/PublicSurveys/4most-surveys-projects.html`

Appendix: Acronyms

UFD = Ultra-Faint Dwarf galaxies
MW = Milky Way
LMC = Large Magellanic Cloud
SMC = Small Magellanic Cloud
GC = Globular Cluster
RRLy = RR Lyrae variable
CC = Classical Cepheid variable
T2C = Type II Cepheid variable
ACEP = Anomalous Cepheid variable
Gaia (E)DR* = *Gaia* (Early) Data Release *
SDSS = Sloan Digital Sky Survey
PAndAS = Pan-Andromeda Archaeological Survey
PS1 = Pan-STARRS1
MagLiteS = Magellanic Satellites Survey
CCD = Charge-Coupled Device
BP = Blue Photometer Prisms
RP = Red Photometer Prisms
RVS = Radial-Velocity Spectrometer
FoV = Field-of-View
CMD = Color-Magnitude Diagram
RGB = Red Giant Branch
HB = Horizontal Branch
IS = Instability Strip
RA = Right Ascension
Dec = Declination
pmra = Proper Motion in Right Ascension direction
pmdec = Proper Motion in Declination direction
PWZ = Period-Wesenheit-Metallicity relation
PW = Period-Wesenheit relation
PL = Period-Luminosity relation
ML = Machine Learning
DBSCAN = Density-Based Spatial Clustering of Applications with Noise
HDBSCAN = Hierarchical Density-Based Spatial Clustering of Applications with Noise
OPTICS = Ordering Points To Identify the Clustering Structure
S.M. = Spectroscopic Members RR Lyrae stars
Class. = `best_classification` in `gaiadr3.vari_rrlyrae`
or `type_best_classification` in `gaiadr3.vari_cepheid`
or `best_class_name` in `gaiadr3.vari_classifier_result`

References

Ankerst, Mihael et al. (1999). 'OPTICS: ordering points to identify the clustering structure'. In: *SIGMOD Rec.* 28.2, pp. 49–60. ISSN: 0163-5808. DOI: 10.1145/304181.304187. URL: https://doi.org/10.1145/304181.304187.

Arias, Jose Marco et al. (2025). 'Andromeda XXXV: The Faintest Dwarf Satellite of the Andromeda Galaxy'. In: 982.1, L3, p. L3. DOI: 10.3847/2041-8213/adb433. arXiv: 2502.19516 [astro-ph.GA].

Banerjee, A. and R.N. Dave (2004). 'Validating clusters using the Hopkins statistic'. In: *IEEE International Conference on Fuzzy Systems: 2004; Budapest, Hungary* 1, 149–153 vol.1. DOI: 10.1109/FUZZY.2004.1375706.

Bell, Eric F. et al. (2022). 'Ultrafaint Dwarf Galaxy Candidates in the M81 Group: Signatures of Group Accretion'. In: 937.1, L3, p. L3. DOI: 10.3847/2041-8213/ac8e5e. arXiv: 2209.06009 [astro-ph.GA].

Belokurov, V. et al. (2006). 'A Faint New Milky Way Satellite in Bootes'. In: *The Astrophysical Journal* 647.2, p. L111. DOI: 10.1086/507324. URL: https://dx.doi.org/10.1086/507324.

Belokurov, V. et al. (2007). 'Cats and Dogs, Hair and a Hero: A Quintet of New Milky Way Companions'. In: 654.2, pp. 897–906. DOI: 10.1086/509718. arXiv: astro-ph/0608448 [astro-ph].

Bono, Giuseppe et al. (1997). 'Evolutionary Scenario for Metal-Poor Pulsating Stars.II.Anomalous Cepheids'. In: 113, p. 2209. DOI: 10.1086/118431.

Bovill, Mia S. and Massimo Ricotti (2009). 'Pre-Reionization Fossils, Ultra-Faint Dwarfs, and the Missing Galactic Satellite Problem'. In: 693.2, pp. 1859–1870. DOI: 10.1088/0004-637X/693/2/1859. arXiv: 0806.2340 [astro-ph].

Braga, V. F. et al. (2015). 'On the Distance of the Globular Cluster M4 (NGC 6121) Using RR Lyrae Stars. I. Optical and Near-infrared Period-Luminosity and Period-Wesenheit Relations'. In: 799.2, 165, p. 165. DOI: 10.1088/0004-637X/799/2/165. arXiv: 1411.6826 [astro-ph.GA].

Braga, V. F. et al. (2020). 'Separation between RR Lyrae and type II Cepheids and their importance for a distance determination: the case of omega Cen'. In: 644, A95, A95. DOI: 10.1051/0004-6361/202039145. arXiv: 2010.06368 [astro-ph.SR].

Brown, Thomas M. et al. (2014). 'The Quenching of the Ultra-faint Dwarf Galaxies in the Reionization Era'. In: 796.2, 91, p. 91. DOI: 10.1088/0004-637X/796/2/91. arXiv: 1410.0681 [astro-ph.GA].

Bullock, James S., Andrey V. Kravtsov and David H. Weinberg (2000). 'Reionization and the Abundance of Galactic Satellites'. In: 539.2, pp. 517–521. DOI: 10.1086/309279. arXiv: astro-ph/0002214 [astro-ph].

Campello, Ricardo J. G. B., Davoud Moulavi and Joerg Sander (2013). 'Density-Based Clustering Based on Hierarchical Density Estimates'. In: *Advances in Knowledge Discovery and Data Mining*. Ed. by Jian Pei et al. Berlin, Heidelberg: Springer Berlin Heidelberg, pp. 160–172. ISBN: 978-3-642-37456-2.

Caputo, F. et al. (2004). 'Bright metal-poor variables: Why "Anomalous" Cepheids?' In: 424, pp. 927–934. DOI: 10.1051/0004-6361:20040307. arXiv: astro-ph/0405395 [astro-ph].

Carlin, Jeffrey L. and D. J. Sand (2018). 'Boötes III is a Disrupting Dwarf Galaxy Associated with the Styx Stellar Stream'. In: *The Astrophysical Journal* 865.1, p. 7. DOI: https://doi.org/10.3847/1538-4357/aad8c1.

Clement, Christine M. et al. (2001). 'Variable Stars in Galactic Globular Clusters'. In: 122.5, pp. 2587–2599. DOI: 10.1086/323719. arXiv: astro-ph/0108024 [astro-ph].

Clementini, G. et al. (2016). 'Gaia Data Release 1. The Cepheid and RR Lyrae star pipeline and its application to the south ecliptic pole region'. In: 595, A133, A133. DOI: 10.1051/0004-6361/201629583. arXiv: 1609.04269 [astro-ph.SR].

Clementini, G. et al. (2019). 'Gaia Data Release 2. Specific characterisation and validation of all-sky Cepheids and RR Lyrae stars'. In: 622, A60, A60. DOI: 10.1051/0004-6361/201833374. arXiv: 1805.02079 [astro-ph.SR].

Clementini, G. et al. (2023). 'Gaia Data Release 3. Specific processing and validation of all-sky RR Lyrae and Cepheid stars: The RR Lyrae sample'. In: 674, A18, A18. DOI: 10.1051/0004-6361/202243964. arXiv: 2206.06278 [astro-ph.SR].

Clementini, Gisella et al. (2003). 'Distance to the Large Magellanic Cloud: The RR Lyrae Stars'. In: 125.3, pp. 1309–1329. DOI: 10.1086/367773.

Dall'Ora, Massimo et al. (2006). 'Variable Stars in the Newly Discovered Milky Way Satellite in Bootes*'. In: *The Astrophysical Journal* 653.2, p. L109. DOI: 10.1086/510665. URL: https://dx.doi.org/10.1086/510665.

Ester, Martin et al. (1996). 'A Density-Based Algorithm for Discovering Clusters in Large Spatial Databases with Noise'. In: *Second International Conference on Knowledge Discovery and Data Mining (KDD'96). Proceedings of a conference held August 2-4*. Ed. by D. W. Pfitzner and J. K. Salmon, pp. 226–331.

Frebel, Anna and John E. Norris (2015). 'Near-Field Cosmology with Extremely Metal-Poor Stars'. In: 53, pp. 631–688. DOI: 10.1146/annurev-astro-082214-122423. arXiv: 1501.06921 [astro-ph.SR].

Fritz, T. K. et al. (2018). 'Gaia DR2 proper motions of dwarf galaxies within 420 kpc. Orbits, Milky Way mass, tidal influences, planar alignments, and group infall'. In: 619, A103, A103. DOI: 10.1051/0004-6361/201833343. arXiv: 1805.00908 [astro-ph.GA].

Fuchs, Matthias and Wolfram Höpken (2022). 'Clustering'. In: *Applied Data Science in Tourism: Interdisciplinary Approaches, Methodologies, and Applications*. Ed. by Roman Egger. Cham: Springer International Publishing, pp. 129–149. ISBN: 978-3-030-88389-8. DOI: 10.1007/978-3-030-88389-8_8. URL: https://doi.org/10.1007/978-3-030-88389-8_8.

Gaia Collaboration et al. (2016). 'The Gaia mission'. In: 595, A1, A1. DOI: 10.1051/0004-6361/201629272. arXiv: 1609.04153 [astro-ph.IM].

Gaia Collaboration et al. (2021). 'Gaia Early Data Release 3. Summary of the contents and survey properties'. In: 649, A1, A1. DOI: 10.1051/0004-6361/202039657. arXiv: 2012.01533 [astro-ph.GA].

Garofalo, A. et al. (2022). 'New LZ and PW(Z) relations of RR Lyrae stars calibrated with Gaia EDR3 parallaxes'. In: *Monthly Notices of the Royal Astronomical Society* 513.1, pp. 788–806. DOI: https://doi.org/10.1093/mnras/stac735.

Garofalo, Alessia et al. (2013). 'VARIABLE STARS IN THE ULTRA-FAINT DWARF SPHEROIDAL GALAXY URSA MAJOR I*'. In: *The Astrophysical Journal* 767.1, p. 62. DOI: 10.1088/0004-637X/767/1/62. URL: https://dx.doi.org/10.1088/0004-637X/767/1/62.

Greene, Derek, Padraig Cunningham and Rudolf Mayer (2008). 'Unsupervised Learning and Clustering'. In: Springer, pp. 51–90. ISBN: 9783540751700. DOI: 10.1007/978-3-540-75171-7-3.

Grillmair, C. J. (2009). 'FOUR NEW STELLAR DEBRIS STREAMS IN THE GALACTIC HALO'. In: *The Astrophysical Journal* 693.2, p. 1118. DOI: 10.1088/0004-637X/693/2/1118. URL: https://dx.doi.org/10.1088/0004-637X/693/2/1118.

Groenewegen, M. A. T. (2024). 'Primary Period-Luminosity-Relation Calibrators in the Milky Way: Cepheids and RR Lyrae Physical basis, Calibration, and Applications'. In: *IAU Symposium*. Ed. by Richard de Grijs, Patricia A. Whitelock and Márcio Catelan. Vol. 376. IAU Symposium, pp. 128–149. DOI: 10.1017/S1743921323002995. arXiv: 2307.03033 [astro-ph.GA].

Hopkins, Brian and J. G. Skellam (1954). 'A New Method for determining the Type of Distribution of Plant Individuals'. In: *Annals of Botany* 18.2, pp. 213–227. ISSN: 0305-7364. DOI: 10.1093/oxfordjournals.aob.a083391. eprint: https://academic.oup.com/aob/article-pdf/18/2/213/778952/18-2-213.pdf. URL: https://doi.org/10.1093/oxfordjournals.aob.a083391.

Jensen, Jaclyn et al. (2024). 'Small-scale stellar haloes: detecting low surface brightness features in the outskirts of Milky Way dwarf satellites'. In: 527.2, pp. 4209–4233. DOI: 10.1093/mnras/stad3322. arXiv: 2308.07394 [astro-ph.GA].

Ji, A. P. et al. (2020). 'Detailed Abundances in the Ultra-faint Magellanic Satellites Carina II and III'. In: *The Astrophysical Journal* 889.1, p. 27. DOI: https://doi.org/10.3847/1538-4357/ab6213.

Joo, Seok-Joo et al. (2019). 'RR Lyrae Stars in the Field of Sagittarius II'. In: *The Astrophysical Journal* 875.2, p. 120. DOI: 10.3847/1538-4357/ab11ca. URL: https://dx.doi.org/10.3847/1538-4357/ab11ca.

Kundu, Richa, Dante Minniti and Harinder P. Singh (2019). 'Search for extra-tidal RR Lyrae stars in Milky Way globular clusters from Gaia DR2'. In: 483.2, pp. 1737–1743. DOI: 10.1093/mnras/sty3239. arXiv: 1811.11130 [astro-ph.GA].

Laevens, Benjamin P. M. et al. (2015). 'Sagittarius II, Draco II and Laevens 3: Three New Milky Way Satellites Discovered in the Pan-STARRS 1 3π Survey'. In: 813.1, 44, p. 44. DOI: 10.1088/0004-637X/813/1/44. arXiv: 1507.07564 [astro-ph.GA].

Leavitt, Henrietta S. and Edward C. Pickering (1912). 'Periods of 25 Variable Stars in the Small Magellanic Cloud.' In: *Harvard College Observatory Circular* 173, pp. 1–3.

Longmore, A. J., J. A. Fernley and R. F. Jameson (1986). 'RR Lyrae stars in globular clusters : better distances from infrared measurements ?' In: 220, pp. 279–287. DOI: 10.1093/mnras/220.2.279.

Madore, B. F. (1982). 'The period-luminosity relation. IV. Intrinsic relations and reddenings for the Large Magellanic Cloud Cepheids.' In: 253, pp. 575–579. DOI: 10.1086/159659.

Marconi, M. et al. (2015). 'On a New Theoretical Framework for RR Lyrae Stars. I. The Metallicity Dependence'. In: 808.1, 50, p. 50. DOI: 10.1088/0004-637X/808/1/50. arXiv: 1505.02531 [astro-ph.SR].

Martin, Nicolas F. et al. (2009). 'PAndAS' CUBS: Discovery of Two New Dwarf Galaxies in the Surroundings of the Andromeda and Triangulum Galaxies'. In: 705.1, pp. 758–765. DOI: 10.1088/0004-637X/705/1/758. arXiv: 0909.0399 [astro-ph.CO].

Martínez-Vázquez, C. E. et al. (2016). 'Probing the early chemical evolution of the Sculptor dSph with purely old stellar tracers'. In: 461.1, pp. L41–L45. DOI: 10.1093/mnrasl/slw093. arXiv: 1605.02768 [astro-ph.GA].

McConnachie, Alan W. (2012). 'The Observed Properties of Dwarf Galaxies in and around the Local Group'. In: 144.1, 4, p. 4. DOI: 10.1088/0004-6256/144/1/4. arXiv: 1204.1562 [astro-ph.CO].

Monti, Lorenzo et al. (2025). 'Unified Deep Learning Approach for Estimating the Metallicities of RR Lyrae Stars Using light curves from Gaia Data Release 3'. In: *arXiv e-prints*, arXiv:2505.20947, arXiv:2505.20947. DOI: 10.48550/arXiv.2505.20947. arXiv: 2505.20947 [astro-ph.SR].

Muñoz, Ricardo R. et al. (2018). 'A MegaCam Survey of Outer Halo Satellites. III. Photometric and Structural Parameters'. In: 860.1, 66, p. 66. DOI: 10.3847/1538-4357/aac16b. arXiv: 1806.06891 [astro-ph.GA].

Muraveva, T. et al. (2018). 'RR Lyrae stars as standard candles in the Gaia Data Release 2 Era'. In: 481, pp. 1195–1211. DOI: 10.1093/mnras/sty2241. arXiv: 1805.08742 [astro-ph.SR].

Muraveva, Tatiana et al. (2020). 'A fresh look at the RR Lyrae population in the Draco dwarf spheroidal galaxy with Gaia'. In: 499.3, pp. 4040–4053. DOI: 10.1093/mnras/staa2984. arXiv: 2009.12191 [astro-ph.GA].

Muraveva, Tatiana et al. (2025a). 'Exploring the Sagittarius stream with RR Lyrae Stars from Gaia Data Release 3'. In: *Astronomy & Astrophysics*. DOI: https://arxiv.org/abs/2505.20165.

Muraveva, Tatiana et al. (2025b). 'Metallicity of RR Lyrae stars from the Gaia Data Release 3 catalogue computed with Machine Learning algorithms'. In: 536.3, pp. 2749–2769. DOI: 10.1093/mnras/stae2679. arXiv: 2407.05815 [astro-ph.SR].

Musella, Ilaria et al. (2009). 'Pulsating Variable Stars in the Coma Berenices Dwarf Spheroidal Galaxy'. In: 695.1, pp. L83–L87. DOI: 10.1088/0004-637X/695/1/L83. arXiv: 0902.4230 [astro-ph.GA].

Narloch, W. et al. (2025). 'Period–luminosity relations for Galactic Type II Cepheids in the Sloan bands'. In: 697, A30, A30. DOI: 10.1051/0004-6361/202553733. arXiv: 2503.10532 [astro-ph.SR].

Neeley, Jillian R. et al. (2017). 'On a New Theoretical Framework for RR Lyrae Stars. II. Mid-infrared Period-Luminosity-Metallicity Relations'. In: 841.2, 84, p. 84. DOI: 10.3847/1538-4357/aa713d. arXiv: 1705.01970 [astro-ph.SR].

Neeley, Jillian R. et al. (2019). 'Standard Galactic field RR Lyrae II: a Gaia DR2 calibration of the period-Wesenheit-metallicity relation'. In: 490.3, pp. 4254–4270. DOI: 10.1093/mnras/stz2814. arXiv: 1910.01773 [astro-ph.SR].

Nemec, James M. et al. (2024). 'Double-mode RR Lyrae stars observed by K2: analysis of high-precision Kepler photometry'. In: 529.1, pp. 296–319. DOI: 10.1093/mnras/stae424. arXiv: 2402.06997 [astro-ph.SR].

Okamoto, S. et al. (2008). 'A Suprime-Cam study of the stellar population of the Ursa Major I dwarf spheroidal galaxy'. In: 487.1, pp. 103–108. DOI: 10.1051/0004-6361:20078232. arXiv: 0804.2976 [astro-ph].

Ortiz, I. et al. (2008). *IVOA Astronomical Data Query Language Version 2.00*. https://www.ivoa.net/documents/ADQL/. IVOA Recommendation.

Petersen, J. O. (1973). 'Masses of double mode cepheid variables determined by analysis of period ratios.' In: 27, p. 89.

Ricotti, Massimo and Nickolay Y. Gnedin (2005). 'Formation Histories of Dwarf Galaxies in the Local Group'. In: 629.1, pp. 259–267. DOI: 10.1086/431415. arXiv: astro-ph/0408563 [astro-ph].

Riess, Adam G. et al. (2022). 'A Comprehensive Measurement of the Local Value of the Hubble Constant with 1 km s^{-1} Mpc^{-1} Uncertainty from the Hubble Space Telescope and the SH0ES Team'. In: 934.1, L7, p. L7. DOI: 10.3847/2041-8213/ac5c5b. arXiv: 2112.04510 [astro-ph.CO].

Rimoldini, Lorenzo et al. (2023). 'Gaia Data Release 3. All-sky classification of 12.4 million variable sources into 25 classes'. In: 674, A14, A14. DOI: 10.1051/0004-6361/202245591. arXiv: 2211.17238 [astro-ph.GA].

Ripepi, V. et al. (2014). 'The VMC Survey - VIII. First results for anomalous Cepheids'. In: 437.3, pp. 2307–2319. DOI: 10.1093/mnras/stt2047. arXiv: 1310.5967 [astro-ph.SR].

Ripepi, V. et al. (2019). 'Reclassification of Cepheids in the Gaia Data Release 2. Period-luminosity and period-Wesenheit relations in the Gaia passbands'. In: 625, A14, A14. DOI: 10.1051/0004-6361/201834506. arXiv: 1810.10486 [astro-ph.SR].

Ripepi, V. et al. (2023). 'Gaia Data Release 3 -Specific processing and validation of all sky RR Lyrae and Cepheid stars: The Cepheid sample'. In: *Astronomy & Astrophysics* 674.A17. DOI: https://doi.org/10.1051/0004-6361/202243990.

Ripepi, V. et al. (2024). 'First spectroscopic investigation of anomalous Cepheid variables'. In: 682, A1, A1. DOI: 10.1051/0004-6361/202347991. arXiv: 2310.20503 [astro-ph.GA].

Salaris, Maurizio and Santi Cassisi (2005). *Evolution of Stars and Stellar Populations*. John Wiley & Sons Ltd.

Sicignano, T. et al. (2024). 'The VMC survey. L. Type II Cepheids in the Magellanic Clouds: Period-luminosity relations in the near-infrared bands'. In: 685, A41, A41. DOI: 10.1051/0004-6361/202348650. arXiv: 2401.12770 [astro-ph.SR].

Sicignano, Teresa et al. (2025). 'The VMC Survey – LIV. Anomalous Cepheids in the Magellanic Clouds Period-Luminosity relations in the near-infrared bands'. In: *arXiv e-prints*, arXiv:2506.08208, arXiv:2506.08208. DOI: 10.48550/arXiv.2506.08208. arXiv: 2506.08208 [astro-ph.SR].

Siegel, Michael H. (2006). 'RR Lyrae Stars in the Boötes Dwarf Spheroidal Galaxy'. In: *The Astrophysical Journal* 649.2, p. L83. DOI: 10.1086/508491. URL: https://dx.doi.org/10.1086/508491.

Simon, Joshua D. (2019). 'The Faintest Dwarf Galaxies'. In: *Annual Review of Astronomy and Astrophysics* 57, pp. 375–415. DOI: https://doi.org/10.1146/annurev-astro-091918-104453.

Simon, Joshua D. and Marla Geha (2007). 'The Kinematics of the Ultra-faint Milky Way Satellites: Solving the Missing Satellite Problem'. In: 670.1, pp. 313–331. DOI: 10.1086/521816. arXiv: 0706.0516 [astro-ph].

Soszyński, I. et al. (2008). 'The Optical Gravitational Lensing Experiment. The OGLE-III Catalog of Variable Stars. II.Type II Cepheids and Anomalous Cepheids in the Large Magellanic Cloud'. In: 58, p. 293. DOI: 10.48550/arXiv.0811.3636. arXiv: 0811.3636 [astro-ph].

Soszyński, I. et al. (2015). 'The OGLE Collection of Variable Stars. Anomalous Cepheids in the Magellanic Clouds'. In: 65.3, pp. 233–250. DOI: 10.48550/arXiv.1508.00907. arXiv: 1508.00907 [astro-ph.SR].

Tau, Elisa A., A. Katherina Vivas and Clara E. Martínez-Vázquez (2024). 'Extended Stellar Populations in Ultrafaint Dwarf Galaxies'. In: *The Astronomical Journal* 167.2, p. 57. DOI: https://doi.org/10.3847/1538-3881/ad1509.

Torrealba, G et al. (2018). 'Discovery of two neighbouring satellites in the Carina constellation with MagLiteS'. In: *Monthly Notices of the Royal Astronomical Society* 475.4, pp. 5085–5097. ISSN: 0035-8711. DOI: 10.1093/mnras/sty170. eprint: https://academic.oup.com/mnras/article-pdf/475/4/5085/24056790/sty170.pdf. URL: https://doi.org/10.1093/mnras/sty170.

Vivas, A. Katherina, Clara Martínez-Vázquez and Alistair Walker (2020). 'Gaia RR Lyrae Stars in Nearby Ultra-Faint Dwarf Satellite Galaxies'. In: *The Astrophysical Journal* 247.1, p. 35. DOI: https://doi.org/10.3847/1538-4365/ab67c0.

Waller, Fletcher et al. (2023). 'The Cosmic Hunt for members in the outskirts of ultra-faint dwarf galaxies: Ursa Major I, Coma Berenices, and Boötes I'. In: *Monthly Notices of the Royal Astronomical Society* 519.1, pp. 1349–1365. DOI: https://doi.org/10.1093/mnras/stac3563.

Willman, Beth et al. (2005). 'A New Milky Way Dwarf Galaxy in Ursa Major'. In: 626.2, pp. L85–L88. DOI: 10.1086/431760. arXiv: astro-ph/0503552 [astro-ph].

Wolf, Joe et al. (2010). 'Accurate masses for dispersion-supported galaxies'. In: 406.2, pp. 1220–1237. DOI: 10.1111/j.1365-2966.2010.16753.x. arXiv: 0908.2995 [astro-ph.CO].

Zaremba, Daria et al. (2025). 'GHOST commissioning science results - IV: Chemodynamical analyses of Milky Way satellites Sagittarius II and Aquarius II'. In: DOI: https://doi.org/10.48550/arXiv.2503.05927.

Zinn, R. and M. J. West (1984). 'The globular cluster system of the Galaxy. III. Measurements of radial velocity and metallicity for 60 clusters and a compilation of metallicities for 121 clusters.' In: 55, pp. 45–66. DOI: 10.1086/190947.